# A STUDY OF BIREFRINGENT SCINTILLATION TOWARDS THE MILLISECOND PULSAR J0437-4715

A THESIS SUBMITTED TO AUCKLAND UNIVERSITY OF TECHNOLOGY
IN PARTIAL FULFILMENT OF THE REQUIREMENTS FOR THE DEGREE OF
MASTER OF SCIENCE (RESEARCH)

Supervisor
Dr. Willem van Straten

2021

By
Afiq Abdul Hamid
School of Engineering, Computer and Mathematical Sciences

# Abstract

Pulsars are highly magnetized rapidly rotating neutron stars that emit streams of energetic charged particles along their magnetic axes. They are observable in the radio spectrum when their emission sweeps across the line of sight of radio telescopes. Pulsars are useful tools for testing theories of relativistic gravity and as probes of the magnetoionic plasma contained within the galactic interstellar medium (ISM). The latter motivation is given focus in this thesis with the aim of contributing towards current understanding of the nature of diffuse astrophysical plasmas on small scales.

This thesis presents a study of birefringent multipath propagation effects along the line of sight to the nearby millisecond pulsar PSR J0437-4715 with the objective of probing for small scale variations of interstellar magnetic fields within the Local Bubble of the ISM. We analyze more than 60 hours of calibrated data observed from MeerKAT radio observatory to observe the phenomena of differential scintillation of orthogonal senses of circularly polarized emission from the pulsar, owing to birefringence in the thin scattering screens of magnetoionic plasma that causes scintillation. The derived limits on the magnitude of differential scintillation are used to constrain the amplitude of spatial variations of magnetic fields on scales of less than 1 x $10^{11}$ cm within the scattering region.

Our approach is mainly twofold; we first create dynamic spectra of left and right circular polarization intensities using the psrflux program of the PSRCHIVE pulsar data analysis software. We then search for manifestations of significant differential phase effects caused by birefringent scintillation by computing the difference between the dynamic spectra, the secondary spectrum, and the secondary cross spectrum. Through our analysis, we have found a signal where phase varies slowly at low Doppler shifts and low spatial frequencies from the imaginary part of the secondary cross spectrum, however, the stochastic nature of the signal along the parabola lead us to believe that the signal phase is dominated by the jitter noise intrinsic to the pulsar. We conclude by calculating $3\sigma$ upper limit constraints on the amplitude of magnetic field fluctuations from the variance of differential phase measured from the normalization of phase from the secondary cross spectrum. Our constraints provide insights on the sensitivities of the MeerKAT L-band receiver towards detecting magnetic field fluctuations on small turbulent scales from birefringent scintillation.

# Contents

# List of Tables

# List of Figures

# Attestation of Authorship

I hereby declare that this submission is my own work and that, to the best of my knowledge and belief, it contains no material previously published or written by another person nor material which to a substantial extent has been accepted for the qualification of any other degree or diploma of a university or other institution of higher learning.

Signature of student

# Acknowledgements

I would like to express much gratitude and thanks to my parents Drs. Fatimah Kari and Abdul Hamid Jaafar for entertaining my wildest dreams of becoming an astrophysiscist. Thank you for lighting my way to the stars. To my younger brothers Luqman Abdullah and Aizat Iman who are now physically far away from me but never far from my thoughts.

Many thanks to the expert and accommodating staff of Auckland University of Technology Institute of Radio Astronomy and Space Research that supported and me throughout this endeavour. Much appreciation goes out towards institute director Professor Sergei Gulyaev, deputy director Tim Natusch, Dr. Stuart Weston and Patricia Sallis. A very special thanks to my supervisor Dr. Willem van Straten who has had much patience with me throughout my study and with the conditions brought about by the year 2020.

Appreciation is also noted towards my fellow postgraduate peers Natalia Primak, Axl Rogers, and Asif Rayhan for their kind fellowship and many a charming evening conversations. I wish them the best of luck in all their future endeavours.

I would also like to express my gratitude towards Drs. Daniel Reardon and Aditya Parthasarathy of Swinburne University of Technology Centre for Astrophysics and Supercomputing and the Max Planck Institute for Radio Astronomy. The former for providing the Scintools platform that was instrumental for this work and the latter for the provisioning of calibrated data of the J0437-4715 observations given focus on in this work, on top of all the support in between.

And finally, to Fatin Najihah Elier who was a steadfast companion throughout my two years at AUT.

# Chapter 1

# Introduction

## 1.1 Introduction

In 1968, a remarkable discovery was made on the fields of the Mullard Radio Astronomy Observatory in Cambridge of the United Kingdom. Using the Interplanetary Scintillation Array, two radio astronomers; Jocelyn Bell Burnell and Anthony Hewish happened across a repeating radio signal with a period of 1.33 seconds (Hewish et al., 1968). There had been many proposals for possible origins of the mysterious signal such as pulsating white dwarves and extraterrestrials beacons. Baade and Zwicky (1934) had proposed that compact stars composed primarily of neutrons having the average density of nuclear matter existed. The discovery of the of the Crab Pulsar and its accompanying supernova remnant (SNR) a year later led to the acceptance of the association of the pulsating radio source and the rapidly rotating neutron star model (Staelin and Reifenstein, 1968), as well as the association of supernovae (the explosive deaths of massive stars) with the existence of *pulsars*, a type of stellar remnant that are left behind in the wake of supernovae.

## 1.2 The Nature of Pulsars

Pulsars are highly magnetized rotating neutron stars (NS) that emit beams of radio emission along a magnetic axis. When the rotational axis is misaligned with their magnetic axis the beams sweep out a cone like pattern, making the pulsar observable with radio telescopes as a periodic lighthouse effect when the beams sweep across the telescope line of sight (LoS; Gold 1968). Pulsars are remarkable astrophysical laboratories because they are host to many extreme conditions irreplicable on Earth.

Pulsars are extremely dense objects comprised of degenerate matter held together by quantum mechanical forces. If the mass of the progenitor star is between 8 – 25 $M_{\odot}$ the star will explode as a supernova upon depletion of main sequence nuclear fuel to leave behind an ultra compact core (Stahler and Palla, 2004). The compact core will exist in this state so long as its mass is greater than 1.4 $M_{\odot}$ (Chandrasekhar, 1931) and no greater than the range of 2 - 2.5 $M_{\odot}$. If this core were to somehow be injected with additional mass beyond this range it will experience further collapse into a stellar mass black hole (Oppenheimer and Volkoff, 1939). The range of 2 - 2.5 $M_{\odot}$ is dependent on the NS equation of state (EoS) that relates the NS pressure to its density.

The pulsar phenomenon is a product of the asymmetrical supernova explosions that occur upon stellar collapse. The magnetic fields in massive stars produce a core in solid-body rotation with fields of $10^{12}$ G. Upon stellar collapse angular momentum is conserved and the core receives a kick that imparts upon it a space velocity of 100 - 1000 km s$^{-1}$. The kick also influences the birth spin of the ejected core with a greater kick producing a higher spin frequency (Spruit and Phinney, 1998; Burrows, 1998). Kick velocity contributes to NS spin period as a factor:

$$P_{\mathrm{NS}} = 0.07 \frac{200\,\mathrm{km\ s^{-1}}}{v} \frac{0.5}{\sin(\alpha)} \frac{3}{f_{\Omega}}\ \mathrm{s} \tag{1.1}$$

where $v$ is velocity, $f_{\Omega}$ is angular rotation frequency, and $\alpha$ is the angle between spin and magnetic axes. Radio pulsars are born with $P_{\mathrm{NS}}$ in the range of 0.05–0.5 seconds. Since the magnetic field of the progenitor is conserved, a co-rotating plasma filled magnetosphere is produced. A light cylinder encloses the NS beyond which would imply plasma co-rotating at superluminal velocities which is a physical impossibility. This creates gaps in the magnetosphere, where coherent radio emission is produced from electron-positron pair plasma (Sturrock, 1971). Fig. 1.1 is a model of a pulsar.

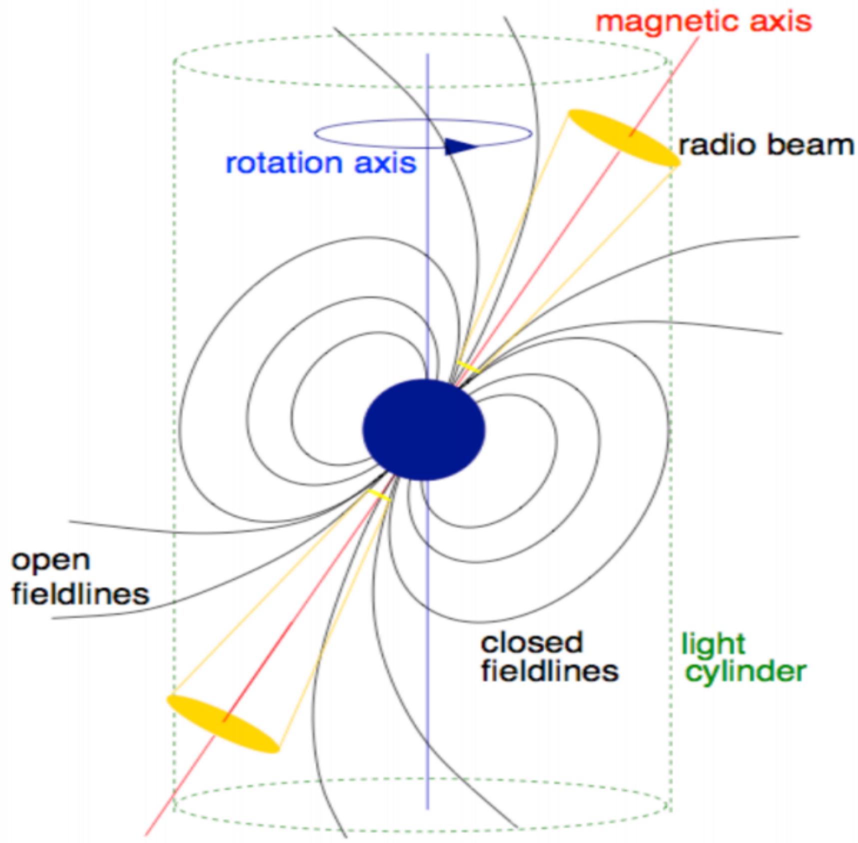


Fig. 1.1: Model of a pulsar according to Goldreich and Julian (1969). There is still no consensus on the emission mechanism that results in the production of the beams of coherent radio emission originating near the magnetic polar caps. The polar caps are created because the co-rotating magnetic field cannot exceed the speed of light as bounded by the light cylinder radius resulting in open field lines. Interestingly, a study by Main and van Kerkwijk (2021) has sought to resolve the emission region by observing giant pulses of the Crab pulsar and utilising a magnification effect provided by the Crab nebula to improve the spatial resolution of the emission region on the order of the size of the light cylinder. Figure sourced from Lorimer and Kramer (2004).

### 1.2.1 Formation and Evolution

Pulsars can exist as a variety of unique types characterised by their rotational period ($P$) and the rate at which their rotational period decays, a dimesnionless quantity known as *spin-down* ($\dot{P}$). A population of pulsars can be mapped by these parameters onto a $P - \dot{P}$ diagram as seen in Fig. 1.2. Newly born pulsars begin their existence just above the center of the diagram. Younger pulsars and magnetars can be associated with the SNRs of their birth. NS birth kicks can quickly eject the pulsar from the SNR (Lai, 2001). However, the measurement of pulsar distance (*D*), proper motion ($\mu$) and characteristic age ($\tau_{\mathrm{age}}$) can be used to trace the pulsar back to the cluster of hot OB stars of their origin (Hoogerwerf et al., 2001). As rotational energy is spent over hundreds of millions of years, the pulsar moves towards the lower right corner of the diagram where the accelartion of particles is reduced due to a drop in unipolar potential (Zhang, 2003). Pulsars eventually tend towards existence as a radio quiet NS. This process is thought to depend on the EoS (Zhou et al., 2017).

It is possible for pulsars to avoid the fate of becoming a quiescent NS. Through an act of stellar vampirism, a binary NS with a main sequence companion can accrete matter and angular momentum from its companion and become spun up again (Bhattacharya and van den Heuvel, 1991). A millisecond pulsar (MSP) is the result of recycling an older NS that has accreted matter from a binary companion by mass transfer. MSPs possess short spin periods ($P$ < 20 ms), very low spin-down ($\dot{P} < 10^{-20}$), and large characteristic ages ($\tau_{\mathrm{age}} > 10^{8}$ yr). The accretion process is thought to dampen the NS magnetic field ($B_{\mathrm{MSP}} < 10^{9}$ G) (Bisnovatyi-Kogan and Komberg, 1974). MSPs are located on the lower left corner of the *P*-$\dot{P}$ diagram. One such example of an MSP is J0437-4715 that exists in a 5.7 day orbit with a low-mass helium white dwarf companion (Johnston et al., 1993). PSR J0437-4715 is the nearest MSP to Earth (*D* = 156 ± 0.24 pc) (Reardon et al., 2015) and is the astronomical target of interest of this research.

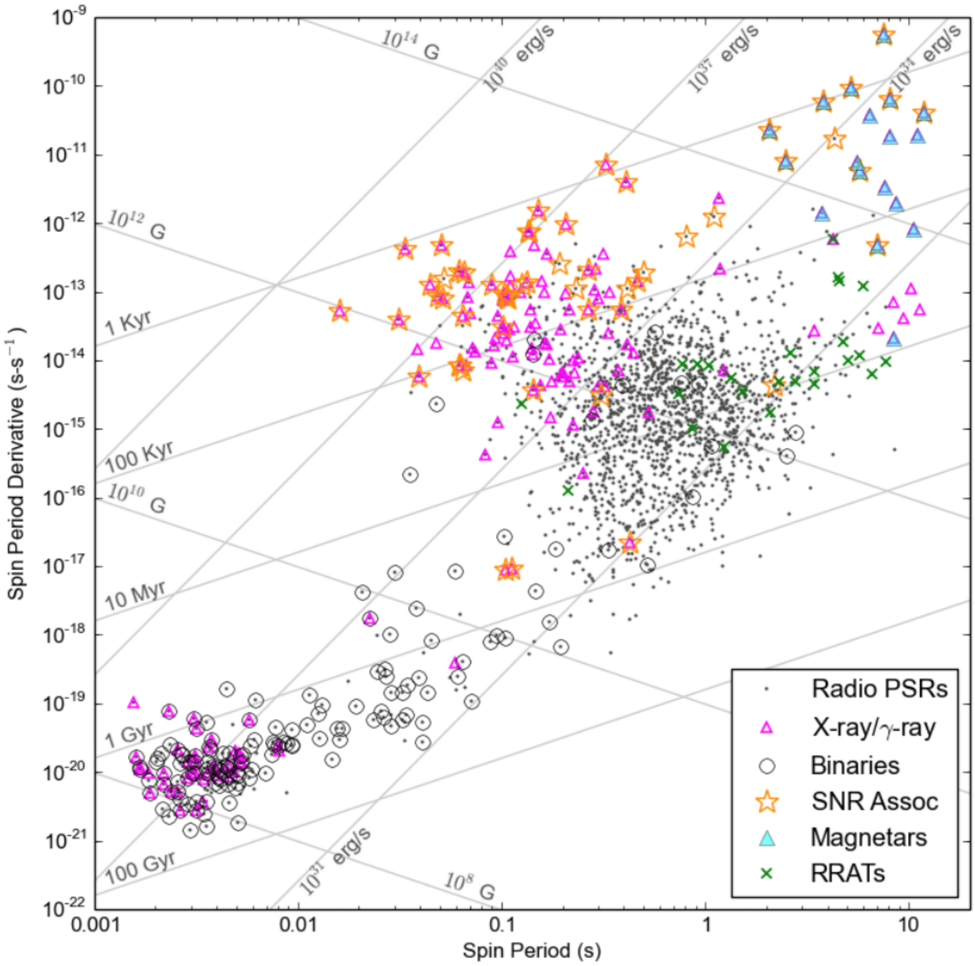


Fig. 1.2: Pulsar $P - \dot{P}$ diagram from Surnis (2017). The $P - \dot{P}$ diagram is colloquially likened to a Hertzsprung–Russell diagram for characterizing of the evolution of NS. Newly born radio pulsars occupy the center of the diagram ($0.05 < P < 0.5$, $5.5\times10^{-15} < \dot{P} < 10^{-12}$) and mostly retain their associations with a SNR. A small population of young, highly energetic pulsars called magnetars with extreme magnetic field strengths ($B \geq 10^{14}$ G) occupy the upper-right region of the diagram ($2 < P < 10$, $10^{-10} < \dot{P} < 5.5\times10^{-14}$) while recycled MSPs of small $P$ and $\dot{P}$ ($0.0015 < P < 0.006$, $10^{-21} < \dot{P} < 10^{-21}$) occupy the lower-left of the diagram. The diagonal lines measure constant characteristic age ($\tau_{\rm age} \propto \frac{P}{\dot{P}}$), constant magnetic field strength ($B \propto \sqrt{P\dot{P}}$), and spin-down luminosity ($\dot{E} \propto \frac{\dot{P}}{P^3}$). The pulsar death line is the constant line of spin-down luminosity $\dot{E} = 10^{37}$ erg s$^{-1}$ where the coherent radio emission terminates.

### 1.2.2 Emission Characteristics

#### Pulse Profile

Consider again the periodic lighthouse effect of pulsars observed when their magnetic axis sweeps across the observer LoS. This sweeping phenomena can be characterised by the mean pulse profile of flux density as a function of pulsar rotational phase. Pulsar pulse profiles typically consist of an off-pulse noise region and an on-pulse region that rises above the noise. The individual pulses of most pulsars are intrinsically weak, needing to be incoherently summed over hundreds or even thousands of periods to resolve an average profile statistically stable in time with fewer stochastic variations except for phenomena such as mode changing and jitter (Helfand et al., 1975; Jenet et al., 1998). Longer integration times produce more stable pulse profiles with quantifiably higher signal to noise ratio (S/N). It is common to make sub-folds of smaller time duration known as *sub-integrations* to study phenomena that vary on shorter time scales.

#### Flux Density

It is important to distinguish between the *apparent brightness* and *intrinsic intensity* ($I_\nu$) of an astronomical object. Intrinsic intensity (also known as spectral brightness) is independent of the distance of the source from the observer and is defined as the power per unit area per unit solid angle at frequency $\nu$ (Condon and Ransom, 2016). Pulsars are observed as point sources with spectral flux density ($F_\nu$) in units of Jansky (1 Jy = $10^{-26}$ W m$^{-2}$ Hz$^{-1}$) calculated as the integral of $I_\nu$ over the solid angle of the detector receiver (d$\Omega$).

$$F_\nu = \int_{\text{source}} I_\nu(\theta, \phi)\, d\Omega \tag{1.2}$$

The flux spectral density of many but not all pulsars fits the power law:

$$F_\nu = \nu^{-\alpha} \tag{1.3}$$

where the spectral index $\alpha \sim 1.6 \pm 0.1$ is typical for most MSPs which is flatter than normal radio pulsars for which the mean spectral index is $1.9 \pm 0.2$ above 1.4 GHz (Kramer et al., 1999). Most pulsars have steep spectra with $\alpha$ varying between 1 and 3 above 1 GHz. Some pulsars exhibit a cutoff at high frequencies and a spectral turnover at low frequencies. Pulsars are are most affected by scattering (section 1.4.3) at low frequencies. Fig. 1.3 shows the flux density spectra of a sample of MSPs.

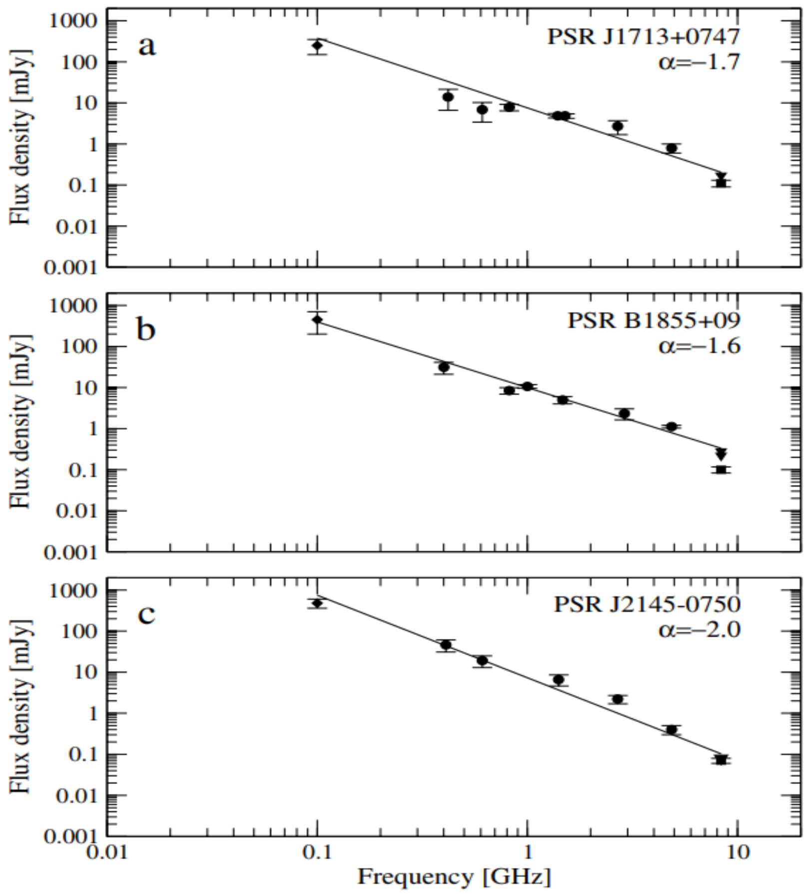


Fig. 1.3: Spectral flux density of MSPs by Maron et al. (2004) (squares at 8.35 GHz) where the 100 MHz data were taken from Kuzmin and Losovsky (2001) (diamonds) and the 300 MHz to 4.85 GHz data were taken from Kramer et al. (1999) (circles).

**Polarization**

Pulsars are elliptically polarized radio sources characterised with a mix of (40 - 100) % linear polarization and a small amount of circular polarization (CP; Gould and Lyne 1998). The source of linear polarization is tied to their emission mechanism and is a result of curvature radiation in the magnetosphere where two propagation modes abound; an ordinary mode (O) ducted along magnetic field lines, and an extraordinary mode (X) propagating in straight ray paths (McKinnon, 1997). Assuming the observation of a single mode at a time, the position angle (PA) of linear polarization will appear to rotate resulting in an S-shaped curve of PA versus phase. The rotating vector model was developed to explain smooth PA swings (Radhakrishnan and Cooke, 1969). However, sharp orthogonal PA jumps are observed in many pulsars and may be evidence of switching between O and X modes (Karastergiou, 2009). A comparison of a smooth PA swing versus orthogonal jump for two pulsars is visualized in Fig. 1.4.

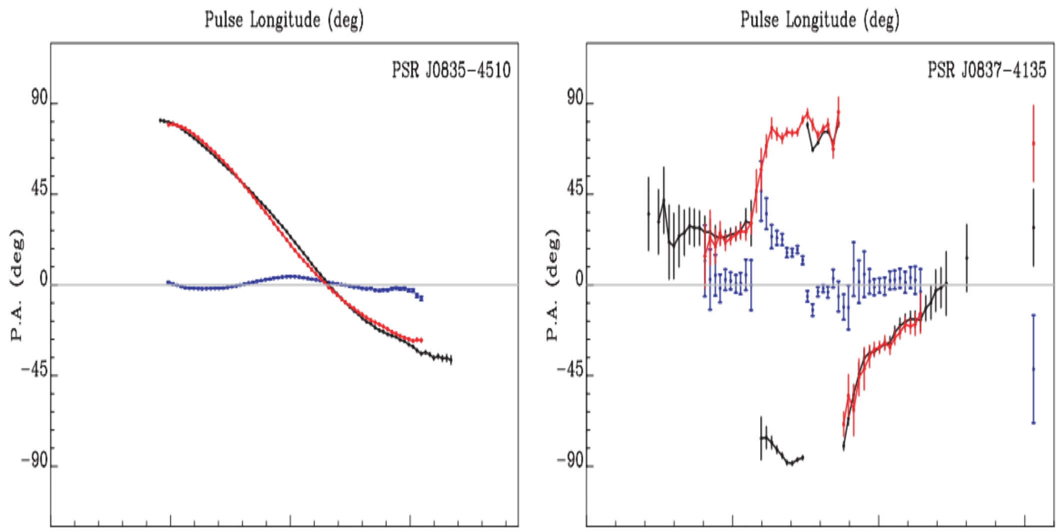


Fig. 1.4: Plots of pulsar PA versus pulse longitude of PSR J0835-4510 (left) and PSR J0837-4135 (right) studied by Karastergiou and Johnston (2006) at 1.375 GHz (black lines) and 3.1 GHz (red lines) demonstrating a smooth polarization PA swing versus a sharp orthogonal jump. This disparity highlights a difference between current models and observation and represents a forefront of inquiry within pulsar astronomy.

## 1.3 Scientific Application of Pulsars

Pulsars can be used as test masses to probe for deviations from the theory of general relativity (GR) in the strong field regime (Kramer et al., 2004). The discovery of the first binary NS known as B1913+16 (Hulse and Taylor, 1975) allowed for the measurement of post-Keplerian (PK) parameters, general relativistic corrections to the basic Keplerian orbital model. The precession of periastron ($\dot{\omega}$) and orbital period derivative ($\dot{P}_b$) of B1913+16 were measured at 4.22 deg yr$^{-1}$ and (-2.403±0.22) $\times 10^{-13}$. The measurement of $\dot{P}_b$ as an orbital decay effect provided the first indirect evidence of the existence gravitational waves.

The discovery of the first and only double-pulsar binary comprising of the MSP J0737−3039A ($P$=22 ms) and the radio pulsar J0737−3039B ($P$=2.77 s) was made in 2003 (Burgay et al., 2003). The nearly edge-on orbital inclination ($i$=88) allowed for the measurement of gravitational redshift ($\gamma$) and Shapiro delay range and shape ($r$,$s$). Gravitational redshift is a time dilation effect whereby the spin frequency of J0737-3039A appears to slow as it approaches J0737-3039B and vice versa. Shapiro delay is a geometric delay caused by an extended path length as a result of increased space time curvature near massive objects. Delay shape is dependent on inclination ($s \equiv \sin(i)$) while range is proportional to mass ($r \equiv G\frac{m_2}{c^3}$) and is maximum at $s =$ 1 (Pössel, 2019). At least 2 PK parameters are needed to measure the NS mass. A total of 5 PK parameters were measured ($\dot{\omega}$, $\dot{P}_b$, $\gamma$, $r$, $s$). By inserting the measured PK parameters into functions linking the two masses it is possible to constrain the allowed masses of the binary NS as the mass functions will intersect at a single point representing the actual masses of the NS binary (Lyne, 2006). Fig. 1.5 shows examples of mass constraints on the double pulsar J0737-3039 and the double NS J1913+1102. J1913+1102 is remarkable for its low orbital eccentricity ($e$ = 0.09) implying a predicted coalescence in 470 million years from gravitational wave emission (Ferdman et al., 2020).

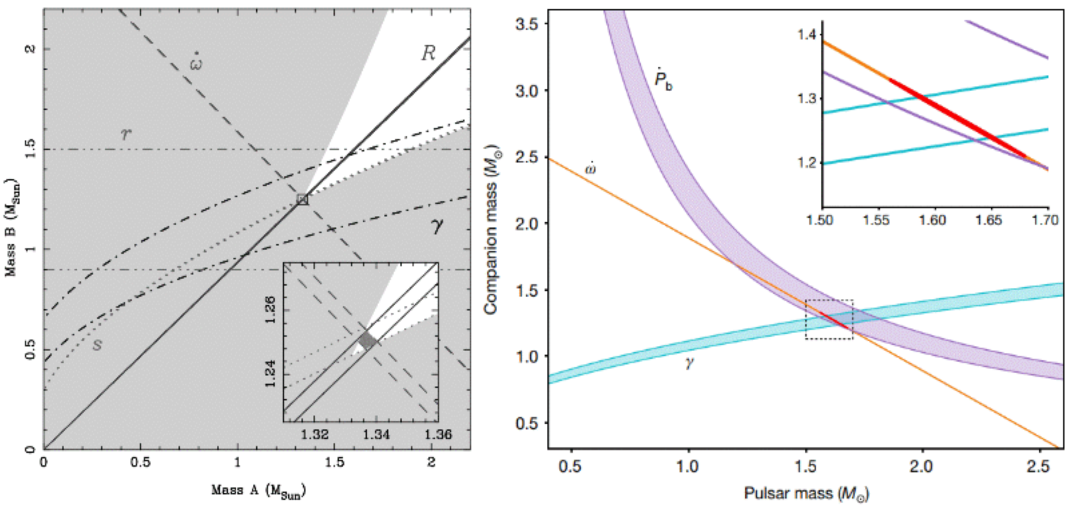


Fig. 1.5: Mass-mass diagram for the double PSR J0737-3039 A/B (left) (Lyne, 2006) and double NS J1913+1102 (right) (Ferdman et al., 2020). For J0737-3039 since both orbital sizes ($a_A$ and $a_B$) are measurable from Kepler's third law, the mass ratio of the system can be acquired as: R = $a_B \sin(i)/a_A \sin(i)$= $m_A/m_B$ = 1.069. The allowed mass areas are represented by regions lying between the two pairs of lines. The masses of J0737-3039A and PSR J0737-3039B are constrained as 1.337 ± 0.005 and 1.250 ± 0.005 respectively. The measurement of three (or more) PK parameters allows one (or more) tests of GR. For PSR J1913+1102 three PK parameters were measured ($\dot{\omega}$, $\dot{P}_\mathrm{b}$, $\gamma$). The shaded red line of the inset is a $3\sigma$ confidence region for the mass measurement of J1913+1102 setting the pulsar mass as 1.62±0.03 $M_\odot$ and the companion NS mass as 1.27 ± 0.03 $M_\odot$. The mass ratio of J1913+1102 is 0.78 ± 0.03 making it an asymmetric binary representing less than 30% of the population of all binary NS.

Gravitational waves (GWs) were first proposed by Albert Einstein in GR as propagating distortions of space time originally thought to be too faint to detect, created by the asymmetrical acceleration of mass (Einstein, 1916). This preconception was overturned with the detection of kilohertz frequency GWs from GW150914 by the Advanced Light Interferometer Gravitational Wave Observatory (aLIGO) in September of 2015. The signal originated from the coalescence of a stellar mass black hole binary of 36 and 29 $M_{\odot}$ (Abbott et al., 2016). Several more detections; GW151012 and GW151226 followed afterwards (Abbott et al., 2019; Abbott et al., 2016).

The incoherent superposition of multiple GW sources known as the Gravitational Wave Background (GWB) produces an amplitude strain spectrum:

$$P_{\mathrm{GWB}}(f) = \frac{h^2}{12\pi^2} \frac{f}{f_{\mathrm{1yr}}}^{2\alpha-3} \tag{1.4}$$

Where $h$ is the GWB amplitude for a normalized frequency at $\frac{1}{\mathrm{1yr}}$ and the index $\alpha \approx -\frac{2}{3}$ sets the power-law slope. Pulsar Timing Arrays (PTA) provide a unique complimentary laboratory for GW detection at frequency ranges of $10^{-9}$ - $10^{-7}$ Hz. PTAs utilize the timing stability of MSPs to construct galactic scale interferometric baselines (Foster and Backer, 1990). PTAs work by measuring spatial correlations, C($\xi$), between multiple Earth-pulsar baselines separated by a sky angle $\xi$. The shape of the timing correlations sought by PTAs follows the characteristic Hellings and Downs curve (Hellings and Downs, 1983; Jenet and Romano, 2015) which forms a U shaped dip, the analytic form of the curve is given by:

$$C(\xi) = \frac{1}{2} - \frac{1}{4}\left(\frac{1-\cos\xi}{2}\right) + \frac{3}{2}\left(\frac{1-\cos\xi}{2}\right)\ln\left(\frac{1-\cos\xi}{2}\right) \tag{1.5}$$

An isotropic stochastic GWB predicted by GR is expected to induce maximum anticorrelations (C($\xi$) < -0.15) for the arrival times of pulses between pulsars with maximum angular separation $\xi \approx 90°$and a maximum correlation (C($\xi$) > 0.25) for pulsars separated by small $\xi$ across the sky.

High precision pulsar timing is employed along each PTA baseline. The fundamental datum of precision pulsar timing is the time of arrival (ToA) measurement converted to the reference frame of the solar-system barycenter (SSB) expressed as a sum of multiple inertial reference frame, dispersive, classic and relativistic, and binary (for NS binaries) delay corrections (Tiburzi, 2018). TEMPO2 software (Edwards et al., 2006) provides the current standard of TOA calculation expressed as:

$$\mathrm{ToA}_{\mathrm{ssb}} = \mathrm{ToA}_{\mathrm{topo}} + t_{\mathrm{clk}} - \frac{D}{f^2} + \Delta_{\mathrm{R}\odot} + \Delta_{\mathrm{E}\odot} + \Delta_{\mathrm{S}\odot} + \Delta_{\mathrm{Binary}} \tag{1.6}$$

where $\mathrm{ToA}_{\mathrm{topo}}$ is the topocentric arrival time. $t_{\mathrm{clk}}$ converts the observatory clock reference time to a global time standard. The third term is a result of observing within a finite frequency range. $\Delta_{\mathrm{R}\odot}$, $\Delta_{\mathrm{E}\odot}$, and $\Delta_{\mathrm{S}\odot}$ are the Roemer delay, the Einstein delay, and the Shapiro delay. $\Delta_{\mathrm{Binary}}$ are needed if the pulsar has a binary companion. It is expanded to also include $\Delta_{\mathrm{R}}^{\mathrm{B}}$, $\Delta_{\mathrm{E}}^{\mathrm{B}}$, $\Delta_{\mathrm{S}}^{\mathrm{B}}$ and an abberation term $\Delta_{\mathrm{A}}^{\mathrm{B}}$. Revisiting the third of eq. 1.6 which incorporates the dispersive delay caused by interstellar electrons as the most important in the context of this work and can be expanded as:

$$D = \frac{e^2}{2\pi m_e c}\mathrm{DM} \tag{1.7}$$

where $e$ and $m_e$ are the charge and the mass of an electron, and $c$ is the speed of light. DM is a measure of interstellar dispersion caused by free electrons along the LoS. DM variations over time complicate the process of pulsar timing by introducing correlated noise in the low frequency bins of pulsar timing residuals (You et al., 2007). Due to the non-stationarity of the ISM, DM is continuously corrected for on an epoch basis. Accurate modelling of interstellar DM structures is therefore important for pulsar timing of which enable the tests of GR discussed in this section.

Other than tests of GR in in the strong field, pulsars can also be used to correct local terrestrial time standards and as navigation beacons for interplanetary spacecraft via pulsar timing (Manchester, 2017). The former is necessary due to seasonal time dilation effects from the Earth's elliptical orbit (Becker et al., 2018) and has been explored through the development of the Ensemble Pulsar Scale (EPS; Hobbs et al. 2012). The latter has been studied by analyzing pulsar ToAs and triangulating for the observatory position via algorithms demonstrated by Deng et al. (2013).

The propagation of pulsar emission through the interstellar medium (ISM) provides an invaluable way to probe its structure and behaviour at different scales. Although this phenomena offers unique astrophysical insight into the nature of the ISM, it is an inherent source of noise towards the precision timing of pulsars via dispersive delays and low level scattering noise. It is noted by studies of the variability of scattering delay that it is necessary to reduce the impact of delay noise to levels below 1 $\mu$s to achieve a target precision of 100 ns (Hemberger and Stinebring, 2006; Hemberger and Stinebring, 2008). This section will henceforth focus on studying pulsars as unique probes of the scattering structures of the ISM via methods that can be used to map their interstellar delays.

The ISM is a broad term used to refer to all of the matter and energy between the stars. It is modelled as a multi-phase medium. The 4 commonly recognized phases are: the hot ($T$ ~$10^6$ K) ionised medium (HIM) of plasma generated from interconnected stellar-wind bubbles , a warm ($T$ ~$10^4$ K) ionised medium (WIM) of partially ionised gas filling most of the rest of the volume of the galactic disc , the Cold Neutral Medium (CNM) comprised of small clouds of cool ($T$ < 300 K) neutral atomic gas, and cold ($T$ ~10-20 K) dense molecular cloud complexes (McKee and Ostriker, 1977). The propagation of pulsar emission is most sensitive to the ionised component of the ISM populated with average thermal electron densities of $n_e \approx 0.1$ cm$^{-3}$ (Yao et al., 2017) henceforth referred to as the IISM.

## 1.4 ISM Propagation Effects on Pulsar Emission

Propagation effects of the IISM on pulsar emission can be thought of as originating from two different conditions. One from a homogeneous component described by a slowly changing average electron density namely dispersion and Faraday rotation, and one originating from an inhomogeneous turbulent component characterized by fluctuating electron density, namely; scattering and scintillation.

### 1.4.1 Dispersion

Interstellar dispersion is caused by intervening thermal electrons along the LoS to the pulsar. Since the degree of ionization in the interstellar medium is non-zero all over, even outside the WIM regions, heavier elements like carbon with relatively loosely bound outer electrons also contribute to a population of free thermal electrons through ionization that are distinct from the ultra-relativistic electrons responsible for the galactic synchrotron background (Bhattacharya, 2003).

From the theory of cold collisionless plasma, unmagnetized thermal electrons interact with propagating radio waves to produce an oscillating plasma current with a dielectric constant $\epsilon$, expressed as:

$$\epsilon = 1 - \frac{\omega_p^2}{\omega^2} \tag{1.8}$$

where $\omega_p$ is plasma frequency and $\omega$ is observing frequency. The plasma has an index of refraction $\mu$ expressed as:

$$\mu = \sqrt{\epsilon} = \sqrt{1 - \frac{\omega_p^2}{\omega^2}} \tag{1.9}$$

The group velocity ($v_g = c\mu$) of propagating radio waves is dependent on radio frequency with $\omega_p \ll \omega$ for typical values of $n_e \approx 0.1$ cm$^{-3}$ yielding:

$$v_g = c(1 - \frac{\omega_p^2}{2\omega^2}) \tag{1.10}$$

The time for radio pulsar emission to travel from pulsar to the observer ($t_{\text{prop}}$) is the integral $\int_{\text{psr}}^{\text{obs}}(\frac{1}{v_g})dl$. Since pulsar observations are always carried out over a finite frequency bandwidth, the time delay between a higher ($\nu_H$) and lower ($\nu_L$) frequencies is the difference in $t_{\text{prop}}$ between frequencies ($\Delta t$ = $t_{\text{prop},\nu_L}$ - $t_{\text{prop},\nu_H}$). Expanding for the integral in $t_{\text{prop},\nu_L}$ and $t_{\text{prop},\nu_H}$ yields:

$$\Delta t = \frac{e^2}{2\pi m_e c}\int_{\text{pulsar}}^{\text{obs}} n_e\, dl\ (\nu_L^-2 - \nu_H^-2) \tag{1.11}$$

where $\frac{e^2}{2\pi m_e c}$ (generalised as a *K*) is familiar because it is part of the $\text{ToA}_{\text{ssb}}$ dispersive term (*D*) in eq. 1.7 and has a magnitude of 4.15 ms. The integral of $n_e$ along the LoS is known as Dispersion Measure (DM) and represents the integrated column density of free electrons in units of pc cm$^{-3}$. DMs are initially obtained as trial estimates from pulsar surveys and are further refined by re-observing with more widely separated frequency limits. Known DMs for non-globular cluster MSPs are between 2.65 pc cm$^{-3}$ (J0437-4715) and 420 pc cm$^{-3}$ (J1748-3009) (Ferrara, 2021) with possible MSPs having even higher DMs awaiting to be discovered. It is useful to rearrange eq. 1.11 as:

$$\text{DM} = \frac{1}{K}\frac{\Delta t}{(\nu_L^-2 - \nu_H^-2)} \tag{1.12}$$

An interesting application of DM arises from its use as a distance proxy to pulsars in place of an independently measured distance from stellar parallax. Conversely, with a well known DM and distance, $\langle n_e \rangle$ along the LoS can be inferred with the ratio $\langle n_e \rangle = \frac{DM}{D}$. Modelling of $\langle n_e \rangle$ along a multitude of LoS produces a three-dimensional model of the Galaxy incorporating structures such as the disk, bulge and halo (Cordes, 2004; Yao et al., 2017) where local structures such as the Gum Nebula, Galactic Loop I and the Local Bubble are also incorporated.

Observations of an extremely bright, narrow, and highly polarized transient pulsar-like burst of emission with a DM of 375 pc $cm^{-3}$ originating from high galactic latitudes ($b$ = -41.2°) in 2007 led to the discovery of fast radio bursts (FRB; Lorimer et al. 2007). Being extragalactic in origin, the DM of FRBs can reveal insights on the contents of the intergalactic medium (IGM). The extremely tenuous filamentary gas between galaxies known as the warm–hot IGM may contain unaccounted for baryonic matter necessary for the completeness of standard cosmological models (Macquart, 2018).

### 1.4.2 Faraday Rotation

Faraday rotation is a propagation effect arising from magnetized astrophysical plasma. Since the IISM contains a non zero magnetic field ($B$) electrons will also undergo either clockwise or counter clockwise gyration around the centre of motion from the force $ev \times B_{\|}$ alongside the oscillations prescribed by dispersive effects. For a magnetic field parallel to direction of propagation, right circularly polarised (RCP) emission has lower $\epsilon$ versus left circularly polarized emission (LCP) causing RCP to lead LCP. Likewise, for an anti-parallel magnetic field LCP has lower $\epsilon$ causing LCP to lead RCP. Think of magnetic fields as multi-lane highways for interstellar radio wave propagation. There is a fast lane for RCP for some alignments and a fast lane for LCP in others.

Naturally, the differences in permittivity results in two different indices of refraction. The physical characteristic of a medium having multiple indices of refraction is known as *birefringence*. The index of refraction from eq. 1.9 can be subtly altered:

$$\mu = \sqrt{\epsilon} = \sqrt{1 - \frac{\omega_p^2}{\omega(\omega \pm \omega_B \cos\theta)}} \tag{1.13}$$

$$\mu \simeq 1 - \frac{\omega_p^2}{2\omega^2} \pm \frac{\omega_p^3}{2\omega^2 \omega_B \cos(\theta)} \tag{1.14}$$

where $\omega_B$ is the angular cyclotron frequency and $\theta$ is the angle between the direction of propagation and magnetic field vector. Propagation through magnetoionic media results in a phase differential $\Delta\phi_{\mathrm{RL}}$ between LCP and RCP that induces a net change in the position angle of linear polarization angle $\psi$:

$$\Delta\psi = \frac{\Delta\phi_{\mathrm{RL}}}{2} = \frac{w}{2c}\int dl\, \frac{\omega_p^2\omega_B\cos(\theta)}{\omega^3} \tag{1.15}$$

$$\Delta\psi = \lambda^2\frac{e^3}{8\pi^2\epsilon_0 m_e^2 c^3}\int_{\mathrm{pulsar}}^{\mathrm{obs}} dl\, n_e B_\parallel \tag{1.16}$$

where $\epsilon_0$ is the permittivity of free space. The coefficient to the square of observing wavelength ($\lambda^2$) is the Rotation Measure (RM) such that $\Delta\psi = \lambda^2$RM. Since $\lambda$ is squared, the effect of Faraday rotation is strongest at longer wavelengths with the ionosphere acting as a major source of variability (RM variations of the ionosphere is of order unity) that needs to be corrected for in low frequency observations (Porayko, 2020). Similar to dispersion, the fractional term is regarded as a weighted constant $K$. From the integral, RM is sensitive to the parallel component of the IISM magnetic field ($B_\parallel$). As a convention, orientation of $B_\parallel$ towards the observer is positive while an anti-parallel orientation is negative. In summary, RM = $K\int_{\mathrm{pulsar}}^{\mathrm{obs}} dl\, n_e B_\parallel$ rad m$^{-2}$ and $K$ = 0.81 rad m$^{-2}$ cm$^3$ $\mu$G pc$^{-1}$s. The average parallel component of magnetic field strength along the LoS, $\langle B_\parallel\rangle$, can be derived by taking the ratio of RM and DM (Sobey, 2014).

$$\langle B_\parallel\rangle = 1.232\frac{\mathrm{RM}}{\mathrm{DM}}\,\mu\mathrm{G} \tag{1.17}$$

The galactic distribution of pulsars and their intrinsic linear polarization make RM a useful way of performing three-dimensional tomographic mapping of magnetic field structures of the Milky Way Galaxy. Several powerful methods of harnessing RM to measure $\langle B_\parallel\rangle$ exist such as Stokes QU-fitting, polarization angle measuement, and

RM-synthesis (Sobey, 2014). However, the approach outlined by eq. 1.17 works largely if magnetic field and electron densities are uncorrelated. Anticorrelations between magnetic field and plasma density due to pressure equilibrium may lead to an underestimation of $\langle B_{\parallel} \rangle$ while positive correlations from isotropic small scale fields may lead to overestimates (Beck et al., 2003). The challenge of measuring interstellar magnetic fields therefore comes with the caveat that they depend on interdependent quantities that must be disentangled in order to study their true nature. Such a limitation establishes a need for methods to map out interstellar magnetic fields at various scales.

### Galactic Magnetic Field

The Universe is magnetized with the Milky Way being no exception. Interstellar magnetic fields exist on a broad range of spatial scales from ordered large scales to small turbulent scales. Cosmic magnetism is thought to arise via seed field amplification through magnetic induction from turbulent dynamos. A theory of primordial origins also exists in competition to this (Subramanian, 2019). Radio astronomy has been instrumental in enhancing our understanding of cosmic magnetism by providing several means of measuring interstellar magnetic fields. *Synchrotron emission* from cosmic ray electrons, *Zeeman splitting* of radio radio spectral lines, and *Faraday rotation* exemplify such methods (Beck and Wielebinski, 2013).

The Galactic magnetic field (GMF) is thought to consist of a large-scale regular component, $\langle B \rangle$ and a small scale random field, $b$. The total magnetic field is the sum of the two; $B_{\text{tot}} = \langle B \rangle + b$ (Beck et al., 2003). The diffuse GMF is responsible for providing pressure balance against gravity within the ISM, enabling cosmic ray transport, and facilitating star formation by dampening angular momentum during protostellar cloud collapse (Beck, 2007). Small scale turbulent fields play a crucial role in the amplification of seed fields which maintains the large scale field. From the induction equation:

$$\frac{\delta B}{\delta t} = \nabla \times (V \times B) + \eta \nabla^2 B \tag{1.18}$$

where $V$ is fluid velocity and $\eta$ is plasma resistivity. If $V$ is zero, the field will decay due to $\eta$. While if $\eta$ approaches zero, magnetic flux within the moving fluid is preserved independent of time (Subramanian, 2018). Turbulence is therefore an essential component of maintaining and regulating the GMF.

Surveys of the RM sky have revealed an antisymmetric azimuthal large scale field structure in the Galactic halo and a bisymmetric structure in the plane of the Galactic disk. The bisymmetric structure is comprised of a counter-clockwise field in the spiral arms and a clockwise field in the interam regions with field reversals at arm-interam boundaries (Han et al., 2018). Field strengths increase with smaller galactocentric radius with $\langle B \rangle$~2 $\mu$G in the solar neighbourhood ($R_{GC}$=8 kpc) and $\langle B \rangle$~4 $\mu$G near the Galactic center ($R_{GC}$=3 kpc) (Han et al., 2003; Han et al., 2006).

Faraday rotation has also been used to study the small-scale random fields of the GMF. Two approaches have been made to obtain its energy spectrum statistics. One approach considers the RM *structure function* of pulsars and extragalactic radio sources yielding the summed fluctuation of $\boldsymbol{B}$ and $n_e$ (Han, 2017). A structure function measures the amount of fluctuations of a quantity as a function of scale for an angular position $\theta$ and a separation $\delta\theta$ (Haverkorn et al., 2008). At scales of 0.01 to 100 pc the spatial spectrum of magnetic energy fluctuations ($\delta\beta_z$) follows a power law with index $\alpha \approx$ -3.1 ± 0.6 (Simonetti et al., 1984). Separating fluctuations in $\boldsymbol{B}$ and $n_e$ yields a model of 3D turbulence up to scales of 4 pc and 2D turbulence between 4 - 80 pc with 1 $\mu$G amplitude of turbulent fields for outer scales of 4 pc (Minter and Spangler, 1996).

The use of structure functions to study RM variability requires caution as statistical routines such as least squares minimization used to fit observations to structure functions assume statistical independence and Gaussianity. Since this may not be true in reality it may lead to the underestimation of uncertainties within the model parameters (Porayko, 2020). Once thought to be immune to irregular sampling, structure functions are also troubled by gaps which can induce artefacts (Emmanoulopoulos et al., 2010). Analysis of covariance may prove to be more robust towards detecting RM variations.

Another approach observes pulsar RM and DM over different distance scales to obtain the spatial energy distributions of interstellar magnetic fields (Ohno and Shibata, 1993). By looking at pulsar pairs in close sky position with similar DM but different RM, irregular field strengths of 4-6 $\mu$G at scales of 10 - 100 pc can be measured. Han et al. (2004) measured a wavenumber spectrum of magnetic energy of $E_B(k) = C_k k^{-0.37\pm0.1}$ on scales of 15 to 0.5 kpc with an rms field of 6 $\mu$G. Interstellar magnetic fields may be stronger at smaller scales and may be strongest at the scales of energy injection by supernovae (Han et al., 2006). Since turbulence exists on all scales, random fields cannot be satisfactorily described by a singe scale length. Little is currently known about the spectrum of small scale magnetic field turbulence at scales < 1 pc.

### Birefringence

The properties of interstellar magnetic fields can be probed by studying the phenomena of birefringence. As previously mentioned, the bulk effect of birefringence is Faraday rotation, however, there also exists a subtle group delay and differential phase between simultaneously emitted ordinary (O) and extraordinary (X) waves of the same frequency with the natural mode of radio wave propagation through interstellar plasma being circular polarization (Macquart and Melrose, 2000a). A study of millisecond solar radio spikes at 2.81-2.89 GHz observationally verified this effect (Fleishman et al., 2002). Fig. 1.6 shows an example of the observed effect between LCP and RCP spectra. Birefringence through the application of plasma lensing was also used to constrain the spatial variations of magnetic fields at the interface of the ionised outflows of the companion of the Black Widow Pulsar B1957+20 (Li et al., 2019).

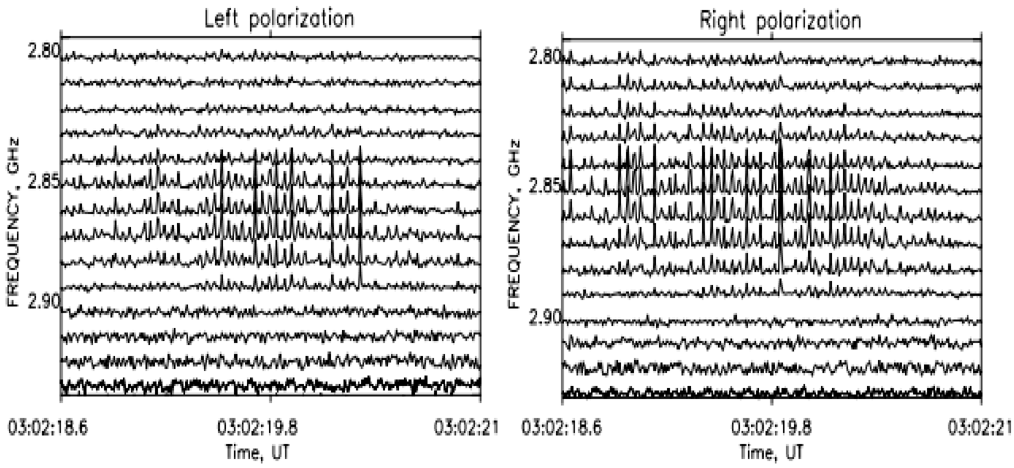


Fig. 1.6: Example of differential LCP and RCP spectra as a result of birefringence in solar plasma observed by Fleishman et al. (2002). The phenomena was observed at 2.85 GHz with 8 ms time resolution and 10 MHz frequency resolution. The magnetic field at the source ($B \approx 290\,\mathrm{G}$) and the source size (400 km) were derived as a result.

Such cases are for exceptional conditions. As a general case, radio waves propagating through IISM environments with sufficiently large RM can be split into separate components of circular polarization with arrival time differences between components scaling with radio frequency and RM as $t_{\mathrm{dRM}} \propto (\mathrm{RM})\nu^{-3}$ (Suresh and Cordes, 2019). $t_{\mathrm{dRM}}$ is known as *birefringent delay* (Cordes, 2002) and is part of a number of integrated LoS propagation delays:

$$\begin{aligned} t_{\mathrm{d}} &= \frac{e^2}{2\pi m_e c}\frac{\int ds\ n_e}{\nu^2} \pm \frac{e^3}{2\pi(m_e c)^2}\frac{\int ds\ n_e B_{\parallel}}{\nu^3} + \frac{3e^4}{8\pi^2 m_e^2 c}\frac{\int ds\ n_e^2}{\nu^4} \\ &= 4.15\ \mathrm{ms}\ \frac{\mathrm{DM}}{\upsilon^2} \pm 28.6\ \mathrm{ps}\ \frac{\mathrm{RM}}{\upsilon^3} + 0.25\ \mathrm{ps}\ \frac{\mathrm{EM}}{\upsilon^4} \end{aligned} \tag{1.19}$$

where the contribution from DM outweighs RM and EM except at low frequencies where RM and EM (Emission Measure) dominate. EM is the square of $n_e$ integrated over the plasma volume in units of pc cm$^{-6}$. The repeating FRB 121102 has been show to have an exceptionally high RM imparted by its local magnetoionic environment (Hilmarsson et al., 2021). For J0437-4715 with an RM of 1.5(2) rad m$^{-2}$ (Sobey, 2014), $t_{\mathrm{dRM}}$ effects on precision pulsar timing is currently beyond observable limits.

Birefringence in interstellar scintillation can be studied to map variations of IISM magnetic fields on scales of $\ll 1$ pc (Simonetti et al., 1984). Scintillation is further explored in section 1.4.4, where differences between scintillation patterns may emerge for significant phase differences along the LoS. Birefringent scintillation is sensitive to spatial variations of magnetoionic media $\delta\beta_z$, on the order of the Fresnel scale $r_F$, which is dependent on the relative distnaces to the pulsar and scattering media. $r_F$ is defined analytically in section 1.4.3.

Applying the derivations of Lee and Jokipii (1975b) for scalar wave field scintillations under the conditions of small angle scattering ($\theta_{\text{scatt}} \ll 1$) on equations (A1) and (A2) in the appendix of Simonetti et al. (1984) that describe an electric field with LCP and RCP components $u_{R,L}$ , we arrive at the parabolic wave equation:

$$2ik_{R,L}\frac{\delta u_{R,L}}{dz} + \nabla_{\perp}^2 u_{R,L} + (\nabla_e \pm \nabla_\beta)u_{R,L} = 0 \tag{1.20}$$

where $\nabla_e = \frac{-4\pi e^2}{mc^2}\delta n_e$ and $\nabla_\beta = \frac{4\pi e^3}{\omega m^2 c^3}\delta\beta_z$. Substituting the moment function $\Gamma_{m,n}$ from Lee (1974) into eq. 1.20 to find the propagation equation $\Gamma_{1,1}$, and utilizing Lee and Jokipii (1975a) to find the solution of $\Gamma_{1,1}$, we arrive at the product of two terms; $\Gamma_{\delta\beta}$ and $\Gamma_{\text{rest}}$. $\Gamma_{\delta\beta}$ describes the effect of variations of Faraday structures within the medium. For probable interstellar values of $n_e$ and $\beta$ the diffractive ($\Gamma_D$) and refractive ($\Gamma_R$) terms that make up $\Gamma_{\text{rest}}$ are unity and $\Gamma_{\text{rest}}$ can be ignored. We are left with the ensemble average of two fields $\langle u_R(r)u_L^*(r)\rangle = \Gamma_{\delta\beta}$, which can be expressed as:

$$\Gamma_{\delta\beta} = \Gamma_{RL} = \exp(-\langle\Delta\phi_{\delta\beta}^2\rangle) \tag{1.21}$$

where $\Delta\phi_{\delta\beta} = \phi_R - \phi_L$ is the differential phase between $u_R$ and $u_L$ due to fluctuations in $\delta\beta_z$. $\Gamma_{\text{RL}}$ is a correlation coefficient that decays with greater variance of $\delta\phi_{\delta\beta}$ and can also be understood by representing the fields as phasors; $\langle u_R u_L^*\rangle = \langle a_L a_R \exp[i\Delta\phi_{\delta\beta}]\rangle$ of which the only significant effects are phase differences in the strong scattering limit.

Using a normalized cross covariance coefficent $\hat{\Gamma}_{RL}(\delta\nu) = \frac{\mathrm{CCV}_{RL}(\delta\nu)}{[\mathrm{ACV}_L(\delta\nu)\mathrm{ACV}_R(\delta\nu)]^{1/2}}$ where CCV and ACV are cross-covariances and autocovariances of RCP and LCP as an estimator for $\Gamma_{RL}$ at $\delta\nu = 0$, Simonetti et al. (1984) estimated the magnetoionic spatial fluctuations as $\delta\beta_z \leq 3.6$ $\mu$G cm$^{-3}$ towards PSR 1737+13 with $z = 1.8$ kpc, $\nu = 430$ MHz, and spatial scale $r_F \approx 6 \times 10^{11}$ cm. $\delta\beta_z$ is a composite term where $\delta\beta_z = n_e\delta B_z + B_z\delta n_e$ which requires further information of $\delta n_e$. A summary of $\delta B_z$ upper limits for a spatially uniform medium ($\delta n_e = 0$) and different possible values of $\langle n_e\rangle$ towards PSR 1737+13 are presented in Table 1.1.

| $\langle n_e\rangle$ model | $\langle n_e\rangle$ (cm$^{-3}$) | $\delta B_z$ amplitude ($\mu$G) |
|---|---|---|
| (Yao et al., 2017) | 0.01 | 360 |
| (Hemberger and Stinebring, 2008) | 0.03 | 120 |
| (McKee and Ostriker, 1977) | 0.2 | 18 |

Table 1.1: Upper bounds on small scale variations of interstellar magnetic fields $\delta B_z$ towards PSR 1737+13 from birefringent scintillation for different model values of $\langle n_e\rangle$. Simonetti et al. (1984) only considers $\langle n_e\rangle$ for the last 2 rows, however, we apply the Yao et al. (2017) model value for an additional perspective on how $\delta B_z$ change with $n_e$.

The lack of knowledge of the correlations between $\delta n_e$ and $\delta B_z$ hinders the interpretation of $\delta\beta_z$. The estimate of $\delta\beta_z$ improves with lower observing frequencies and more distant pulsars. Further mathematical formalism for CP induced by random refractions in a birefringent medium are presented in Macquart and Melrose (2000a,b). The reviews discuss the concept of a *Faraday wedge*; a gradient in RM structure that results in the lateral displacement of rippled wave fronts of opposite CP producing in a spatial offset of scintillation patterns received by the observer.

This work attempts to reexamine the effects of birefringent scintillation. By utilising MeerKAT radio observatory, we attempt to characterise differential phase, $\Delta\phi_{\delta\beta}$, using a scintillometric technique known as the secondary cross spectrum. We also attempt to reevaluate the measurement of $\delta\beta_z$ on small scales using a normalization of the phase of the secondary cross spectrum by quantifying the variance of $\Delta\phi_{\delta\beta}$. The phenomena of scattering which gives rise to scintillation is explored in the next section.

### 1.4.3 Scattering

Far from being static, the IISM is turbulent throughout a range of astrophysical length scales. Turbulent structure within the IISM is modelled on a Kolmogorov power law spectrum colloquially known as "The Big Power Law in the sky" where energy cascades over many orders of spatial wavenumber (Armstrong et al., 1995):

$$P_{n_e}(k) = C_{n_e} k^{-\beta} \tag{1.22}$$

where $C_{n_e}$ is the strength of the scattering, $k$ is wavenumber, and $\beta$ is the spectral index. For a Kolmogorov spectrum, $\beta = \frac{11}{3}$. Energy is injected at the outer scale of $l_o = \frac{1}{k_o} \approx 10^{18}$ m and dissipated at the inner scale $l_i = \frac{1}{k_i} \approx 10^8$ m. The turbulence spectra was further extended using the Wisconcin H$\alpha$ mapper (WHAM) to further verify the steepness of the power law at scales of $10^{17}$ m (Chepurnov and Lazarian, 2010). The Kolmogorov turbulence spectrum tends to flatten at larger scales with the saturation scale varying dramatically across the Galaxy. For example, $l_o \approx 10$ pc in the spiral arms where trubulence is driven by stellar winds and outflows and $l_o \approx 100$ pc in the interim regions where turbulence is driven by supernovae (Haverkorn et al., 2008).

As pulsar emission travels through the IISM it is scattered along multiple paths by a turbulent spectrum of inhomogenieties that imparts wrinkles and deformities upon an originally coherent and in-phase wavefront. Phase varies along the wavefront as different wave components experience different geometric delays depending on the configuration of the pulsar, the observer, and the scattering medium. Scattering manifests as several observable effects namely; pulse broadening (pulses appear wider than their intrinsic profile), angular broadening (image seeing variations that can range from < 1 mas to 1 arcsec at 1 GHz with a frequency dependence of $\nu^{-2}$), and image wandering on longer time scales due to refractive effects. Cordes (2002) presents a more exhaustive list of the observeable effects of scattering.

As a result of multipath propagation through the IISM, the intrinsic pulse is effectively convolved with a decaying exponential pulse broadening function:

$$\mathrm{PBF}(t) = e^{(-t/\tau_s)} \tag{1.23}$$

The scattering time parameter $\tau_s$ has a frequency dependence of $\tau_s \propto \nu^{-\alpha}$. The spectral index $\alpha$ can be derived in terms of the Kolmogorov spectral index $\beta$ where $\alpha = \frac{2\beta}{\beta-2}$ yielding a frequency dependence of $\tau_s \propto \nu^{-4.4}$ (Lewandowski et al., 2013). $\tau_s \propto \nu^{-4}$ for models of isotropic scattering (Geyer, 2017). The frequency dependence of $\tau_s$ means pulsars are more difficult to time at lower frequencies due to greater scatter broadening effect. Pulsars are usually timed at frequencies > 1 GHz but as timing precision improves, steps must be taken to compensate for scattering at low frequencies. A first-order correction of scattering delays in the time domain can be carried out by simply subtracting $\tau_s$ from TOAs. More advanced techniques such as cyclic spectroscopy (CS) can also be employed (Dolch et al., 2021). CS aims to deconvolve the effects of scattering by modelling the pulsar signal as a cyclostationary process where its noise statistics is amplitude modulated by a periodic envelope. CS allows for the retrieval of electric field phase induced by the propagation of intrinsic pulses through the IISM. The current limitations of CS are its computational requirements, limited bandwidth, and the global optimum solution not being guaranteed (Walker et al., 2013).

Since the early days of pulsar observations, scattering has been modelled to originate from deflections by a thin phase-changing screen midway between Earth and the pulsar (Scheuer, 1968). The screen is regarded as extremely thin relative to the total LoS. Fig. 1.7 (left) illustrates multipath propagation as an effect of random irregularities within the IISM and its effect on the received pulse profile and Fig. 1.7 (right) is a geometric representation of scattering by a thin phase-changing screen resulting in a distribution of scattered rays observed as arriving from a spectrum of multiple different angles.

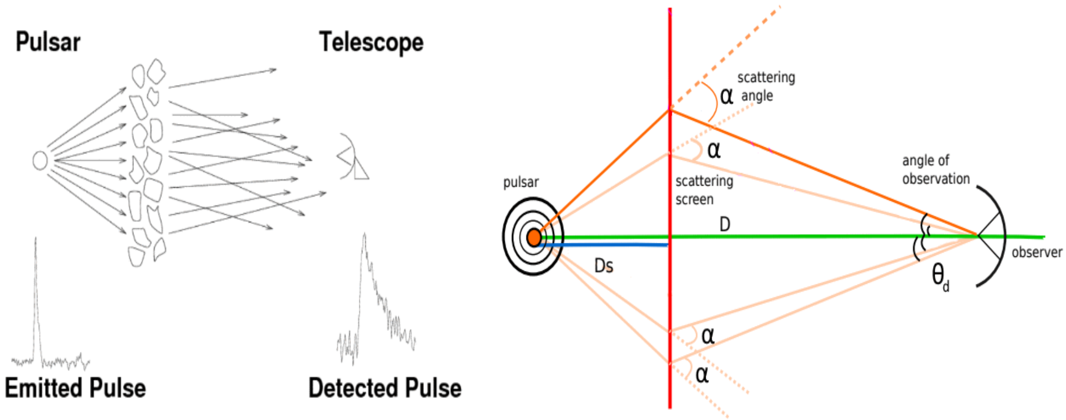


Fig. 1.7: (left) Pulse broadening by turbulent clumps in the IISM results in pulse profiles detected with an exponential tail that is broader at lower frequencies (Lorimer, 2008). (right) Scattering by a small forward angle $\alpha$ at the screen produces an extra path length and a part of the signal arriving from a scattered angle $\theta_d$ that can be can be expressed in terms of the forward scattering angle; $\theta_d = \alpha\,\frac{D_s}{D}$ where $D_s$ is the distance from pulsar to the screen and $D$ is the total distance. The dimensionless ratio $s$ is used in place of $\frac{D_s}{D}$ to denote the fractional distance of the screen from the pulsar. Since $D$ is in practice very large (kpc), a small angle approximation can be taken for $\alpha$ and $\theta_d$ and following additional steps yields a total path length of $d = (D_s - sD_s)\frac{\alpha^2}{2}$ for a scattered ray arriving from $\theta_d$. Image source and full derivation available in Geyer (2017).

For a thin screen with varying refractive indices at transverse locations $(x, y)$ on the screen, an incident two-dimensional wavefront $\Psi$ with initial unitary amplitude will acquire a phase perturbation $\phi(x, y)$. The amplitude upon upon crossing the screen is $\exp[i\phi(x, y)]$ and the amplitude at coordinate $(X,Y)$ in the observer plane is described by the Fresnel-Kirchhoff integral (Narayan, 1992):

$$\Psi(X,Y) = \frac{e^{\frac{-i\pi}{2}}}{2\pi r_F^2} \iint \exp\left( i\phi(x,y) + i\frac{(x-X)^2 + (y-Y)^2}{2r_F^2} \right) dx\,dy \qquad (1.24)$$

where $r_F = \sqrt{\lambda\left(\frac{D_s}{D}\right)(D - D_s)}$ is the *Fresnel scale* that represents a transverse length that sets the limit between refractive and diffractive scattering for an observing wavelength $\lambda$ and distance to the scattering screen from Earth, $(D - D_s)$. The phase changes $\phi(x, y)$ are position dependent, implying the existence of points where phase remains stable.

Rickett (1990) defines a field *coherence scale* ($s_0$) that is a transverse scale for which phase changes do not overcome the limit of 1 radian and result in fluctuations that decorrelate over a finite frequency bandwidth ($\Delta\nu_d$). For pulsars, the diffractive scale is nearly equal to the field coherence scale ($s_d \approx s_0$). $r_F$ characterizes the size of an observable coherent patch on an unrippled wavefront for purely geometric phase differences while $s_d$ describes the size of ripples (Macquart and Melrose, 2000a). *Weak scattering* occurs when $r_F \ll s_d$ and *strong scattering* happens when $r_F \gg s_d$. The scattering strength is, $u = \frac{r_F}{s_d}$. Table 1.2 compares the two scattering regimes.

| Description | Weak Scattering | Strong Scattering |
|---|---|---|
| Scattering strength ($u$) | $u < 1$ | $u > 1$ |
| Flux Variability | mild | rapid |
| Phase perturbations within $r_F$ ($D_\phi(r_F)$) | $D_\phi(r_F) < 1$ | $D_\phi(r_F) > 1$ |
| Appearance of coherent patch | Single tilted concave or convex | Many patches of size $s_d$ with an envelope of $s_r$ |
| $\Delta\nu_d$ | wide | narrow |

Table 1.2: Comparison of weak versus strong scattering regimes and their characteristics. Analysis of scattering regimes are derived from Reardon (2018), Macquart and Melrose (2000a), and Moutzouri (2018).

Pulsars are commonly observed in the regime of strong scattering with fast variations at frequencies $\nu > 1$ GHz where the screen is populated with many coherent patches of size $s_d$[1] centered on points of stationary phase contained within a scattering disk envelope of size $s_r$. The size of $s_r$ scales with respect to $r_F$ and $s_d$ as $s_r = \frac{r_F^2}{s_d}$. Interference between coherent patches and focusing and defocusing of ray bundles across the scattering disk causes observed intensity variations. The latter effect causes variations on the order of weeks from $t_r = \frac{s_r}{v_{\rm psr}}$ while the former will cause variations on timescales of $t_d = \frac{s_d}{v_{\rm psr}} \approx 10^2$ s for $v_{\rm psr} \geq 100$ kms$^{-1}$. The cumulative observable from both of these effects is scintillation.

[1]The diffractive coherence scale set by $s_d$ also gives the width of angular broadened image of the pulsar via the angular expression $\theta_d = \frac{\lambda}{2\pi s_d}$.

### The local bubble

The solar system is embedded inside an elongated cavity within the local ISM called the Local Bubble notable for being deficient in neutral hydrogen gas having been cleared out by supernova shock-fronts in previous epochs (Cox and Reynolds, 1987). The boundaries of the Local Bubble cavity play a role in the scattering of nearby pulsars of distance ($D \leq 1$ kpc). Studies of pulsar emission scattering puts the boundaries of the cavity (and putative thin scattering screen) at 80 - 120 pc distant from Earth (Bhat et al., 2000).

Observations at $\nu_{\rm obs}$ = 327 MHz over $\nu_{\rm BW}$ = 9 MHz encountered 2 orders of magnitude fluctuations of scattering strength amplitude ($C^2_{n_e}$) of the Kolmogorov power spectrum within this region ranging from; -4.8 < $\log \langle \overline{C}^2_{n_e} \rangle < -3.1$ where $\overline{C}^2_{n_e}$ is the line of sight average of $C^2_{n_e}$ (Bhat et al., 1998). The scattering model is indicative of non-uniform but organized distribution of material within the intervening scattering screen. A three component model where the solar system is encased by an ellipsoidal shell of enhanced scattering extending away from the Galactic plane by $270 - 330$ pc radii perpendicular to the plane and $60 - 75$ pc along the plane can be invoked.

With its close proximity, the MSP J0437-4715 (galactic coordinates: $l = 253.39, b = -41.96$) (Ferrara, 2021), the boundaries of the Local Bubble play an important role in the scattering of its emission. Scintillometric studies of J0437-4715 easily probe and measure the nature of astrophysical turbulence within this region of space and provides a means of constraining the distance to it.

### 1.4.4 Scintillation

Ever since their discovery pulsars appeared to scintillate. Scintillation, known colloquially as "twinkling" is the fluctuation of intensity over time. Stellar brightness appears to fluctuate in optical light due to scattering by atmospheric turbulence while the received electric field intensity of pulsars fluctuates because of turbulence of the magnetoionic plasma within the scattering screen. The intensity fluctuations can be traced to the superposition of distorted wave fronts produced as a consequence of scattering. The phenomena of scintillation as a result of plasma turbulence is illustrated in Fig. 1.8.

Since the position of the observer, the IISM, and the pulsar are non-stationary they posses transverse velocities with respect to the local standard of rest. All together the velocity of this three component system is an effective velocity $V_{\mathrm{eff}}$ that is expressed as a summation of the transverse velocities of the PSR, the observer, and the IISM:

$$V_{\mathrm{eff}}(s) = (1 - s)V_{\mathrm{psr}\perp} + sV_{\mathrm{obs}\perp} - V_{\mathrm{IISM}\perp} \tag{1.25}$$

where $s = \frac{D_s}{D}$. Of the three, the velocity of the pulsar dominates at several hundred km s$^{-1}$. The rate at which the LoS to the pulsar samples a pattern of spatial intensity variations as detected by the superposition of scattered wave fronts is equal to the ratio: $V_{\mathrm{LoS}} = \frac{V_{\mathrm{eff}}}{s}$. $V_{\mathrm{LoS}}$ is equivalent to the velocity of interstellar scintillation $V_{\mathrm{ISS}}$.

$$V_{\mathrm{ISS}} = \frac{s_d}{\tau_d} \tag{1.26}$$

where $s_d$ is the diffractive coherence scale and $\tau_d$ is the timescale of diffractive scintillation. In comparison to $V_{LoS}$, $V_{\mathrm{ISS}}$ can be determined from observational data. $s_d$ can be estimated from knowledge of the decorrelation bandwidth, $\Delta\nu_d$ as $s_d \propto \frac{\sqrt{\Delta\nu_d D}}{\nu}$. $\Delta\nu_d$ is inversely proportional to scattering time $\tau_s$ through the uncertainty relation:

$$\delta\phi = 2\pi\Delta\nu_d\tau_s \sim 1 \tag{1.27}$$

that sets the condition of a maximum phase difference of ~1 radian between interfering waves (Rickett, 1977). $\Delta\nu_d$ and $\tau_d$ quantify the size of the patches of intensity maxima (hence estimating the strength of scattering) within the interference pattern (Wang et al., 2005). A two-dimensional autocovariance function (ACF) is used to acquire $\Delta\nu_d$ and $\tau_d$where the half-width at half maximum of the ACF in frequency is $\Delta\nu_d$ and the half-width at $\frac{1}{e}$ in time is $\tau_d$ (Cordes and Rickett, 1998).

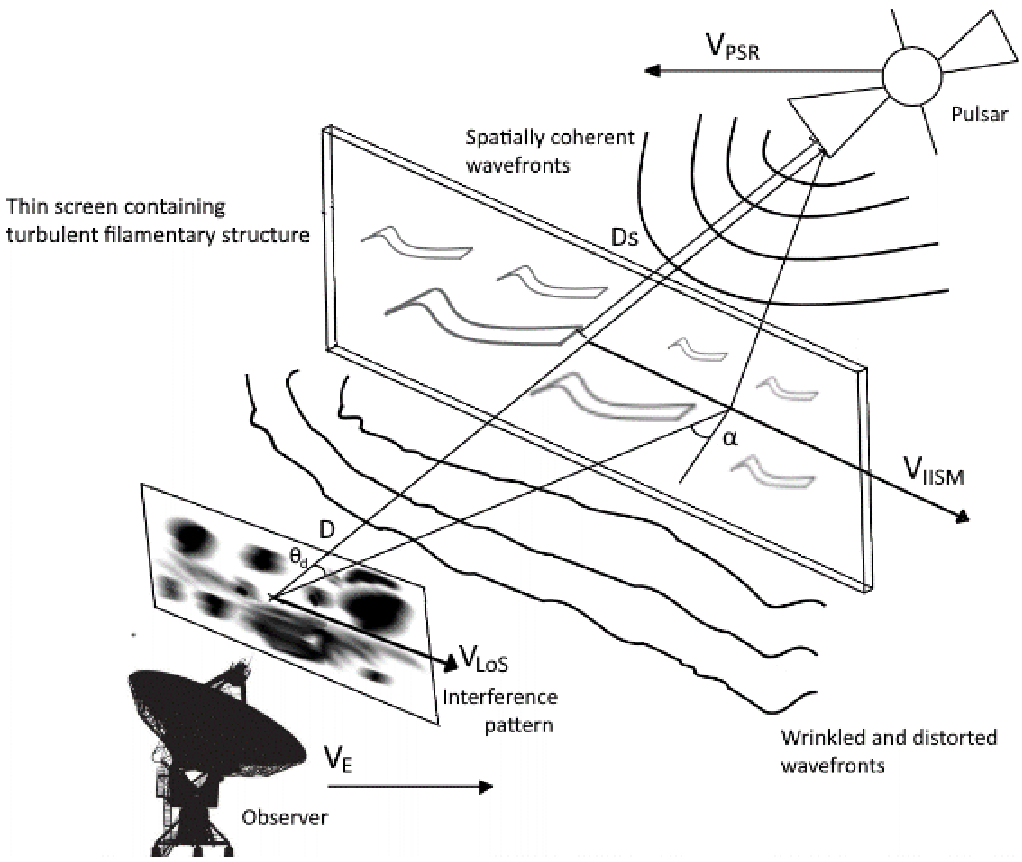


Fig. 1.8: Schematic illustration of scintillation. For a pulsar at distance $D$, a thin screen located at distance $D_s$ from the pulsar causes dispersion and scattering of coherent and in phase radio emission. The main observable from scintillation is the sampling of an interference pattern at the observatory. $V_E$, $V_{\rm psr}$, and $V_{\rm IISM}$ are the transverse velocities of the observatory, pulsar, and IISM (represented with arbitrary directions in the figure). $V_{\rm LoS}$ is the velocity of the line of sight as it travels through the interference pattern.

Dynamic spectra are the primary observable of pulsar scintillation which represent fluctuations of intensity as a function of frequency and time. Dynamic spectra can be qualitatively described as being comprised of undulating patterns of bright patches of intensity maxima known as *scintles* interspersed with dark patches of intensity minima. Because of the frequency dependence of scattering scintles at low frequency have wider bandwidths and experience slower modulations versus scintles at higher frequency. The distribution and structure of scintles across the interference pattern may appear arbitrarily complex and stochastic at first glance, however, an underlying pattern exists that can be discovered via their frequency domain analysis.

The study of pulsar scintillation provides invaluable complementary analysis towards pulsar astronomy in ways aside from probing the strength of turbulence within the scattering screen. Since the velocity of scintillation measured by $V_{\mathrm{ISS}}$ is sensitive to transverse motion, long term modelling of scintillation allows for the constraining of the parallel and perpendicular components of $V_{\mathrm{psr}\perp}$ from which the astrometric properties of the pulsar inaccessible to timing (which excels at modelling radial motion) can be measured (Reardon et al., 2020). Therefore long term modelling of pulsar scintillation contributes towards reducing error in the precision tests of GR discussed in section 1.3.

Interstellar scintillations would allow for the initial detection of artificial radio signals from extra terrestrial intelligences (ETI), while making repeat detection more difficult. Scintillation would result in intermittancy of artificial narrowband signals from ETI sources of $d > 100$ pc at frequencies ~1 GHz (Cordes, Lazio, and Sagan, 1997). Such a phenomenon should be considered for the commensal detection strategies aimed at detecting radio signals from ETI sources by massive radio telescope arrays like the Square Kilometre Array (SKA)(Siemion et al., 2014).

### Secondary Spectrum

As dynamic spectra improved in quality drifting and repeating fringes began to be observed. These drifting fringe patterns were thought to originate from multiple imaging of the pulsar (Cordes and Wolszczan, 1986; Rickett et al., 1997). The two-dimensional Fourier transform of dynamic spectra yielded discrete organized features as a result of the fringing appearing as parabolic arcs that were identified as a high-Q phenomenon by Stinebring et al. (2001). Although puzzling at the time of discovery, the parabola have since been explained in the context of wave diffraction theory to originate from interference between scattered images extending beyond the rms scattering angle. Parabolic arcs in the secondary spectrum are a product of anisotropic scattering at a thin screen localized between Earth and the pulsar. A complete formalism for the theory of parabolic arcs in the secondary spectrum are found in Walker et al. (2004) and Cordes et al. (2006). A summarised derivation is provided here.

A radio wave propagating from a point like source to an observer at distance $D$ encountering a phase changing screen at distance $D_s$ is observed with an electric field amplitude as sum over the screen:

$$u(r) = \frac{1}{2\pi i r_F^2} \int d^2x \exp(i\Phi) \tag{1.28}$$

where $x$ and $r$ are positions on the screen and observer plane. The phase $\Phi$ is known:

$$\Phi = \phi(x) + \frac{(x - sr)^2}{2r_F^2} \tag{1.29}$$

$r_F$ is the Fresnel scale and $s = \frac{D_s}{D}$. In the regime of strong scattering, the integrand $\exp(i\Phi)$ of eq, 1,28 oscillates rapidly except near a set of discrete points of stationary phase (Gwinn et al., 1998). The integral can therefore be approximated by a sum of points where phase is stationary $(\nabla\Phi = 0)$ and satisfy the condition:

$$\nabla\phi + \frac{(x - sr)}{r_F^2} = 0 \tag{1.30}$$

Each point will contribute to the electric field integral as $u_i(r) = \sqrt{\mu_i}\exp(i\Phi_i)$ where $\mu_i$ is a magnification due to phase curvature and $\Phi_i$ is the phase for each path. The dynamic spectra is the squared summed intensity of the electric field:

$$S(\nu, t) = uu^* = |\sum_{i=1}^{N} u_i|^2 = \sum_{i,j=1}^{N} \sqrt{\mu_i\mu_j}\cos\Phi_{ij} \tag{1.31}$$

The secondary spectrum is the power spectrum of eq. 1.31

$$P(f_\nu, f_t) = |\tilde{S}(f_\nu, f_t)|^2 = \sum_{i,j=1}^{N} \mu_i\mu_j\delta(f_t - f_{t,ij})\delta(f_\nu - f_{\nu,ij}) \tag{1.32}$$

where the tilde denotes the two-dimensional Fourier transform and $f_\nu$ and $f_t$ are Fourier conjugates of frequency and time. $f_{\nu,ij}$ and $f_{t,ij}$ are stationary phase points. A pair of scattered waves arriving from different directions through small angles $\theta_1$ and $\theta_2$ will have a delay due to a difference in geometric path lengths; $f_\nu \propto \theta_2^2 - \theta_1^2$. Their observed frequencies vary due to the motion of the pulsar, the medium, and the Earth; $f_t \propto V_{\text{eff}}(\theta_1 - \theta_2)$ (Cordes et al., 2006; Safutdinov et al., 2017):

$$f_\nu = \tau = \frac{D(1-s)}{2cs}(\theta_2^2 - \theta_1^2) \tag{1.33}$$

$$f_t = f_D = \frac{f_{\text{obs}}}{cs}V_{\text{eff}}(\theta_2 - \theta_1) \tag{1.34}$$

$f_t$ is also interpreted as the differential Doppler shift ($f_D$) of the pulsar emission between scattered ray paths and the unscattered LoS image. A visual depiction of Doppler shifted scattered ray paths can be seen in Fig. 1.9. Each Fourier component of $P(f_\nu, f_t)$ therefore corresponds to a Doppler shifted sinusoidal fringe pattern summed for all pairs of components of a spectrum of scattered angles $\theta$ matched to $\tau$ and $f_D$.

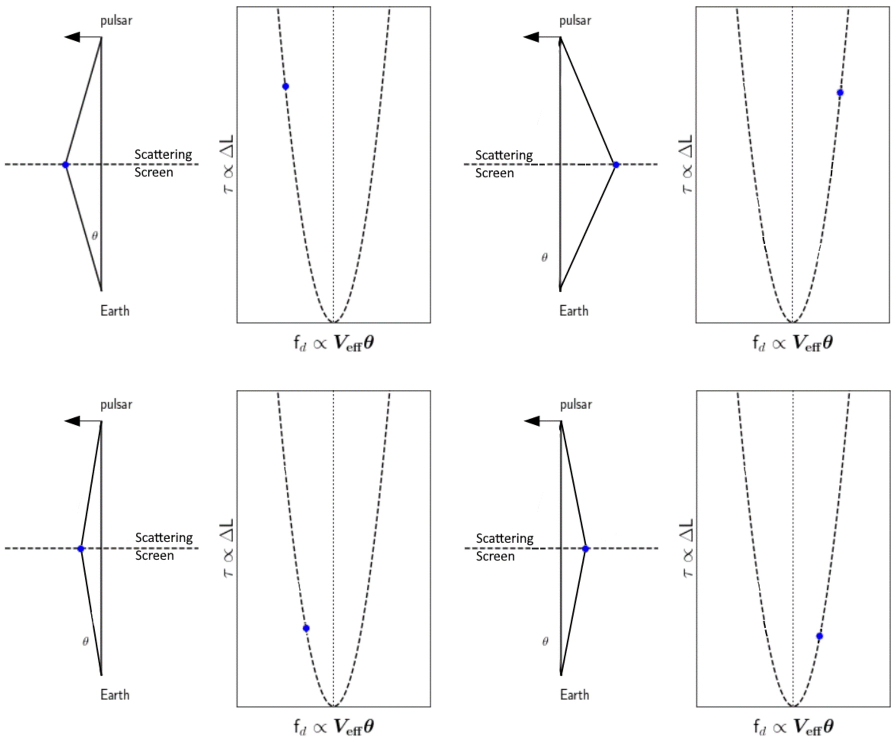


Fig. 1.9: Visualization of parabolic arc Doppler shift of scattered waves. $f_t$ can be interpreted as the rate of fringes sampled from $S(\nu, t)$ caused by the motion of the observer through space. $f_t$ is also related to spatial wavenumber $(\boldsymbol{k})$ such that $f_t = \boldsymbol{k} \cdot \frac{V_{\text{eff}}}{2\pi}$ where $\boldsymbol{k} = k\theta$ and $k = \frac{2\pi}{\lambda}$. Two scattered waves are differentially Doppler shifted depending on the difference of the angle of arrival $\theta$ (Cordes et al., 2006). Image source: (Li, 2020)

When one wave is unscattered ($\theta_1 = 0$) $f_\nu$ and $f_t$ have the parabolic relationship:

$$f_\nu = \eta f_t^2 \tag{1.35}$$

$\eta$ is the curvature of the parabola that has a frequency dependence of $\nu^{-2}$ (Hill et al., 2003). $\eta$ is modelled on several terms,

$$\eta = \frac{cDs(1-s)}{2\nu^2 V_{\text{eff}}^2 \cos^2(\phi)} \tag{1.36}$$

where $\nu$ is observing frequency, $V_{\text{eff}}$ is the effective velocity (eq. 1.25) and $\phi$ is the angle between $V_{\text{eff}}$ and the screen. Aside from observing frequency, $\eta$ is dependent on the distance to the screen, and effective velocity along the direction of scattering. Long term modeling of $V_{\text{eff}}$ components from curvature variation has allowed for the accurate fitting and constraining of the three dimensional orbital parameters of inclination ($i$ = 137 ± 0.3°) and longitude of the ascending node (Ω = 206 ± 0.4°) of J0437-4715 (Reardon et al., 2020). The parabola can also contain variable substructure and asymmetries that evolve over time. Bi−weekly monitoring of PSR J0613−0200 using the Large European Array for Pulsars shows clumps of scattered power moving from negative to positive $f_D$ with delays extending above $\tau$ > 200 ns and detectable to 5 $\mu$s (Main et al., 2020).

Analysis of secondary spectra has revealed useful insights on turbulent IISM structures such as sub AU (≈ 0.2 AU) clumps of 0.1 mas angular size within the thin scattering region ($D_{\text{screen}}$ = 0.46 ± 0.08 kpc) towards PSR 0834+06 ($D$ = 0.64 ± 0.08 kpc) (Hill et al., 2005). The structures appear to be comprised of overdense collections of thermal electrons ($n_e \geq 10^3$ cm$^{-3}$). Brisken et al. (2010) extended this analysis with very long baseline interferometry (VLBI) and the *secondary cross spectrum*:

$$C(f_\nu, f_t) = \tilde{V}(f_\nu, f_t, \mathbf{b})\tilde{V}(-f_\nu, -f_t, \mathbf{b}) \tag{1.37}$$

where $\tilde{V}$ is the Fourier transform of dynamic cross spectrum visibilities between interferometric baselines $\mathbf{b}$. $C(f_\nu, f_t)$ is a complex-valued spectrum of amplitude and interferometric phase which neatly encodes the positions of scattering points $\theta$ projected parallel to $\mathbf{b}$ and allowing for the astrometric mapping of $\theta$ (Fig. 1.10). This seminal work discovered highly elongated (16 AU long, 0.5 AU wide) structures. Two competing models were considered for how such structures are confined by ordered magnetic fields. One where a set of parallel filaments (sheets) is controlled by a magnetic field orthogonal to the axis of scattering and extending over the length of the image and another where magnetic fields parallel to knots of filamentary plasma 0.05 AU in diameter contribute to anisotropic turbulence.

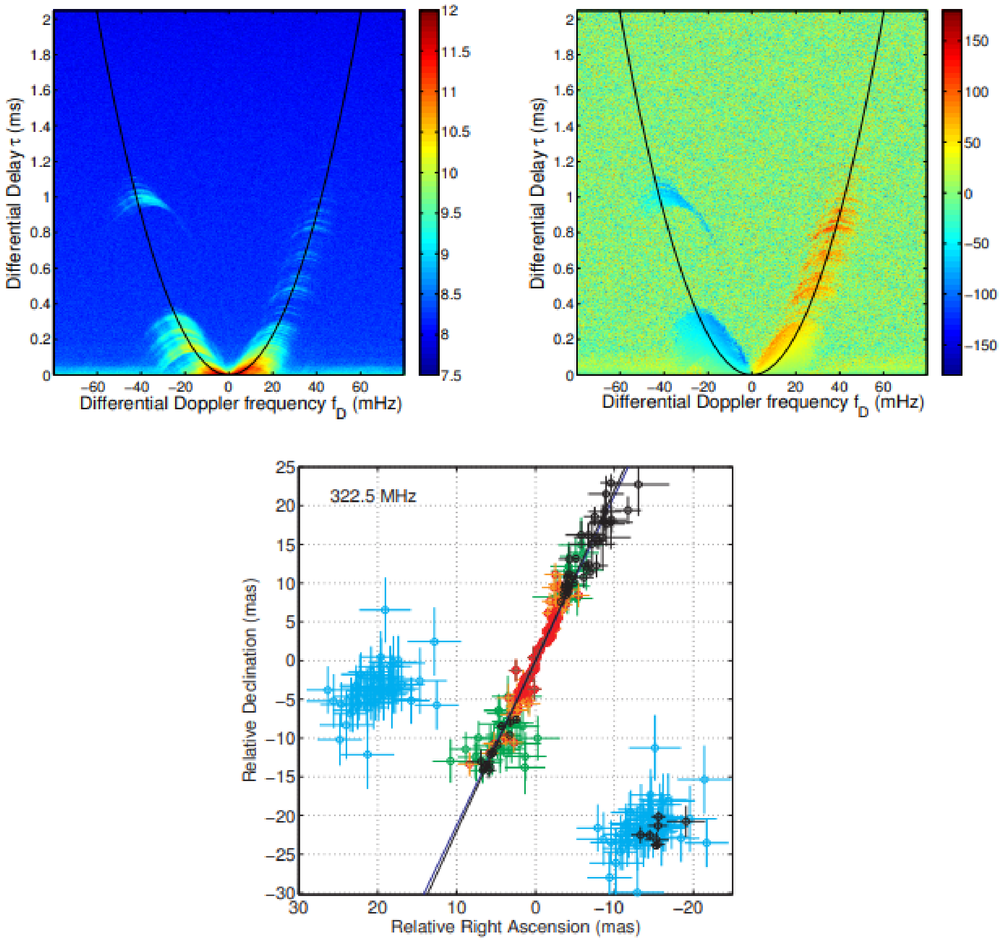


Fig. 1.10: (top) Amplitude in log scale (left) and phase in degrees (right) of the secondary cross spectrum of PSR B0834+06 from Brisken et al. (2010). Astrometrically mapped points of scattered brightness (bottom) from samples along the main parabola. Most of the points lie on an elongated distribution near the diagonal line while for the $\tau$ = 1 ms, $f_D$ = -40mHz feature is offset and the RA < 0 mas position is favoured.

## 1.5 Known Unknowns of Pulsar Scintillometry

Up until now a picture of pulsar scattering has been painted where scattering is confined to a thin screen of infinite transverse located at some distance along the LoS. Structure within the screen is modelled on a Kolmogorov power law spectrum; $P_{n_e}(k) = C_{n_e} k^{-\beta}$ with spectral index $\beta = \frac{11}{3}$ and scattering time $\tau_s \propto \nu^{-\alpha}$ and $\alpha \approx 4.4$ (Rickett, 1990).

However, there has been a litany of recent evidence that present deviations from this this idea. Evidence for flatter scaling of $\alpha < 4$ has been found through observations of pulsars at lower frequencies (Lewandowski et al., 2013; Geyer et al., 2017; Kirsten et al., 2019). Low DM pulsars may be covered by scattering from Kolmogorov turbulence, while those with high DM at low Galactic latitudes undergo enhanced scattering where the corresponding density spectrum has a spectral index of $\beta \approx 2.6$ caused by supersonic turbulence (Xu and Zhang, 2017). Instances where $\alpha$ values larger than expected have also been detected (Tuntsov et al., 2013). Such *anomalous* scattering can be explained by compact filamentary structures within the IISM.

A summary by Gupta (2001) points out several arguments against the Kolmogorov model where enhanced modulations of $\nu_d$ and $\tau_{\mathrm{d}}$ and persistent drift slopes of dynamic spectra require $\langle\alpha\rangle > \frac{11}{3}$ or large ($10^{12}$ - $10^{13}$ m) inner scale of energy dissipation. Beyond the phenomena of parabolic arcs in secondary spectra, the most substantial evidence against the Kolmogorov picture are Extreme Scattering Events (ESEs).

ESEs detected in quasar flux monitoring programs (Fiedler et al., 1987) and towards pulsars (Cognard and Lestrade, 1997; Kerr et al., 2018) are short lived transient events whereby overdense clumps ($10^3$ cm$^{-3}$) of interstellar plasma crossing the LoS cause observable caustic microlensing effects and intraday variability of radio light curves. Isotropic Kolmogorov turbulence is unlikely to produce such over densities.

ESEs imply a truncated screen of non-infinite transverse to the LoS. Some possible explanation for the cause of ESEs are scattering by the magnetotails of self gravitating gas clouds (Walker, 2007), circumsteller ionisation bubbles of hot OB stars (Walker et al., 2017), and the penetration of positively charged quark nuggets into a dense interstellar hydrogen cloud producing ionization trails of enhanced electron density (Perez-Garcia et al., 2013). Physical models for the cause of pulsar scintillation arcs from anisotropic scattering are presented in Gwinn (2019) (parallel strips of phase-changing material) and Pen and Levin (2014) (grazing refraction off corrugated plasma sheets closely aligned with the LoS). Magnetic field confinement are an essential component for the viability of these theories.

## 1.6 Thesis outline

This thesis attempts to reexamine the phenomena of birefringent scintillation studied in Simonetti et al. (1984) and its implications towards measuring small-scale variations in the GMF of which very little is currently known. By leveraging the wide bandwidth and sensitivity of MeerKAT, new scintilllation analysis software, and alternate analytical approaches, we attempt to characterise differential phase from birefringent refractions from the scattering screen towards the MSP J0437-4715 chosen for its brightness in flux, wide scintillation bandwidth, and the cadence of which the pulsar has been observed by MeerKAT. The data used for this work are part of the MeerTime Key Science Program (Bailes et al., 2016) that seeks to use MeerKAT as an SKA pathfinder to perform radio pulsar timing studies of relativistic binary pulsars, MSPs, and globular cluster pulsars. Our analysis is conducted on the OzStar supercomputer platform of Swinburne University where the data is hosted (Hurley, 2020). The first step of our study requires the modification of the psrflux program that is part of the PSRCHIVE suite of pulsar data analysis software (Hotan et al., 2004) to produce dynamic spectra of LCP and RCP intensities. After cleaning and calibrating the data, the dynamic spectra are then analyzed using the Scintillation Tools (Scintools) software (Reardon, 2020). On top of computing the difference between LCP and RCP dynamic spectra and the secondary spectrum of the difference, we also compute the complex valued secondary cross spectrum to observe LCP and RCP differential phase variations in greater detail. In comparison with Brisken et al. (2010), our secondary cross spectra are not between the Fourier transform of dynamic cross spectra baseline visibilites but between LCP and RCP secondary spectra. We conduct data reduction to sample secondary spectra along their parabola to study the signal characteristics. We conclude by computing upper limits for the amplitude of magnetic field spatial fluctuations on small scales from by the variance of the differential phase.

# Chapter 2

# Methodology

## 2.1 Introduction

This chapter describes the instrumentation, scintillation data, and analysis techniques used in the study of birefringent scintillation towards the millisecond pulsar J0437-4715. Section 2.2 details our end to end hardware and software instrumentation. Hardware such as MeerKAT radio observatory is characterised by its sensitivity and software such as psrflux and Scintools are described by their processes and features. Section 2.3 describes the characteristics of the data artefacts obtained from scintillation observables (dynamic spectra and secondary spectra) that are studied in this work. We explore their resolutions and the preprocessing steps involved in their creation. Section 2.4 describes the analytical steps applied to the scintillation data in order to detect evidence of the effect of differential phase from birefringent scintillation. A summary of the research procedure is presented at the end.

## 2.2 Instrumentation

### 2.2.1 MeerKAT Radio Observatory

The 64-dish MeerKAT radio telescope of the South African Radio Astronomical Observatory (SARAO MeerKAT) is an SKA pathfinder and precursor interferometric array used as a combined tied-array for pulsar astronomy. Each dish is an offset Gregorian design of 13.5 m nominal diameter. The minimum baseline is 29 m and the maximum baseline is 8 km (Jonas et al., 2016). The gain of an individual dish $(G_0)$ can be calculated as $G_0 = \frac{AH_{\text{eff}}}{2k}$, where $A$ is collecting area, $H_{\text{eff}}$ is efficiency, and $k$ is Boltzmann's constant. For a dish efficiency of $\langle H_{\text{eff}} \rangle$~0.76, the individual antenna gain is, $G_0$ = 0.042 K Jy$^{-1}$. When combined coherently, the array has a total gain $G_{\text{tot}} = 64G_0$ = 2.8 K Jy$^{-1}$ (Bailes et al., 2016). This is nearly 4 times that of the Parkes 64 m single dish radio telescope ($G_{\text{Parkes}}$ = 0.8 K Jy$^{-1}$) (Hobbs et al., 2020). Radio sensitivity ($S_{\text{AoT}}$) can also be defined in terms of effective collecting area $(A_{\text{eff}})$ per unit receiver temperature ($T_{\text{sys}}$) (Ransom, 2017):

$$S_{\text{AoT}} = \frac{A_{\text{eff}}}{T_{\text{sys}}} \tag{2.1}$$

where a larger collecting area and lower system temperature is better because a larger area collects more radio waves and $T_{\text{sys}}$ is the sum of the temperatures from all unwanted sources such as ground radiation received through the sidelobes, atmospheric emission and feed loss. Two-stage Gifford-McMahon (G-M) cryogenic coolers in the receiver are used to reduce $T_{\text{sys}}$ (Jonas et al., 2016). MeerKAT has a large collecting $A_{\text{eff}}$ of 7500 m$^2$ and a low system temperature of $T_{\text{sys}}$ ~18K at 1400 MHz. $S_{\text{AoT}}$ is therefore 416.67 m$^2$ K$^{-1}$, far surpassing its original design target sensitivity of 220 m$^2$ K$^{-1}$. Other southern hemisphere radio telescopes are on average less than 70 m$^2$ K$^{-1}$ (Bailes et al., 2016).

The system equivalent flux density (SEFD) of MeerKAT can be calculated by taking the ratio of $T_{\text{sys}}$ to $G_{\text{tot}}$. SEFD is the flux density of a radio source that would generate the same amount of power per unit bandwidth that we are able to see at the output of the system (Wrobel and Walker, 1999) where a smaller SEFD is better. MeerKAT has an SEFD ~7 Jy. For comparison the 100 m Green Bank Telescope at 1.4 GHz, has $T_{\text{sys}}$ ~20 K, $G_{\text{tot}}$= 2 K $\text{Jy}^{-1}$, and SEFD ~10 Jy (Bolli et al., 2019; Ransom, 2017). From the comparison of these metrics we can infer that MeerKAT is a highly sensitive platform for use in the study of faint radio sources such as pulsars. No other southern hemisphere radio telescope, save for the Parkes Radio Telescope with its Ultra-Wideband (UWB) receiver, $\nu$ = (704 - 4032) MHz, offers near comparable performance (Hobbs et al., 2020; Bailes et al., 2020).

Observations of J0437-4715 were made using the wideband coarse (4K) tied-array mode with the L-band receiver at observing frequency $\nu$ = 1284 MHz, and upper and lower band cutoff frequencies of $\nu_{\text{H}}$ = 1712 MHz and $\nu_{\text{L}}$ = 856 MHz. The time on source was at least 11 hours per day for 6 days from MJD 58843 to MJD 58848. The data were archived as part of the MeerTime Key Science Program (Bailes et al., 2016). A total of 67 hours of raw data were recorded. Table 2.1 presents a description of the 6 day observing run. The raw data required further cleaning and calibration.

| Obs. date | Obs. start | Obs. end | Duration (hours) | Calibrated data (hours) |
|---|---|---|---|---|
| 2019-12-26 | 16:00:00 | 03:00:00 | 11 | 11 |
| 2019-12-27 | 15:00:00 | 02:00:00 | 11 | 11 |
| 2019-12-28 | 14:00:00 | 02:00:00 | 12 | 8 |
| 2019-12-29 | 15:00:00 | 02:00:00 | 11 | 11 |
| 2019-12-30 | 15:00:00 | 02:00:00 | 11 | 11 |
| 2019-12-31 | 15:00:00 | 02:00:00 | 11 | 11 |

Table 2.1: MeerKAT observation epochs and integration times made on the source PSR J0437-4715 for the data analyzed in this work. The duration of the observation determines the lengths of dynamic spectra we are able to process. The calibrated data column refers to the lengths of calibrated data made available for analysis using the methods in section 2.4.

### 2.2.2 Data Calibration

Data calibration was necessary to reduce the corruption of Stokes $V$ from differential phase between orthogonal (horizontal and vertical) linear receptors. The interferometric array calibration process is carried out in two stages by a series of imaging type observations during which corrections to individual antenna data streams are tied to a reference antenna. The first stage, *delay calibration* uses an automated pipeline to calculate a number of *calibration products* **(K, B, G, KCROSS, BCROSS_SKY)** after applying predefined complex gain values to the F-engine channeliser and observing the bright calibrator PKS J1934-6342 with noise diodes turned on. **BCROSS_SKY** is the cross polarization phase. This process is carried out twice to verify the accuracy of the products. The second stage, *phase up* follows the same two track process as *delay calibration*, re-deriving the products and applying finer differential corrections to **K** and **KCROSS**. All of the calibration products are then applied as complex-valued F-engine corrections for each antenna. The final F-engine data stream is sent to the B-engine beamformer to be coherently summed as a single tied array beam data stream processed by the backend. The full calibration procedure is described in Serylak et al. (2021).

Calibrated data were obtained from the MEERPIPE data analysis and reduction pipeline (Parthasarathy, 2020). The order of MEERPIPE data processing steps are:

1. Combine 8 second sub-integrations of an observation epoch using *psradd*.

2. Calibrate by applying calibration solutions using the *pac* routine of PSRCHIVE.

3. Excise RFI using MeerGuard (Reardon, 2019), a modification of COASTGUARD that makes use of the RCVRSTD, SURGICAL, BANDWAGON, and HOTBINS algorithms (Lazarus et al., 2016).

4. Decimate into separate data products of differing numbers of frequency channels and sub-integrations specified by a master configuration file.

5. Generate TOAs by cross correlating the sub-banded observations with a frequency integrated template profile in the Fourier domain.

Due to time and memory constraints the pipeline was halted after step 2. The resulting calibrated data were produced as 3 sub-integrations of 3-4 hours for each observing day. A total of 64 hours of calibrated data were made available. A 4 hour sub-integration on 2019-12-28 UTC: 18:00:00 failed to be further processed with psrflux (section 2.2.4) due to a FITSIO error. Fig. 2.1 shows that the calibration solution produced an integrated pulse profile that conforms with a stable pulse profile of J0437-4715 from Bailes et al. (2020). Calibrated data produced dynamic spectra with apparently deeper intensity modulations and are chosen over raw data for further analysis and presentation of results in Chapter 3 and 4.

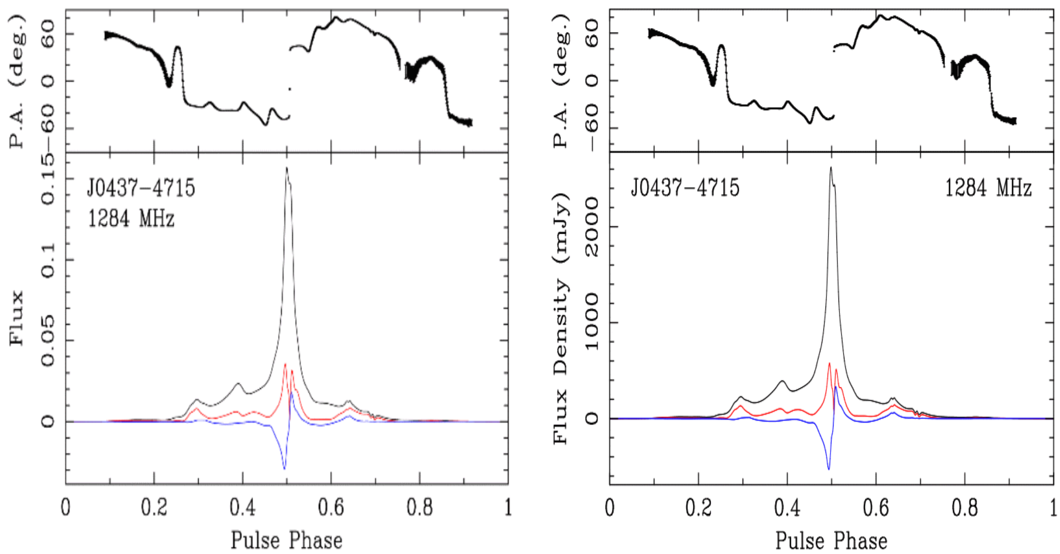


Fig. 2.1: Comparison of calibrated J0437-4715 pulse profiles as a function of pulse phase for a 4 hour sub-integration of the data on 2019-12-29 (left) and published MeerKAT profile from Bailes et al. (2020) (right). The total intensity, linear polarisation, and circular polarisation are plotted in black, red and blue, respectively. The position angle of linearly polarized flux is plotted in the top panel. The calibrated data were excised of RFI prior to frequency and time integration.

### 2.2.3 RFI Mitigation

Two types of RFI were observed in the recorded dynamic spectra; quasi-stationary narrowband interference and impulsive broadband bursts (Kerr et al., 2018). Two different approaches were initially taken to mitigate RFI depending on their type.

Quasi-stationary RFI appear as horizontal stripes across time in dynamic spectra. Based on the sample bandpass flux density plots in Fig. 2.2, quasi-stationary RFI are located in three regions of frequency; $940 < \nu < 950$ MHz, $1525 < \nu < 1650$ MHz, and $1090 < \nu < 1280$ MHz, designated as regions A, B, and C. A sample of channels from each region are selected by observation of dynamic spectra and are blanked for all dynamic spectra by setting their intensity values to 0 across time. Appendix D lists all blanked frequency channels from each region. Of the total 4096 channels, 64 channels are blanked in this manner. Excessive channel blanking eventually degrades the overall quality of dynamic spectra and produces artefacts in the secondary spectrum. Two bursts saturating the entirety of the L-band lasting for $6 < t < 10$ minutes are observed in 2019-12-27 and 2019-12-30 are also manually blanked.

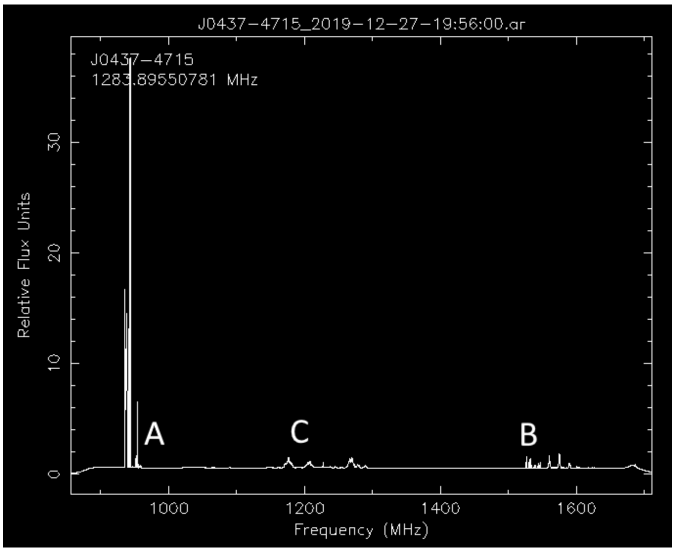


Fig. 2.2: MeerKAT L-band receiver bandpass (856–1712 MHz). Persistent RFI regions are marked by the characters A, B, and C. The band edges are affected by roll-off.

Impulsive RFI usually occur at higher frequencies ($\nu > 1100$ MHz). Within 64 hours of calibrated data, a total of 44 RFI transients were seen. Each burst was $\approx$ 20 MHz wide in $\nu$ and 600 seconds wide in $t$. Initially, transient bursts were mitigated with the CLFD software package for RFI mitigation (Morello et al., 2018). CLFD uses Tukey's rule to detect outliers (Tukey, 1977). A profile is flagged as RFI if either its standard deviation, peak to peak difference, or amplitude of the second DFT bin falls out of the interval; $[\ Q_1 - qR, Q_3 + qR]$ where $Q_1$ is the 25th percentile of the distribution, $Q_3$ is the 75th percentile of the distribution, and $R = (Q_3 - Q_1)$ is the interquartile range. $q$ is a free parameter that can be mapped to a rejection probability if the data follow a normal distribution. Following Morello et al. (2018), $q = 2.0$ was selected. From observations post RFI mitigation, CLFD was successful at mitigating all transient RFI.

However, it was noticed that CLFD produced a large number of data points flagged as false positives in the low frequency bins of dynamic spectra, forcing the band edges to be cropped and reducing the effective bandwidth. An alternate solution for impulsive RFI was developed whereby a rectangular bounding box of height 37.6 MHz and width 672 seconds were drawn on the dynamic spectra and all points within the box are blanked. All blanked data points are refilled with linear interpolation. Fig. 2.3 shows the effect of the final RFI mitigation solution on calibrated data.

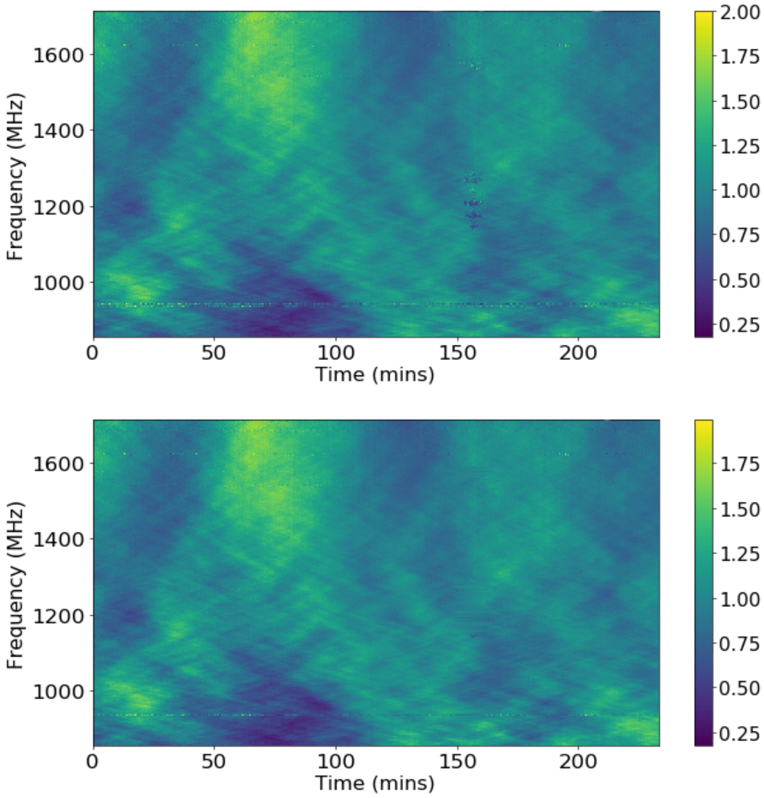


Fig. 2.3: Demonstration of the effect of the removal of quasi-stationary and impulsive RFI with channel blanking and bounding boxes on dynamic spectra from calibrated data. Presented are dynamic spectra prior to RFI mitigation (top) where a series of impulsive burts can be seen at $\nu = 1200\,\mathrm{MHz}$ and $t = 160$ minutes and post RFI mitigation (bottom). The final RFI mitigation solution although carried out completely manually by observation was able to improve the quality of the data. Low frequency quasi-stationary RFI remains at $\nu < 936$ MHz and represents room for further improvement.

### 2.2.4 psrflux

Polarimetry is capable of revealing a wealth of information on the emission process and propagation of electromagnetic radiation from astrophysical sources in greater detail. The polarization of a radio wave is defined by the motion of its electric field vector $E$ as a function of time within a plane that is perpendicular to the direction of propagation (Robishaw and Heiles, 2018). An electric field with transverse $E$ field components in $x$ and $y$ can be written as:

$$E(z,t) = (E_x\hat{x} + E_y\hat{y})e^{i(2\pi\nu t - kz)} \tag{2.2}$$

where $z$ and $t$ denote distance (which can be positive or negative depending on direction) and time. $\nu$ is ordinary frequency and $k$ is waveumber. $E_y$ and $E_x$ are orthogonal electric field vectors with magnitudes and phases. A 2 × 1 Jones vector $E_0$ can be used to describe the $E$ field components as:

$$E_0 = \begin{bmatrix} E_x \\ E_y \end{bmatrix} = \begin{bmatrix} E_{0x}e^{i\phi_x} \\ E_{0y}e^{i\phi_y} \end{bmatrix} \tag{2.3}$$

The tip of the electric field vector traces out an ellipse known as the *polarization ellipse* with a major axis oriented at an angle $\Psi$:

$$\tan 2\Psi = \frac{2E_{0x}E_{0y}\cos(\phi_y - \phi_x)}{E_{0x}^2 - E_{0y}^2} \tag{2.4}$$

The polarization ellipse, however, cannot account for many true states of polarization encountered. Astronomical radio signals are comprised of a superposition of statistically independent polarized states. For partially polarized sources such as pulsars the Stokes parameters $I$, $Q$, $U$, and $V$ are used (Stokes, 1851). $I$ is the total intensity and can be expressed as an incoherent sum of the flux densities of any two orthogonal polarizations. $Q$ and $U$ describe linear polarization where ($Q > 0$) is horizontal, ($Q < 0$) is vertical, ($U > 0$) is oriented +45°and ($U < 0$) is -45°. $V$ describes right ($V > 0$) and left ($V < 0$) circular polarizations (Hamaker and Bregman, 1996). Snik (2009) defines the Stokes vector as:

$$S = \begin{bmatrix} I \\ Q \\ U \\ V \end{bmatrix} = \begin{bmatrix} \langle E_x^* E_x + E_y^* E_y \rangle \\ \langle E_x^* E_x - E_y^* E_y \rangle \\ \langle E_x^* E_y - E_y^* E_x \rangle \\ \langle i(E_y^* E_y - E_y^* E_x) \rangle \end{bmatrix} = \begin{bmatrix} I_{0^o} + I_{90^o} \, , I_{45^o} + I_{-45^o} \, , I_R + I_L \\ I_{0^o} - I_{90^o} \\ I_{45^o} - I_{-45^o} \\ I_R - I_L \end{bmatrix} \tag{2.5}$$

where the first vector is in terms of ensemble averages of the correlations of orthogonal $E$ field components of the Jones vector and the second vector is in terms of flux measurements through polarizers at different angles where $I$ is the intensity regardless of polarization. Eq. 2.5 is consistent with the IAU/IEEE convention outlined in Hamaker and Bregman (1996) which differs in comparison to the PSR/IEEE convention outlined by van Straten et al. (2010) where Stokes $V$ is positive for LCP and negative for RCP. LCP and RCP intensities in terms of Stokes parameters are:

$$I_R = \frac{1}{2}(I + V) \tag{2.6}$$

$$I_L = \frac{1}{2}(I - V) \tag{2.7}$$

Dynamic spectra of LCP and RCP are created by modifying the psrflux program[1] of PSRCHIVE (van Straten et al., 2012) to incorporate eq. 2.6 and eq. 2.7. by subtracting or adding pulse profiles of Stokes $I$ with Stokes $V$ before dividing by 2 and integrating under the on-pulse region for each frequency and for all sub-integrations:

$$S_R(\nu, t) = \sum_{\phi \in \phi_{\text{on}}} \frac{1}{2} \left[ I_{\text{profile}}(\nu, \phi, t) + V_{\text{profile}}(\nu, \phi, t) \right] \tag{2.8}$$

$$S_L(\nu, t) = \sum_{\phi \in \phi_{\text{on}}} \frac{1}{2} \left[ I_{\text{profile}}(\nu, \phi, t) - V_{\text{profile}}(\nu, \phi, t) \right] \tag{2.9}$$

[1]The modified program can be found here: `https://github.com/coderXmachina2/psrflux_birefringence`

### 2.2.5 Scintools

Scintools (SCINtillation TOOLS) is a Python package for the analysis and simulation of pulsar scintillation (Reardon, 2020). Scintools can be used to process dynamic spectra, compute secondary spectra and autocovariances, measure scintillation arcs, simulate dynamic spectra, and model pulsar transverse velocities through scintillation arc curvature or diffractive scintillation bandwidths and timescales.

Scintools works by defining a *Dynspec* class object and several built-in methods. *Dynspec* classes are initialised with dynamic spectra produced from psrflux. Some of the core class methods of Scintools utilised in this work are:

- load_file()

  Loads dynamic spectra and initialises the *Dynspec* object with a psrflux .ds file.

- plot_dyn()

  Plot the dynamic spectrum as a function of frequency and time. If the *lamsteps* argument is given, $S(\nu, t)$ is re-sampled and plotted as $S(\lambda, t)$. The plotted dynamic spectrum is clipped to a maximum of $S_{\text{median}} + 5\sigma$.

- calc_sspec()

  Calculates secondary spectra with the preprocessing steps outlined in Section 2.3.2. If *lamsteps* argument is given, preprocessing will be carried out on $S(\lambda, t)$ producing $P(f_\lambda, f_t)$. *Pre-whitening* and *post-darkening* and windowing *type* and *fraction* can be changed with input arguments.

- plot_sspec()

  Plots the secondary spectrum. If *lamsteps* argument is given, $P(f_\lambda, f_t)$ is plotted. The range of $f_\lambda$ and $f_t$ plotted can be adjusted with input arguments. The plotted secondary spectrum is clipped to a minimum of $P_{\text{median}}$.

- fit_arc()

  Fits for the parabolic arc curvature for the secondary spectrum following the steps outlined in section 2.3.2. The reference frequency is 1284 MHz, and the maximumm delay is 0.22 $\mu$s. Once arc curvature has been fit the secondary spectrum can be replotted with the fit curvature overlaid.

- get_scint_params()

  Calculates diffractive scintllation parameters from the autocovariance function (ACF) of the dynamic spectrum. A one dimensional cut through the center of the ACF is used to find $\Delta\nu_d$ and $\tau_d$. This method also supports an analytical approximation with phase gradient approach following Rickett et al. (2014). The values presented in Table 2.2 are calculated using the one dimensional cut method.

Other important Scintools methods are default_processing() used to remove band edges affected by filter roll-off and zap() for RFI mitigation. We incorporate the bounding box RFI blanking steps discussed in section 2.2.3 into zap(). The norm_sspec() method re-samples the secondary spectrum in $f_t$ by adjusting the sampling of each row with linear interpolation to calculate the "normalized" secondary spectrum, $P(f_\lambda, \frac{f_t}{f_{\text{arc}}})$, where parabola are transformed into vertical lines of power with reference to the primary arc curvature $\eta$ at $\frac{f_t}{f_{\text{arc}}} = \pm 1$. Secondary vertical lines at $\frac{f_t}{f_{\text{arc}}} = \beta$ correspond to a second arc with curvature $\eta_\beta = \frac{\eta}{\beta^2}$. The normalized secondary spectrum is a novel way to search for multiple forward arcs in the secondary spectrum and analyze their power distributions (Reardon et al., 2020). Scintools also has the capability to append dynamic spectra in time and fill any gaps between observations with linear interpolation.

We also added our own methods for computing secondary cross spectra and sampling along the parabola of the secondary spectrum[2].

- calc_sspec_conjugate()

  Calculates the Fourier transform conjugate $\tilde{S}^*(f_\lambda, f_t)$, incorporating the early preprocessing steps. The tilde denotes the two-dimensional Fourier transform.

- calc_cross_sspec()

  Multiplies two secondary spectra to produce secondary cross spectra $C_{RL^*}(f_\lambda, f_t)$ or $C_{LR^*}(f_\lambda, f_t)$. Further elaborated in section 2.3.2. Takes either the real or imaginary part depending on input argument. Completes image preprocessing from the calc_sspec_conjugate() method with a final post-darkening.

- arc_sampling()

  Samples the secondary spectrum values along parabolic arcs for a known input curvature keeping the $f_t$ axis the same.

- calc_norm_cross_corr_coeff()

  Computes the normalization of secondary cross spectra to place upper limits on turbulent magnetic field strengths reported on in the conclusion (section 4.1.3). Takes either the real part or imaginary of the normalized secondary cross spectra depending on input argument.

[2]The modified *Dynspec* class can for this work be found here: `https://github.com/coderXmachina2/MSc_birefringence_Scintools_Dynspec_class/blob/master/x/y/dynspec.py`

### Arc Sampling

To study signal structure along the parabola of the secondary spectrum, data reduction code was written to sample the arc power distribution as a function of Doppler shift. For a known curvature $\eta$, secondary spectra are sampled along the parabola for a range of $-f_t$ to $f_t$ bounded by $f_{\lambda,\,\mathrm{max}}$ calculated from $\tau_{\mathrm{del,\,max}}$ of the arc fitting process in section 2.3.2. The resulting linearised series maps the logarithmic arc power of the parabola to the linear $f_t$ axis of the secondary spectrum. The sampled arc can be thought of as a two sided triangular function where logarithmic power steadily increases as $|f_t| \to 0$. Fig. 2.4 shows an example secondary spectrum $P(f_\lambda, f_t)$ and the corresponding sampled arc $P_{\mathrm{arc}}(f_t)$ from the secondary spectrum. A noteworthy feature of the sampled arc is the dip in power near $f_t = 0$ caused by the pre-whitening and post-darkening process to reduce signal leakage (Coles et al., 2011). This region is smoothed over with a median filter in further analysis.

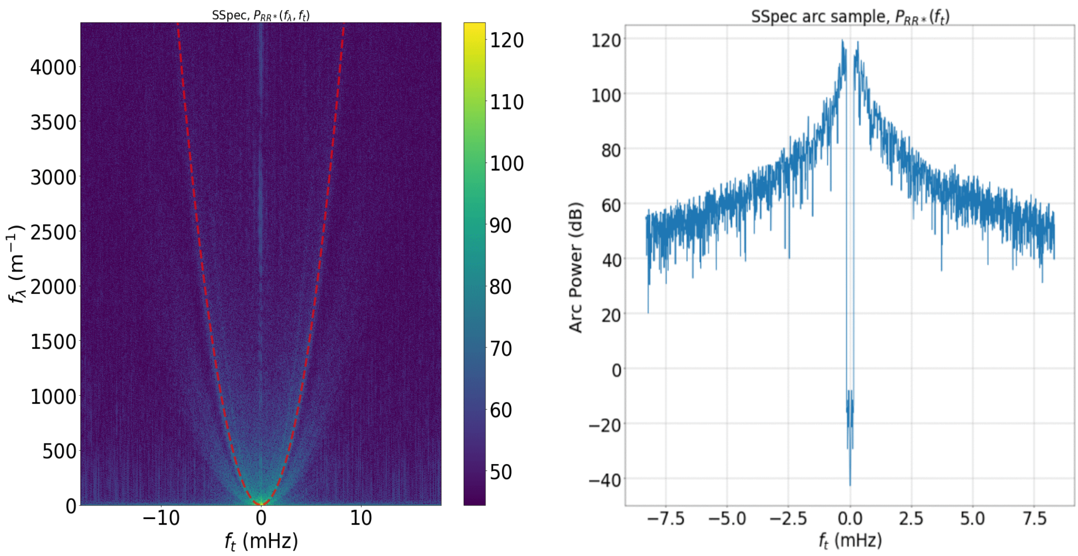


Fig. 2.4: Secondary spectrum $P(f_\lambda, f_t)$ (left) and sampled power along the parabola $P_{\mathrm{arc}}(f_t)$ (right). The red dashed lines of $P(f_\lambda, f_t)$ represent the curvature fit of the parabola from which the values of $P_{\mathrm{arc}}(f_t)$ are taken. No form of interpolation is applied to acquire the sampled signal on the right.

## 2.3 Scintillation Observables

Scintillation produces a spatial interference pattern of intensity variations sampled at the radio telescope receiver from which the effects of IISM turbulence can be observed. The observables from scintillation are dynamic spectra and their secondary spectra.

### 2.3.1 Dynamic Spectra

Dynamic spectra (shortend as *dynspec* where appropriate) are the primary data of pulsar scintillation studies. It is therefore crucial for this work that we have access to the highest possible quality of dynamic spectra. The key parameters to consider are the frequency and time resolutions. Total bandwidth and integration time are also important as long-term fringing can contribute to S/N in the secondary spectrum.

Dynamic spectra are formed by summing over the on-pulse portions of several pulse periods for each channel output by a spectrometer (Cordes et al., 2006). The pulse profile values to be summed are contained within the folded pulsar archives of PSRCHIVE sub-integrations (van Straten et al., 2012). Each sub-integration is a data cube of frequency, phase, and polarization. To create dynamic spectra of variable length, sub-integrations are appended. For our initial approach with raw uncalibrated data, dynamic spectra are formed in lengths of $t$ = 1 hour comprising of 450 sub-integrations.

Time resolution is obtained at $\Delta t$ = 8 seconds per sub-integration. Frequency resolution is the total bandwidth ($\nu_{\rm BW}$) divided by the total number of channels ($N_{\rm ch}$) where $\nu_{\rm BW}$ = 856 MHz and $N_{\rm ch}$ = 4096. Frequency resolution is therefore 208.98 kHz per channel. A dynamic spectrum of $t$ = 1 hour is therefore represented by a 4096 × 450 pixel map of intensities as a function of frequency versus time with the smallest division of frequency 208.98 kHz wide and the smallest division of time 8 seconds wide. A sample of dynamic spectra of total intensity, $S_I(\nu, t)$, plotted with native PSRCHIVE pgplot tools is shown in Fig. 2.5.

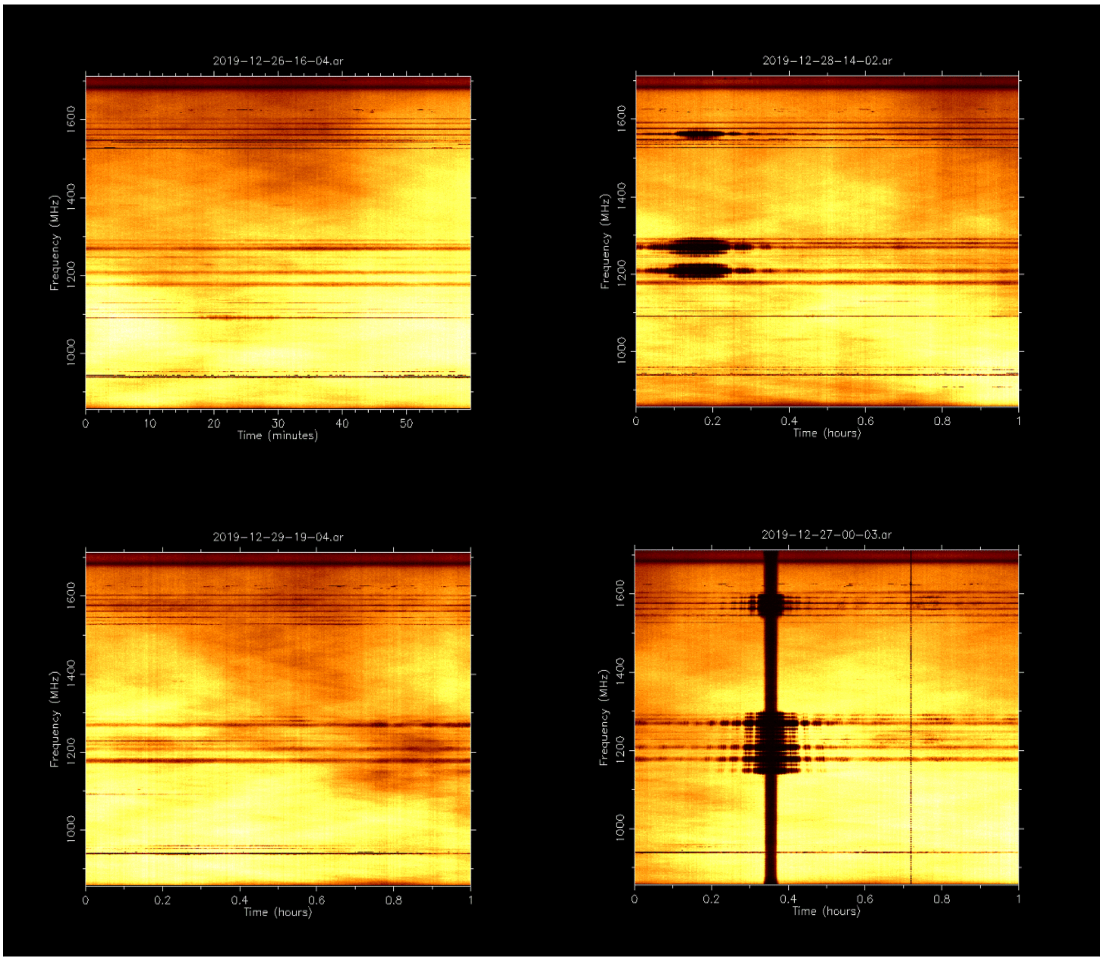


Fig. 2.5: Sample of dynamic spectra plotted by PSRCHIVE (Hotan et al., 2004). The black pixels are data that have been corrupted by RFI and/or receiver instrumentation problems.

From Fig. 2.5, scintillation phenomena and drifting criss-cross fringing that enable the parabolic arc phenomenon in the secondary spectrum can be observed. The frequency dependence of scattering is verified with scintles appearing much wider at lower frequency. RFI are also present in the dynamic spectra. Between the regions corrupted by RFI are the relatively pristine sub-bands of $1300 < \nu < 1520$ MHz, $950 < \nu < 1160$ MHz, and $\nu < 940$ MHz where we expect to acquire the most useful spectral content. A more comprehensive characterization of the L-band radio frequency spectrum of MeerKAT studied in this work is provided in Bailes et al. (2020).

### Regime of Scintillation

J0437-4715 is a well studied MSP in many measures beyond its timing and astrometry (van Straten et al., 2001; Reardon et al., 2020). Due to its timing stability, J0437-4715 is a high priority target for both Parkes and International PTA projects (Hobbs et al., 2010). Studies have also been done to measure its scintillation parameters and regime of scattering (Smirnova et al., 2006). From the uncertainty relation eq. 1.27, the pulsar has a wide $\Delta\nu_d$ and short $\tau_s$. For a low dispersion measure (DM = 2.64 pc cm$^{-3}$), the short $\tau_s$ is expected. The MSP is noted for having a broad and narrow scale of scintillation (Gwinn et al., 2006). It is often observed in the regime of weak scattering where $\Delta\nu_d > \nu_{\text{obs}}$ for $\nu_{\text{obs}}$ above a transition frequency of 1 GHz. For $\nu_{\text{obs}}$ < 1 GHz and $\Delta\nu_d < \nu_{\text{obs}}$ the pulsar is observed in the regime of strong scattering typical of most pulsars (Reardon, 2018). We can attempt to verify these properties by taking the ACF of the dynamic spectra using Scintools to calculate $\Delta\nu_d$ and $\tau_d$ from which we can calculate scattering strength, ($u = \sqrt{\frac{\nu_{obs}}{\Delta\nu_d}}$). The results are presented in Table 2.2. $\Delta\nu_d$ and $\tau_d$ are calculated from $S_R(\nu, t)$ and $S_L(\nu, t)$ and averaged.

| Obs. date | $t$ (hours) | $\Delta\nu_d$ (MHz) | $\tau_d$ (s) | $u$ |
|---|---|---|---|---|
| 2019-12-26 | 11 | 97.31 ± 1 | 862.33 ± 7 | 3.63 |
| 2019-12-27 | 11 | 107.73 ± 1 | 1047.14 ± 13 | 3.45 |
| 2019-12-28 14:00:00 | 4 | 97.34 ± 1 | 964.11 ± 15 | 3.63 |
| 2019-12-28 22:00:00 | 4 | 119.26 ± 1 | 919.67 ± 13 | 3.28 |
| 2019-12-29 | 11 | 121 ± 1 | 2067.31 ± 23 | 3.24 |
| 2019-12-30 | 11 | 105 ± 1 | 1200.52 ± 16 | 3.49 |
| 2019-12-31 | 11 | 84 ± 1 | 852.50 ± 9 | 3.90 |

Table 2.2: Scintillation parameters of the MSP J0437-4715 for all observed epochs. The scattering parameter puts the pulsar in the regime of strong scattering even though $\nu_{\text{obs}}$ is greater than 1 GHz. This runs contrary to what was previously mentioned, however, Reardon (2018) also states that stable measurement of$\Delta\nu_d$ and $\tau_d$ for J0437-4715 is difficult due to an insufficient number of scintles and changing scattering strengths. Our interpretation is that scintillation from a mix of strong and weak scattering is captured. It is noted that even during scintillation minima that the *dynspecs* do not approach intensities of 0 meaning there is weak scintillation occurring within the spectra

### 2.3.2 Secondary Spectra

Pulsar secondary spectra (shortened as *SSpec* where appropriate) are formed by taking the two-dimensional Fourier transform of dynamic spectra to reveal parabolic arcs as a function of conjugate frequency ($f_\nu$) and conjugate time ($f_t$). Power distributions of secondary spectra are typically studied on a logarithmic scale to improve visual dynamic range (Stinebring et al., 2001; Hill et al., 2003).

The Nyquist sampling frequencies that describe the highest conjugate frequencies that can be encoded at a given sampling rate without aliasing can be calculated as; $f_\nu$(Nyquist) = $\frac{N_{\mathrm{ch}}}{2\nu_{\mathrm{BW}}}$ = 2.39 $\mu$s and $f_t$(Nyquist) = $\frac{1}{2\Delta t}$ = 62 mHz (Cordes et al., 2006). These values set the outer most bounds of the $f_\nu$ and $f_t$ axes of the secondary spectrum. The resolutions of the $f_\nu$ and $f_t$ axes are $\Delta f_\nu = \frac{1}{\nu_{\mathrm{BW}}}$ and $\Delta f_t = \frac{1}{t_{\mathrm{obs}}}$. Table 2.3 shows the smallest divisions of $f_\nu$ and $f_t$ for varying lengths of $\nu_{\mathrm{BW}}$ and $t_{\mathrm{obs}}$.

| $n_{\mathrm{subint}}$ | $t_{\mathrm{obs}}$ (hrs) | $\nu_{\mathrm{BW}}$ (MHz) | $\Delta f_\nu$ ($\mu$s) | $\Delta f_t$(mHz) | Fig. 2.6 |
|---|---|---|---|---|---|
| 450 | 1 | 856 | 0.001 | 0.28 | (a) |
| 4950 | 11 | 244 | 0.004 | 0.02 | (b) |
| 450 | 1 | 244 | 0.004 | 0.28 | (c) |
| 4950 | 11 | 856 | 0.001 | 0.02 | (d) |

Table 2.3: Resolutions of secondary spectrum $f_\nu$ and $f_t$ axes. Lengths of one hour are considered as the smallest division of $S(\nu, t)$ as per our initial approach and lengths of 11 hours represent the longest continuous $S(\nu, t)$ recorded within a day of observation. A low frequency portion $\nu_{\mathrm{BW}} = \frac{1}{4}(856)$ MHz was considered because of the frequency dependence of scattering that may produce different results with further processing. Longer $t_{\mathrm{obs}}$ across the full $\nu_{\mathrm{BW}}$ yield the finest $f_\nu$ and $f_t$ resolutions. A sample of secondary spectra for each configuration are presented in Fig. 2.6.

Several preprocessing steps are performed to create secondary spectra. The preprocessing steps are built upon prior scintillation studies and digital signal processing practices to reduce signal leakage and maximize S/N. Further description of the preprocessing steps are found in section 2.1 of Reardon et al. (2020). The preprocessing steps are taken in the order as follows:

1. **Default preprocessing.** Remove band edges affected by bandpass filter roll-off to improve dynamic range. Refill NaNs and zeroes with linear interpolation. Gain variations in frequency are corrected using a bandpass filter and variations in time are corrected using a Savitsky-Golay filter.

2. **$\lambda$-step sampling.** Re-sample and resize dynamic spectra uniformly in $\lambda$-steps using cubic interpolation onto a grid with $\lambda$-step size equal to the difference in the lowest two frequency channels to sharpen arc features. Sampling in $\lambda$-steps removes the frequency dependence of arc curvature (Fallows et al., 2014).

3. **Windowing.** Apply a hamming window on outer 10 % of each dynamic spectrum to reduce sidelobe response. Unwanted signals in these bins contribute to power along the vertical and horizontal axes of the secondary spectrum.

4. **Normalization.** Subtract the mean flux from each pixel of $S(\lambda, t)$ to center the image. This sets the mean of the dynamic spectrum to zero.

5. **Pre-whitening.** Pre-whiten using first-difference method in the time domain to minimize spectral leakage. Bright scintles leak as low frequency power in the secondary spectrum (Kerr et al., 2018). For an input *dynspec* $x(k)$, the pre-whitening filter is expressed as $y(k) = x(k) - x(k-1)$ for an output $y(k)$ where $k$ is $\lambda$ and $t$. This step is executed by convolving $S(\lambda, t)$ with the array $\left(\begin{smallmatrix} 1 & -1 \\ -1 & 1 \end{smallmatrix}\right)$ resulting in multiplication; $\tilde{x}(f)H(f)$ in the frequency domain. The tilde denotes the Fourier transform, $H(f) = 2\sin(\pi f \delta)$, and $\delta$ is the sample interval. Pre-whitening multiplies the secondary power spectrum with $|H(f)|^2 = (2\sin(f\delta))^2$ where $f$ corresponds to both $f_\lambda$ and $f_t$. (Coles et al., 2011).

6. **Fourier transform.** Apply the two-dimensional fast Fourier transform (FFT). The FFT output is resized as $2^{(\lceil \log_2(\lambda_{\rm rows})\rceil+1)}$ for $f_\lambda$ and $2^{(\lceil \log_2(t_{\rm cols})\rceil+1)}$ for $f_t$ axes. For $\nu_{\rm BW}$ = 856 MHz and $t_{\rm obs}$ = 11 hours, a $\lambda$-step sampled *dynspec* of 2049 $\lambda_{\rm rows}$ × 5104 $t_{\rm cols}$ will produce an *SSpec* of 8192 $f_{\lambda \rm rows}$× 16384 $f_{t\rm cols}$.

7. **Square law detection.** Take the real part of the multiplication of the secondary spectrum with its conjugate $P(f_\lambda, f_t) = \text{Re}(\tilde{S}_I \tilde{S}_I^*)$.

8. **FFT Shift.** Shift the zero frequency component to the center of the spectrum. This step forms a mirrored parabola with positive and negative $f_\lambda$.

9. **Crop spectrum.** The conjugate spectrum is Hermitian (point symmetric). For any real valued $S(\lambda, t)$, the Fourier transform $\tilde{S}(f_\lambda, f_t) = \tilde{S}^*(-f_\lambda, -f_t)$. We can discard the bottom plane without losing any information. The dimensions of the *SSpec* from step 6 will become 4096 $f_{\lambda,\rm rows}$× 16384 $f_{t,\rm cols}$.

10. **Postdarkening.** The reverse process of pre-whitening. The power spectrum is divided by $|H(f)|^2$ (Coles et al., 2011; Kerr et al., 2018).

11. **Log Scale.** Take 10 times the logarithm of the secondary spectrum to improve visual dynamic range, useful if the power spectrum is log-normally distributed.

The general form of the secondary spectrum is expressed as:

$$P_{II^*}(f_\lambda, f_t) = 10 \log_{10}(|\tilde{S}_I(f_\lambda, f_t)|^2) \tag{2.10}$$

where $S$ is the mean subtracted and windowed dynamic spectrum and the tilde is the two-dimensional FFT. *I* refers to a secondary spectrum of total intensity. This subscript notation can be extended for circular polarization where $P_{LL^*}(f_\lambda, f_t)$ and $P_{RR^*}(f_\lambda, f_t)$ are secondary spectra formed from $S_L(\nu, t)$ and $S_R(\nu, t)$. Fig. 2.6 shows a sample of $P_{RR^*}(f_\lambda, f_t)$ produced by the preprocessing steps on calibrated MeerKAT data.

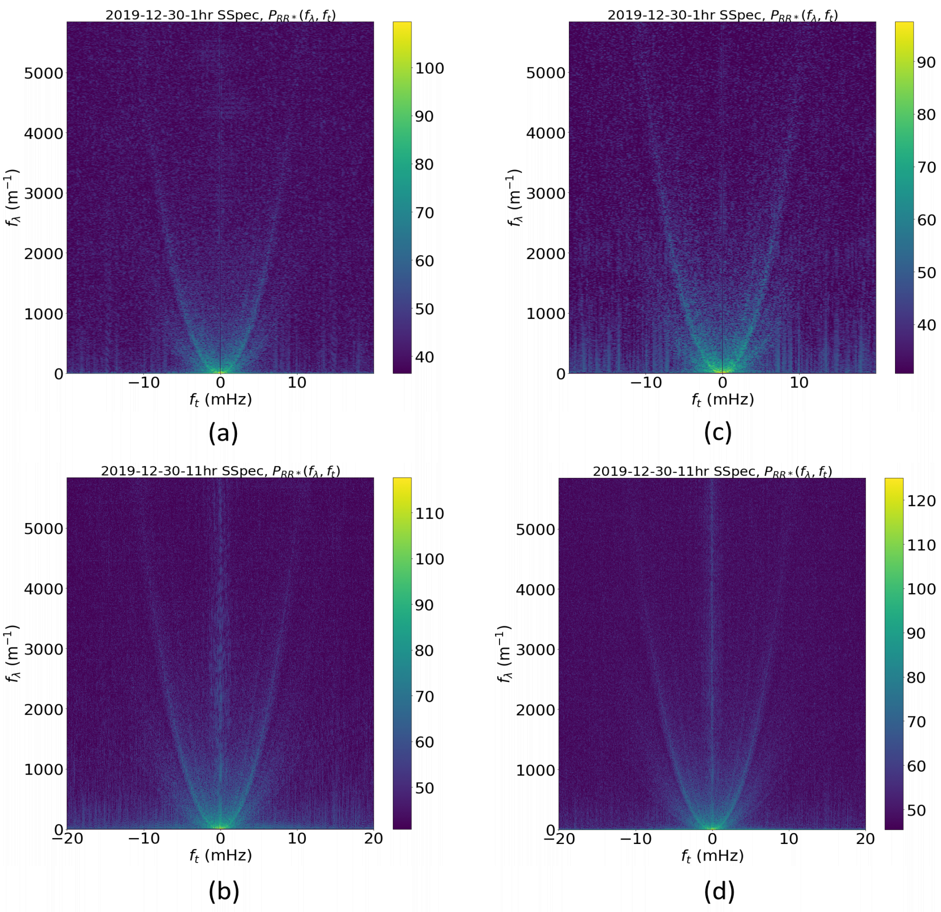


Fig. 2.6: Sample of secondary spectra generated from *dynspec* of varying $\nu$ and $t$. *SSpec* (b) and (c) are for $\nu$ = 232 MHz. *SSpec* (a) and (d) are for $\nu$ = 856 MHz. *SSpec* (a) and (c) are for $t$ = 1 hour and *SSpec* (b) and (d) are for $t$ = 11 hour. The vertical lines are a result of RFI that are constant with time, but vary with frequency in the *dynspec*.

The main feature from Fig. 2.6 is an upwards parabola known as a *forward arc*. The primary forward arcs in the case of our J0437-4715 data correspond mostly to scattering mapped onto spatial frequencies of the range 0 < $f_\lambda$ < 5000 m$^{-1}$ ($\tau \approx$ 1.68 $\mu$s) and the domain -10 < $f_t$ < 10 mHz. When sampled in $\lambda$-steps, power decays rapidly off the thin parabola. Within the primary arc is a secondary arc of higher curvature while outside the primary arc is a diffuse band of power where other forward arcs may exist. An unexpected feature is a diffuse arc of extremely low curvature at $f_\lambda$ < 500 m$^{-1}$ obscured by RFI. The low curvature arc is thought to originate from scattering by the bow-shock of J0437-4715 at $D_s \approx$ 9000 AU (Fruchter, 1995; Rangelov et al., 2016).

### Arc Curvature Fit

Arc curvature, $\eta$, can be fit using Scintools and is modelled on the steps taken by Bhat et al. (2016) in their analysis of scintillation arcs from low frequency Murchison Widefield Array (MWA) and Parkes observations of J0437-4715. For a set of trial curvatures $\{\eta_i\}$, power along the parabola is parametrized as a function of curvature. Summing along linearly-interpolated pixels neighboring $f_{t,i} = \pm\sqrt{\frac{f_\lambda}{\eta_i}}$ for each $f_\lambda$ in $P(f_\lambda, f_t)$ and dividing by twice the number of rows ($N$) in $P(f_\lambda, f_t)$, the mean power of the arc as a function of curvature can be computed:

$$P_{\text{arc}}(\eta) = \frac{1}{2N}\sum_{i=1}^{N} P(\eta f_{t,i}^2, f_{t,i}) \tag{2.11}$$

The sum performed along the parabola is cropped at a certain maximum delay $\tau_{\text{del, max}}$ so as to not incorporate delays beyond which little power is detectable and to prevent the mean power from being averaged down by noise. From Reardon (2018) $\tau_{\text{del, max}}$ can be calculated as:

$$\tau_{\text{del, max}} = 0.22(\frac{1284\text{ MHz}}{f})^2 \mu s \tag{2.12}$$

where the L-band center frequency of 1284 MHz is used as reference. Since we often work in $\lambda$-steps; $f_{\lambda,\text{ max}} = 538.35(\frac{23\,\text{cm}}{c/\lambda})$ m$^{-1}$. Summing is avoided at low-frequency regions near the origin to minimize errors from the bright core. The curvature is found via a three-point smoothing window on $P_{\text{arc}}(\eta)$ and finding the maximum. Fig. 2.7 shows an example of the arc curvature fitting process where the vertical axis is the mean arc power and the horizontal axis is trial curvature. A detailed description of the fitting procedure and derivation of the measurement uncertainty can be found in section 4.3.1 of Reardon (2018). Curvature uncertainties vary between 0.7 and 1.5 m$^{-1}$ mHz$^{-2}$. Longer time integrations and better RFI mitigation can reduce the uncertainties.

From Fig. 2.7 we can see that different trial curvatures correspond to different mean power. The curvature of the primary forward arc is found from the largest peak of $P_{\mathrm{arc}}(\eta)$. Any secondary or tertiary forward arcs can are fit from adjacent peaks of power. At least two forward arcs are expected for J0437-4715 (Reardon et al., 2020). The scattering screen distances are $D_{\eta 1}$ = 124 ± 3 pc and $D_{\eta 2}$ = 89.8 ± 0.4 pc from Earth to the pulsar with $D_{\eta 1}$ coinciding with the outer boundary of the ellipsoidal shell of the local bubble and the $D_{\eta 2}$ coinciding with the inner boundary as per the 3 component model of the local ISM proposed by Bhat et al. (1998). In some studies, up to 8 forward arcs can be detected towards J0437-4715 (D. Reardon, private communication). This study focuses on analyzing the power distributions from the arc of the scattering screen at $D_{\eta 1}$ because of its higher S/N. The arc from the screen at $D_{\eta 2}$ is visible but faint in our 23 cm MeerKAT observations. A list of all curvature fits for calibrated and uncalibrated data for different integration lengths is included in Appendix B. All arc curvatures are in units of m$^{-1}$ mHz$^{-2}$ and the maximum uncertainty is 1.5.

Utilizing the arc curvature fitting technique and fitting for $\eta$ of secondary spectra from dynamic spectra of $t$ = 1 hour for all hours of observation and plotting $\eta$ throughout the entire six days of which the pulsar is observed yields the periodic sinusoidal pattern of curvature variation seen in Fig. 2.8. The oscillation of curvature coincides with modulation by the orbital period of J0437-4715 ($P_b$ = 5.75 days). This is due to the dependence of $\eta$ on the changing velocity of the pulsar projected onto the plane of the scattering screen. Long term monitoring of scintillation arcs to measure the velocity components of pulsars may be superior to the traditional method of observing variations of the diffractive scintillation timescale as scintillation arc curvatures are independent of the strength of turbulence within the IISM (Reardon et al., 2020).

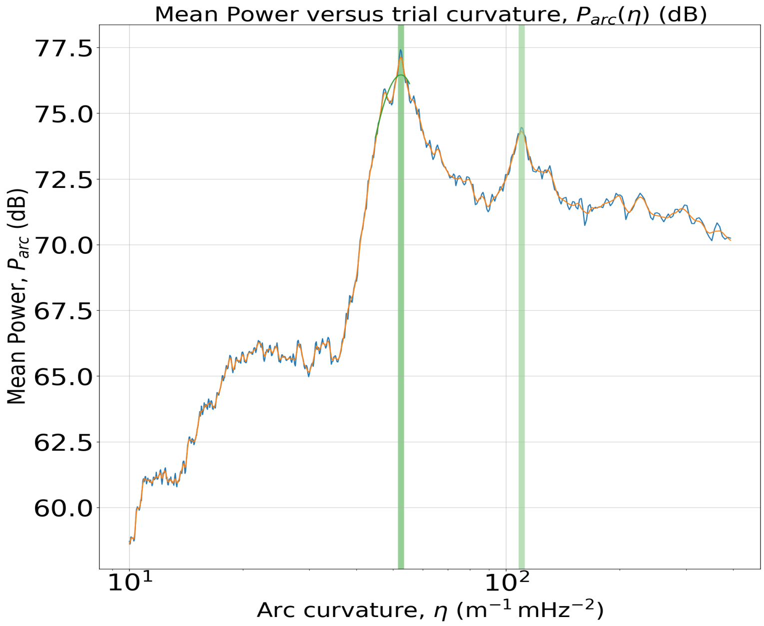


Fig. 2.7: Mean power as a function of trial curvatures. The tallest peak corresponds to the primary forward arc, $\eta_1$ = 63.89 (green vertical left). Other forward arcs appear as adjacent spikes of power, $\eta_2$ = 110.47 (green vertical right). The sample fit is from an *SSpec* derived from the $\nu$ = 856 MHz and $t$ = 11 hour calibrated *dynspec* of 2019-12-27.

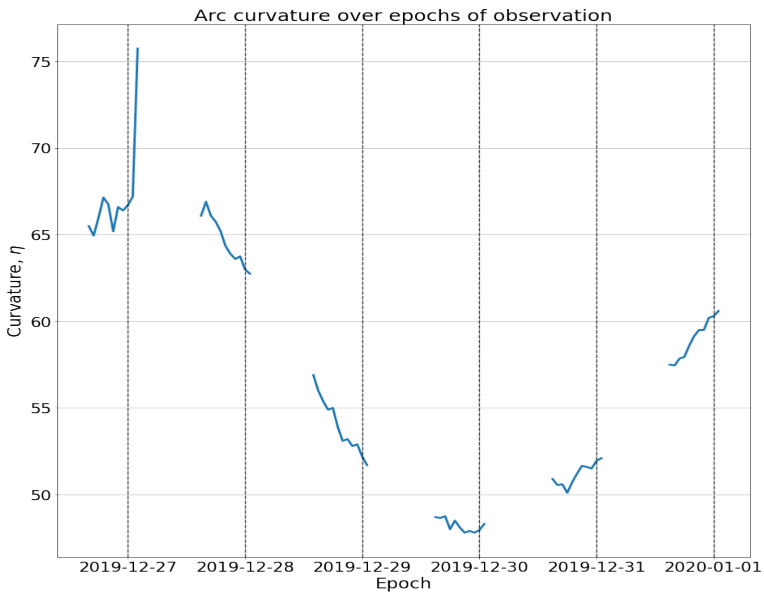


Fig. 2.8: Variations of arc curvature for all observed epochs. The vertical dashed lines represent UTC = 00:00:00. The spike on 2019-12-27 is due to RFI. Arc curvature was measured from raw data and the average of $\eta_L$ and $\eta_R$ were taken. The gaps represent durations where the pulsar was not observed. A full orbital period is nearly resolved.

## 2.4 Analysis

This section looks at the analysis steps applied on the scintillation observables to look for evidence of the effect of birefringence.

### 2.4.1 Differential Spectra

#### Dynamic Spectra

A preliminary test for birefringent scintillation can be performed by subtracting RCP and LCP dynamic spectra to see if sufficient differences between $\phi_R$ and $\phi_L$ ($\Delta\phi_{RL}$) produces a pattern of scintillation in the differential dynamic spectra, $S_{\text{diff}}(\nu, t)$:

$$S_{\text{diff}}(\nu, t) = S_R(\nu, t) - S_L(\nu, t) \tag{2.13}$$

where the difference is taken between each point of intensity. This was previously attempted by Brisken et al. (2010) towards PSR B0834+06 where no detectable signal significant at the 0.1 $\%$ level was found with dynamic spectra of frequency and time resolutions of $\Delta\nu$ = 244 Hz and $\Delta t$ = 6.25 s over bandwidths and integration lengths of $\nu_{\text{BW}}$ = 8 MHz, and $t_{\text{obs}}$ = 6500 seconds. The resolutions in the Fourier domain were $\Delta\tau$ = 0.125 $\mu$s and $\Delta f_t$ = 0.15 mHz observable to a maximum of $\tau$ = 2.05 ms and $f_t \pm$ 80 mHz. The observations were made with low frequency VLBI ($\nu$ = 327 MHz). These results underline the small value nature of $\Delta\phi_{RL}$.

Differential Faraday rotation from turbulent interstellar magnetic fields (Macquart and Melrose, 2000b) would result in a subtle displacement of of RCP and LCP spectra. Supposing that the displacement is significant and $\Delta\phi_{RL}$ is large, $S_R(\nu, t)$ and $S_L(\nu, t)$ could be qualitatively different with bright scintles in one spectra corresponding to a dimmer scintle in the other. However, we will most likely observe $S_R(\nu, t)$ and $S_L(\nu, t)$ as qualitatively similar with any quantifiable significance requiring statistical tests.

We can state a null and an alternate hypothesis as a result of $\Delta\phi_{RL}$:

$H_0 : S_R(\nu, t)$ and $S_L(\nu, t)$ are statistically identical (highly correlated).

$H_1 : S_R(\nu, t)$ and $S_L(\nu, t)$ are different.

For display purposes in Chapter 3, a $3\sigma$ filter is applied to $S_{\text{diff}}(\nu, t)$. However, no filter is applied to compute the secondary spectrum of $S_{\text{diff}}(\nu, t)$ in order to better preserve the signal. We can quantify a significance between LCP and RCP with:

$$\% = 2\frac{S_R(\nu, t) - S_L(\nu, t)}{S_R(\nu, t) + S_L(\nu, t)} \tag{2.14}$$

where values closer to 0 represents more similarity and a values farther from 0 implies a greater difference. Eq. 2.14 is taken for each pixel and not averaged for $S_{\text{diff}}(\nu, t)$.

**Secondary Spectra**

The secondary spectrum can be used to look for evidence of birefringence. Separate secondary spectra of RCP and LCP are first created and observed. If the effects of $\Delta\phi_{RL}$ are strong, the two parabola may appear to have different power distributions. Curvature is expected to remain unchanged between for $P_{LL^*}$ and $P_{RR^*}$ of the same epoch. However, as per their dynamic spectra, $P_{LL^*}$ and $P_{RR^*}$ are likely to appear very similar and the only differences are detectable quantitatively. Two approaches come to mind when trying to investigate the effect of $\Delta\phi_{RL}$ in the secondary spectrum:

$$P_{\text{diff}}(f_\lambda, f_t) = 10\log(|\tilde{S}_{RR^*}(f_\lambda, f_t)|^2) - 10\log(|\tilde{S}_{LL^*}(f_\lambda, f_t)|^2) \tag{2.15}$$

$$P_{S_{\text{diff}}}(f_\lambda, f_t) = 10\log(|\tilde{S}_{\text{diff}}(f_\lambda, f_t)|^2) \tag{2.16}$$

where $P_{\text{diff}}$ is the difference between each pixel of two detected spectra and $P_{S_{\text{diff}}}$ is the squared magnitude of the FFT of $S_{\text{diff}}(\nu, t)$. Eq. 2.15 is akin to a ratio of detected powers as $P_{\text{diff}}(f_\lambda, f_t) = 10\log(\frac{|\tilde{S}_{RR^*}(f_\lambda,f_t)|^2}{|\tilde{S}_{LL^*}(f_\lambda,f_t)|^2})$. Since two signals of different phase can have the same power $P_{\text{diff}}(f_\lambda, f_t)$ tells us nothing about $\Delta\phi_{RL}$. In eq. 2.16 the detected power is from Re$((\widetilde{S_R - S_L})(\widetilde{S_R - S_L})^*) = L^2 - R^2 - 2\text{Re}(RL^*)$. If the powers of L and R are similar then the first two terms cancel out making the detected power the real part of a cross correlation between R and L i.e. -2Re$(RL^*)$. However, if $\Delta\phi_{RL}$ is small, $\cos(\Delta\phi_{RL}) = 1 - \frac{(\Delta\phi_{RL})^2}{2}$ upon detection of $RL^*$ making the effect of $\Delta\phi_{RL}$ more difficult to detect. We require an approach that works under the condition of small values of $\Delta\phi_{RL}$. The secondary cross spectra is one such approach.

### 2.4.2 Secondary Cross Spectra

Secondary cross spectrum are complex-valued functions produced by cross correlating the secondary spectrum of one circular polarization with the secondary spectrum of the orthogonal sense of circular polarization. An example can be defined as:

$$C_{RL^*}(f_\lambda, f_t) = \tilde{S}_R(f_\lambda, f_t)\tilde{S}_L^*(f_\lambda, f_t) \tag{2.17}$$

where $\tilde{S}_R$ is the FFT of an RCP dynamic spectrum and $\tilde{S}_L^*$ is the conjugate of the FFT of an LCP dynamic spectrum. The result is a complex-valued spectrum which encodes an amplitude in the real part and a phase in the imaginary part when $\phi \ll 1$. We can use this attribute of the secondary cross spectrum to study variations of $\Delta\phi_{RL}$. All of the secondary spectrum preprocessing steps discussed in section 2.3.2 are used to compute $C_{RL^*}(f_\lambda, f_t)$. After much experimentation, the best results were arrived at using the process outlined in Fig. 2.9. The final result of the secondary cross spectrum is either $P_{\text{Re}(RL^*)}(f_\lambda, f_t)$ for the amplitude or $P_{\text{Im}(RL^*)}(f_\lambda, f_t)$ for the weighted phase spectrum upon taking the complex argument, absolute value, and normalization to the log scale:

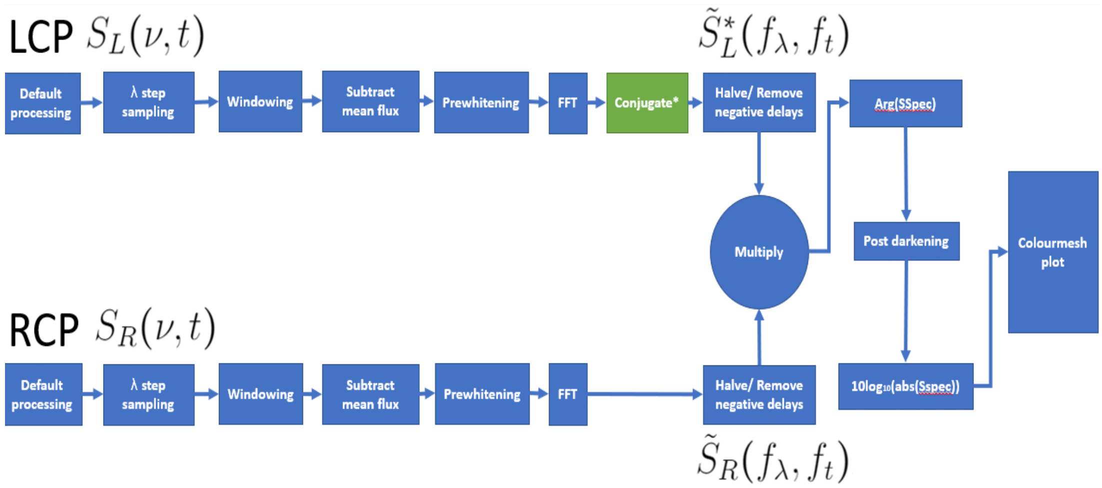


Fig. 2.9: Process of computation of secondary cross spectrum between LCP and RCP. The example displayed is for $C_{RL^*}(f_\lambda, f_t)$. Likewise, $C_{LR^*}(f_\lambda, f_t)$ can also be computed by multiplying $\tilde{S}^*_R(f_\lambda, f_t)$ with $\tilde{S}_L(f_\lambda, f_t)$.

$$P_{RL^*}(f_\lambda, f_t) = 10\log\left(|\arg(\tilde{S}_R(f_\lambda, f_t)\tilde{S}^*_L(f_\lambda, f_t))|\right) \tag{2.18}$$

**Cross Spectra Analysis**

The phase from the imaginary part of the secondary cross spectrum is a principle part of our analysis as the most stringent method of observing the effects of birefringent scintillation. From Simonetti et al. (1984), variance of $\Delta\phi_{RL}$ (also referred to as $\Delta\phi_{\delta\beta}$) as a result of decorrelation of RCP and LCP spectra is measurable through the exponential decay of the cross-covariance coefficient $\Gamma_{RL}$:

$$\Gamma_{RL} = \exp(-\langle\Delta\phi^2_{\delta\beta}\rangle) \tag{2.19}$$

where greater variance of $\Delta\phi_{\delta\beta}$ implies greater decorrelation between RCP and LCP spectra. This effect can also be understood as the second moment phasor sum:

$$\langle u_R u^*_L\rangle = \langle a_L a_R \exp\left[i(\Delta\phi_{\delta\beta})\right]\rangle \tag{2.20}$$

where $a_L$ and $a_R$ are amplitudes and $\Delta\phi_{\delta\beta} = \Delta\phi_{RL} = \phi_R - \phi_L$. The phase component of the cross correlated $C_{RL^*}$ can be used to examine the variations of $\Delta\phi_{\delta\beta}$ as a function of $f_\lambda$ and $f_t$ along the parabola. If $\Delta\phi_{\delta\beta}$ is small and $\sin(\Delta\phi_{\delta\beta}) \approx \Delta\phi_{\delta\beta}$ from the phasor sum, the imaginary part of $C_{RL^*}$ as a direct linear relation to $\Delta\phi_{\delta\beta}$ is more sensitive to small phase variations than the $S_{\text{diff}}(\nu, t)$ and $P_{S_{\text{diff}}}(f_\lambda, f_t)$.

The arc sampling method presented in section 2.2.5 is employed. $\Delta\phi_{\delta\beta}$ is expected to vary continuously, smoothly, and significantly along the parabola. As seen in Fig. 1.10 from Brisken et al. (2010) the phase of the secondary cross spectrum is a parabola with a mean of zero and a distribution of roughly equal positive and negative values. If $\Delta\phi_{\delta\beta}$ is positive valued in $RL^*$, it is negative valued in $LR^*$ and vice versa. Since negative values are undefined upon taking their logarithm, we study the structural variations of $\Delta\phi_{\delta\beta}$ along the parabola separately from both $P_{\text{Im}(LR^*)}(f_\lambda, f_t)$ and $P_{\text{Im}(RL^*)}(f_\lambda, f_t)$ without taking the absolute value. Structure from birefringent scintillation is marked by how these values are organised in the distribution of either their signal run lengths and/or their relative power along the parabola. We record for purposes of analysis the longest sampled continuous signal runs along the parabola, the average power of the sampled signal run, and their locations on the $f_t$ axis after taking the logarithm for the spectrum.

### 2.4.3 Implementation

In summary, the design of our research is as follows.

1. Acquire MeerKAT data.

2. Create LCP and RCP dynamic spectra with psrflux.

3. Maximise the quality of dynamic spectra with RFI mitigation and calibration.

4. Use Scintools to perform each of the analysis techniques detailed in section 2.4 on all of the RFI mitigated and calibrated MeerKAT data.

5. Interpret the results from the analysis techniques.

# Chapter 3

# Results

This chapter presents the results of our analysis techniques to support our study of birefringent scintillation towards the millisecond pulsar J0437-4715. Section 3.1 examines differential spectra, where section 3.1.1 presents $S_L(\nu, t)$, $S_R(\nu, t)$, and $S_{\text{diff}}(\nu, t)$ dynamic spectra. Section 3.1.2 presents $P_{LL^*}(f_\lambda, f_t)$, $P_{RR^*}(f_\lambda, f_t)$, $P_{S_{\text{diff}}}(f_\lambda, f_t)$ secondary spectra, and $P_{\text{arc}}(f_t)$ of $P_{S_{\text{diff}}}(f_\lambda, f_t)$ at the curvature of where we most likely expect a signal to appear. Section 3.2 presents the real and imaginary parts of the power spectrum of $C_{RL^*}(f_\lambda, f_t)$ as well as a sampling along the primary forward arc of $P_{\text{Im}(RL^*)}(f_\lambda, f_t)$ and $P_{\text{Im}(LR^*)}(f_\lambda, f_t)$. Also included is a tabulation of the longest signal runs sampled along the arcs of $P_{\text{Im}(RL^*)}(f_\lambda, f_t)$ and $P_{\text{Im}(LR^*)}(f_\lambda, f_t)$ where phase varies continuously enough along the arc to be considered as possible variations of $\Delta\phi_{LR}$ as a result of birefringence. Observations of 2019-12-26 and 2019-12-27 include the cross spectrum phase. We also compute an average power by summing along the signal run and dividing by the length of the sampled signal run. We compute the width of the signal run in units of $f_t$ mHz along the arc. We then classify the signal runs using the midpoint between the first and last sampled $f_t$ into different regions of the arc where $|f_t| > 7$ is within the stochastic noise field, $5 < |f_t| < 7$ is the outer arc, and $-5 < |f_t| < 5$ is the inner arc. The sampled signals can be further statistically analyzed for structure.

# 3.1 Differential Spectra

## 3.1.1 Dynamic Spectra

### 2019-12-26

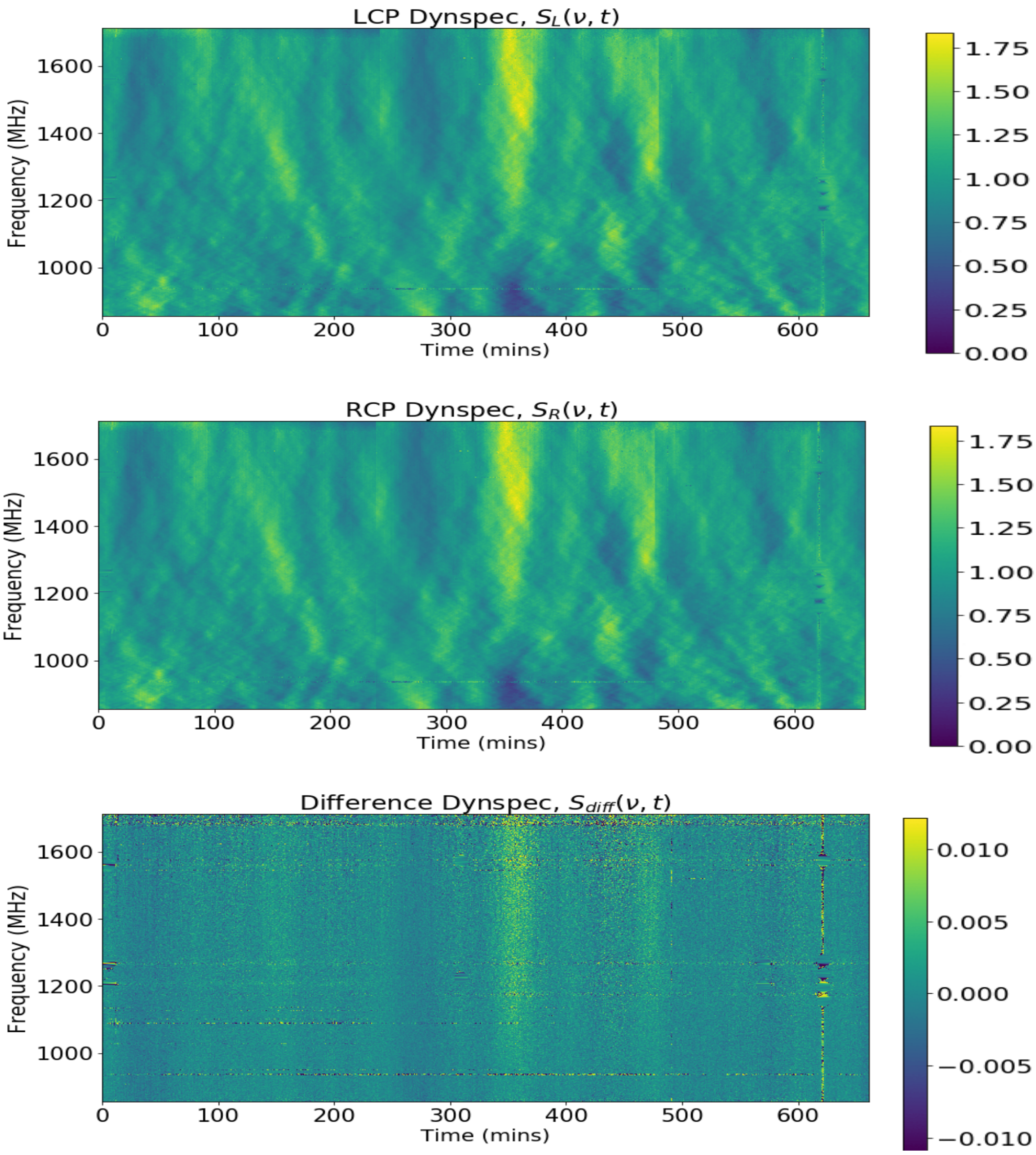


Fig. 3.1: Dynamic spectra of LCP $(S_L(\nu, t))$, RCP $(S_R(\nu, t))$, and their difference spectrum $(S_{\text{diff}}(\nu, t))$

**2019-12-27**

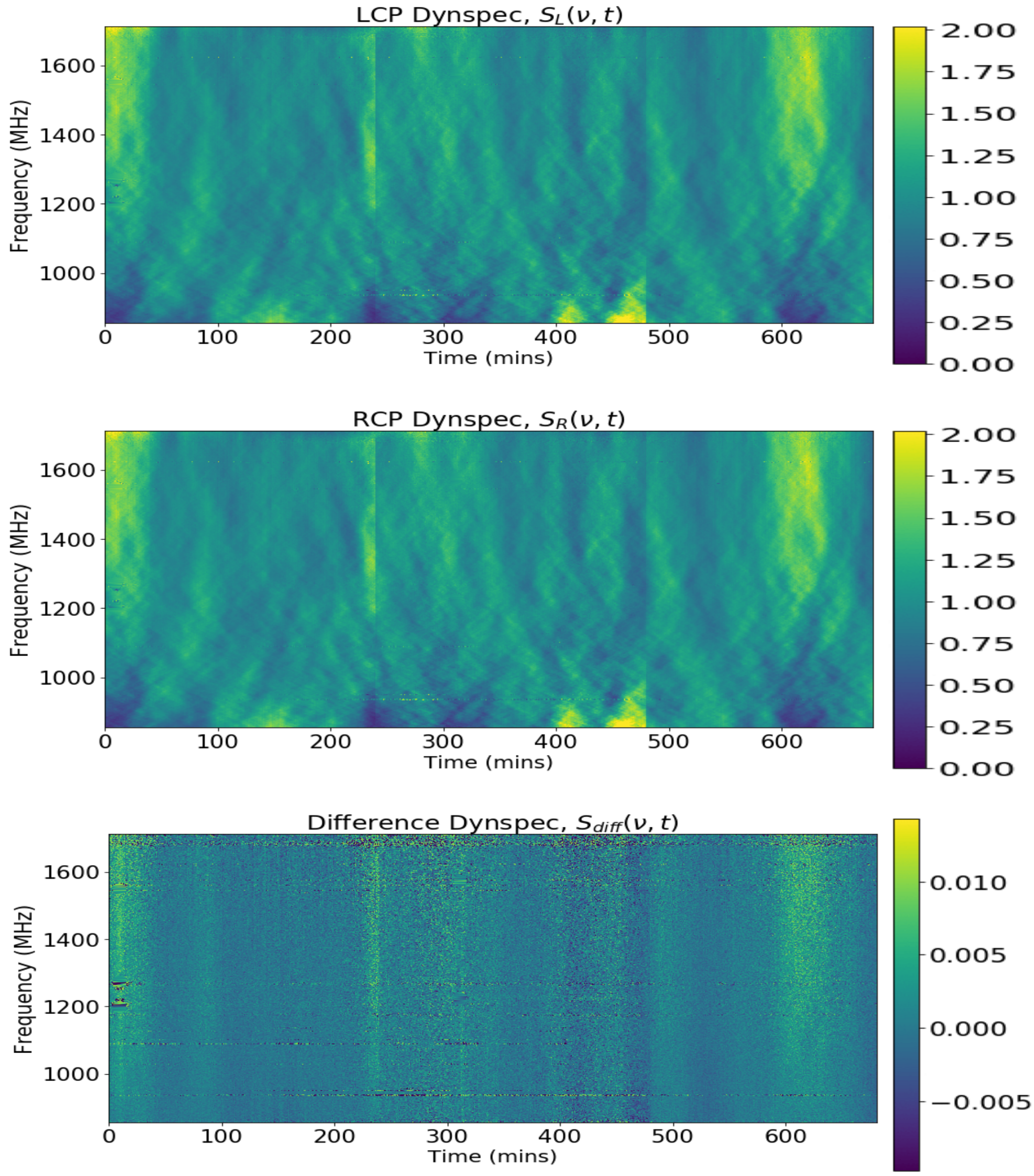


Fig. 3.2: As in Fig. 3.1

**2019-12-28**

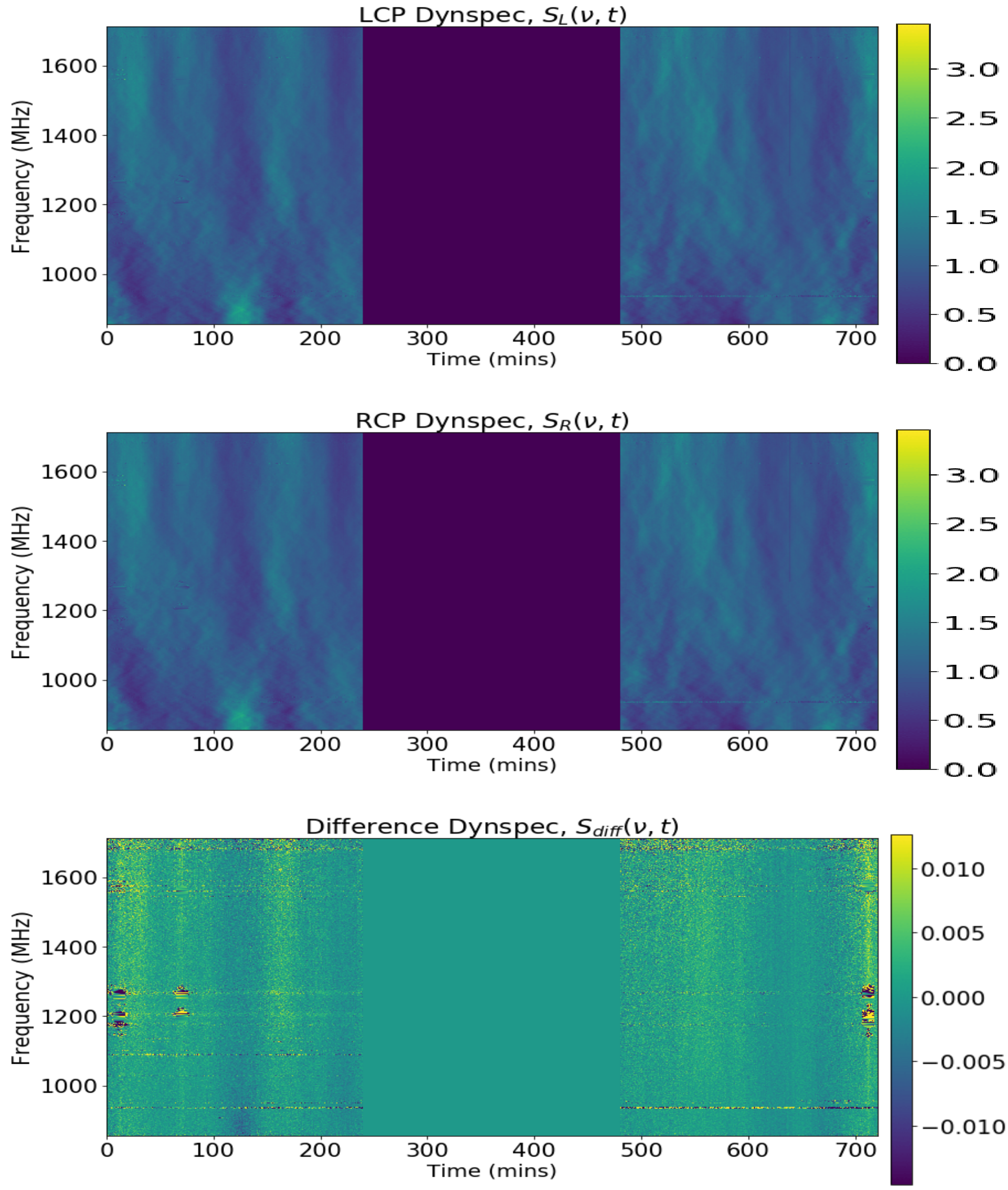


Fig. 3.3: As in Fig. 3.1. The middle gap filled with linear interpolation is due to a sub-integration that failed further processing with psrflux due of FITSIO error.

**2019-12-29**

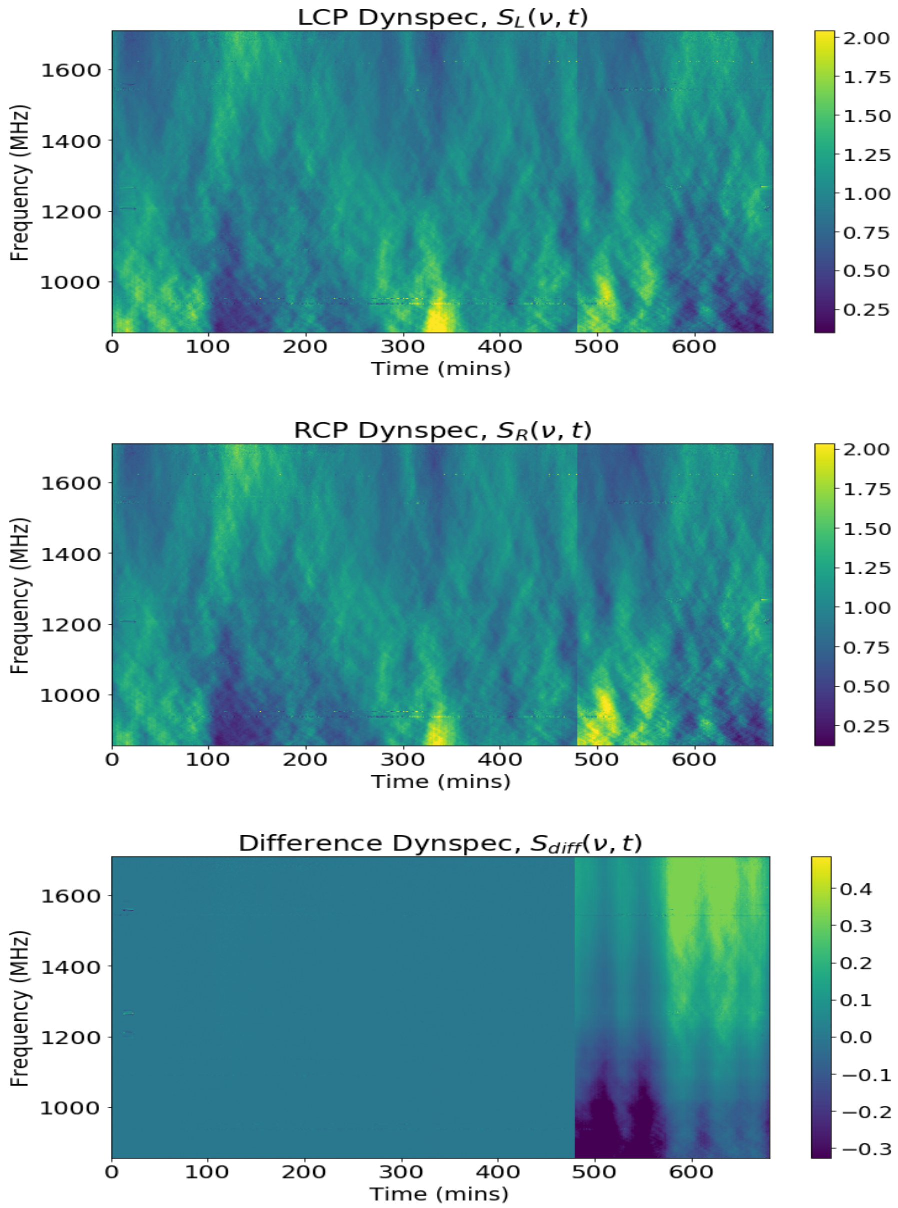


Fig. 3.4: As in Fig. 3.1. The apparent discontinuity of the spectrum at $t = 480$ minutes is a result of differential phase calibration error.

**2019-12-30**

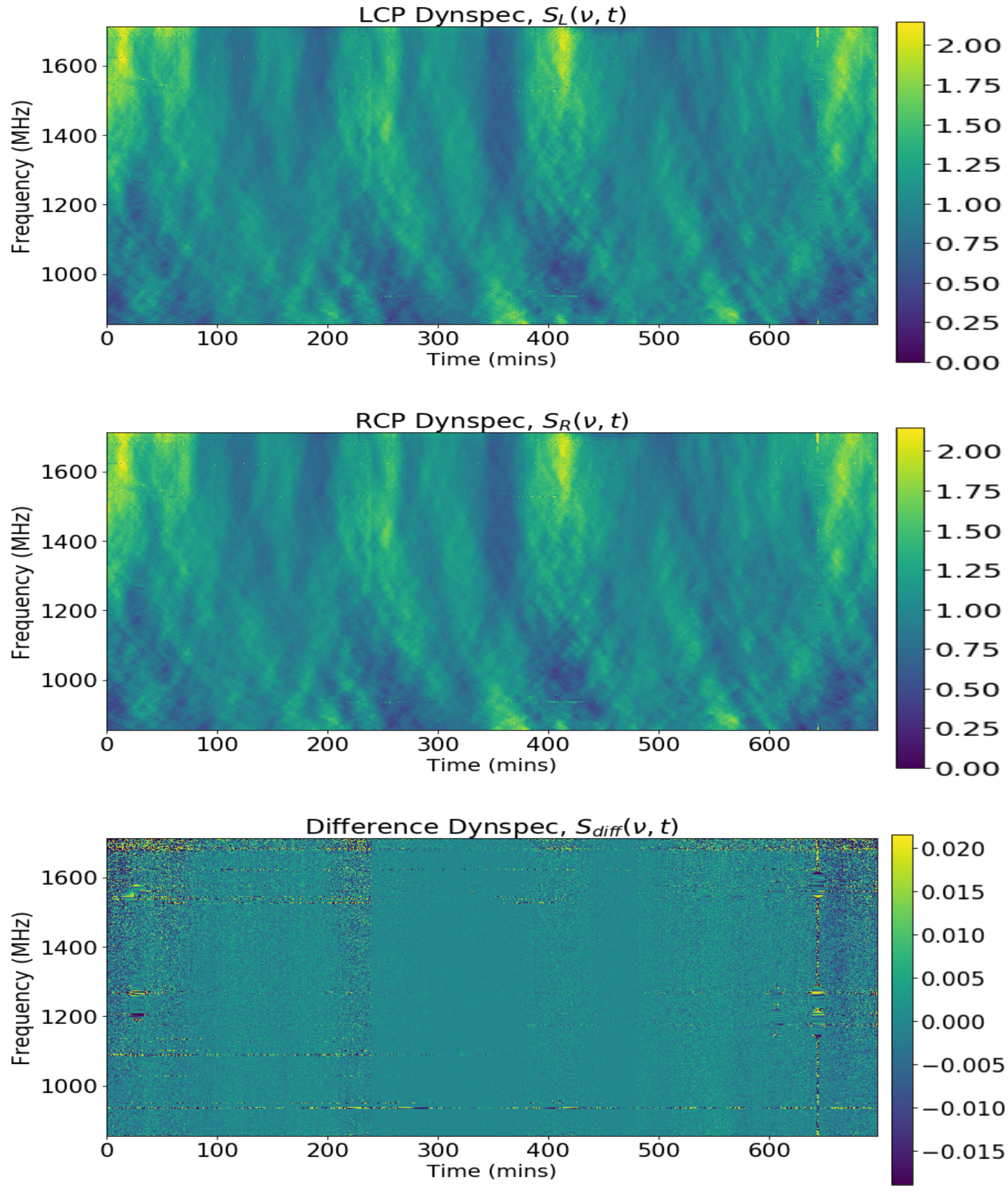


Fig. 3.5: As in Fig. 3.1

**2019-12-31**

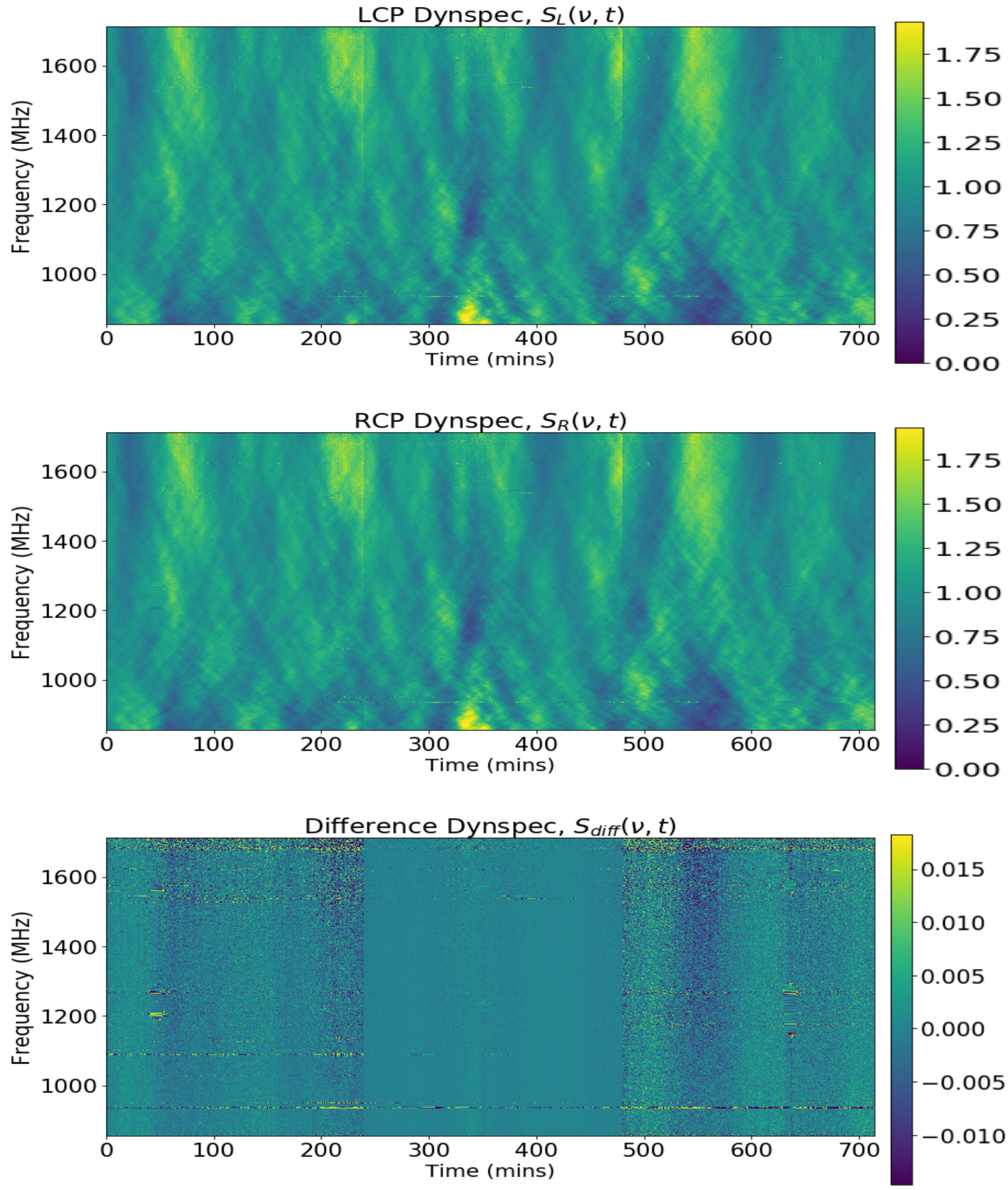


Fig. 3.6: As in Fig. 3.1

### 3.1.2 Secondary Spectra

#### 2019-12-26

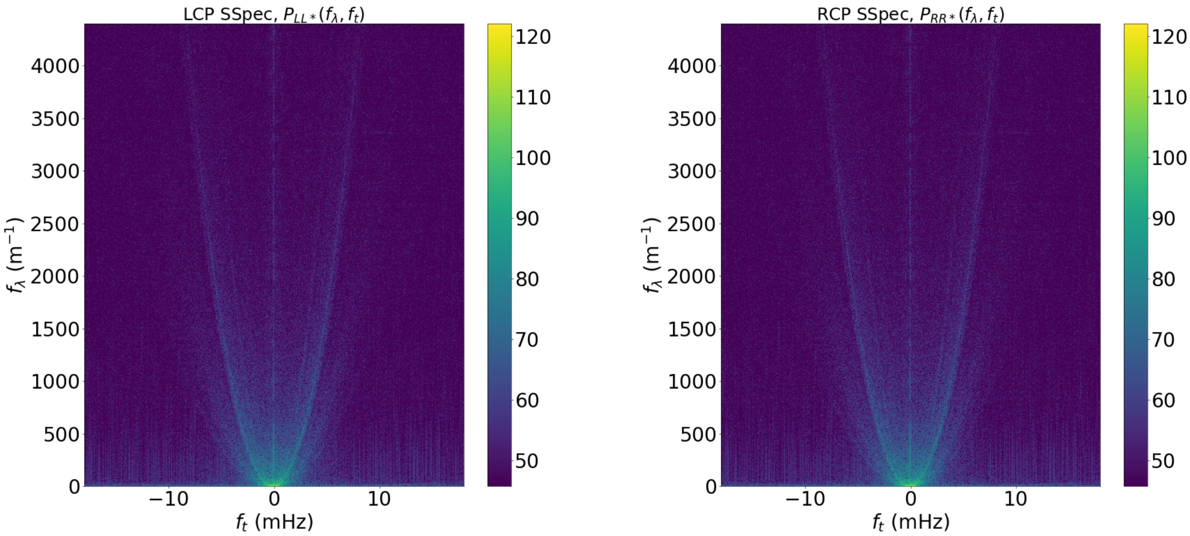


Fig. 3.7: Secondary spectrum of LCP and RCP $P_{LL^*}(f_\lambda, f_t)$ and $P_{RR^*}(f_\lambda, f_t)$

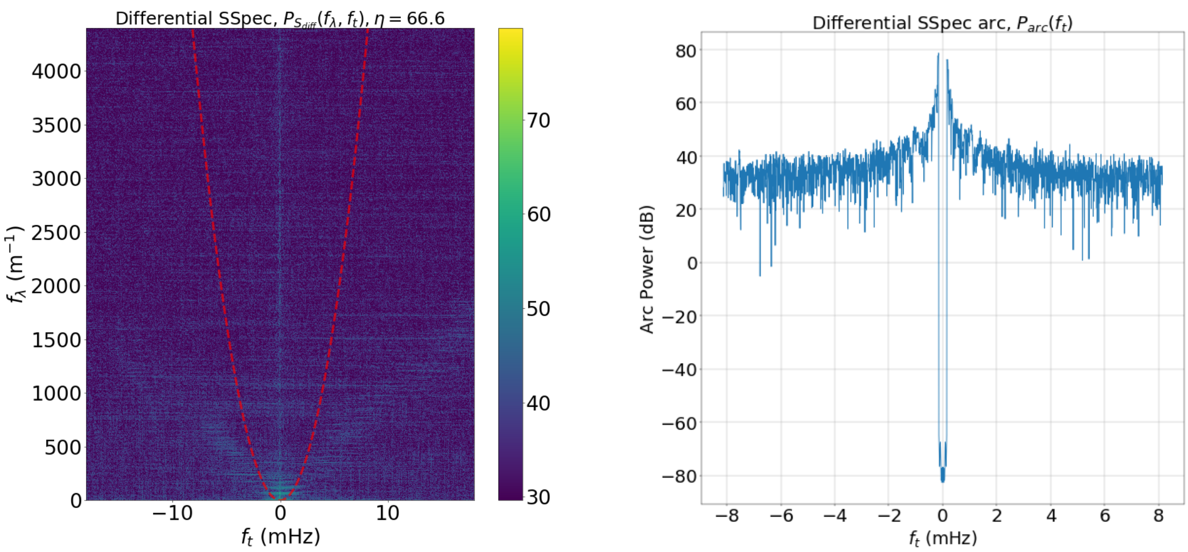


Fig. 3.8: Secondary spectrum of difference spectrum $P_{S_{\mathrm{diff}}}(f_\lambda, f_t)$, and $P_{\eta\,=\,66.6}(f_t)$

**2019-12-27**

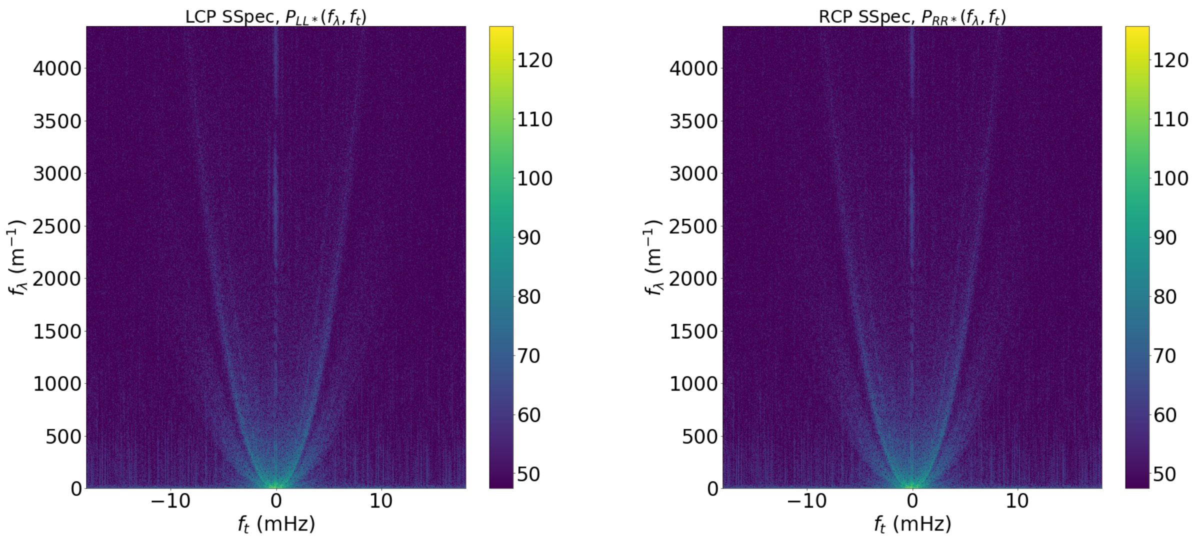


Fig. 3.9: As in Fig. 3.7

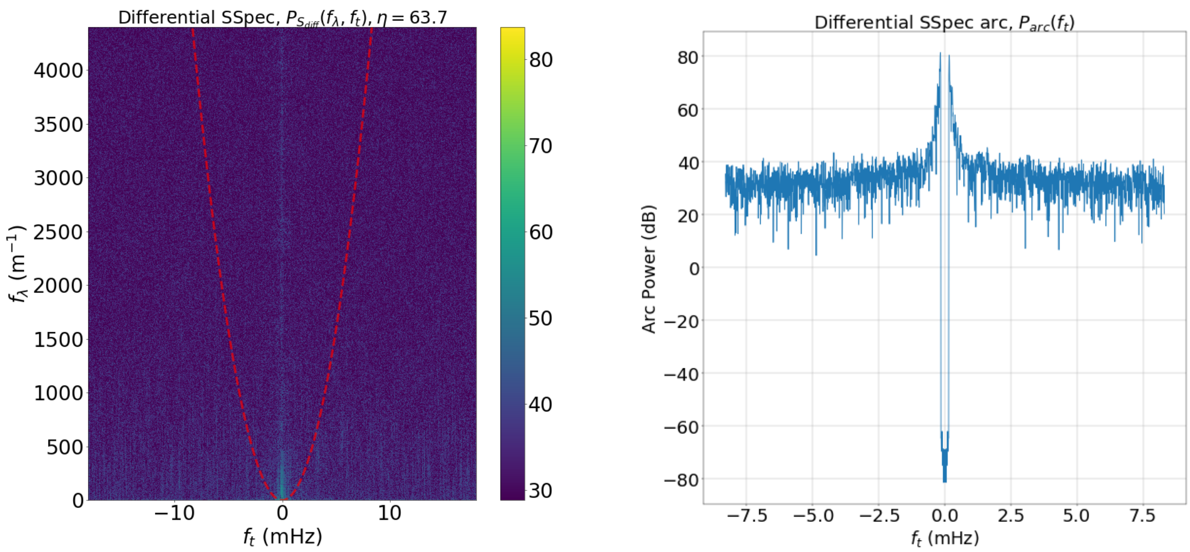


Fig. 3.10: As in Fig. 3.8 with $\eta = 63.7$

### 2019-12-28

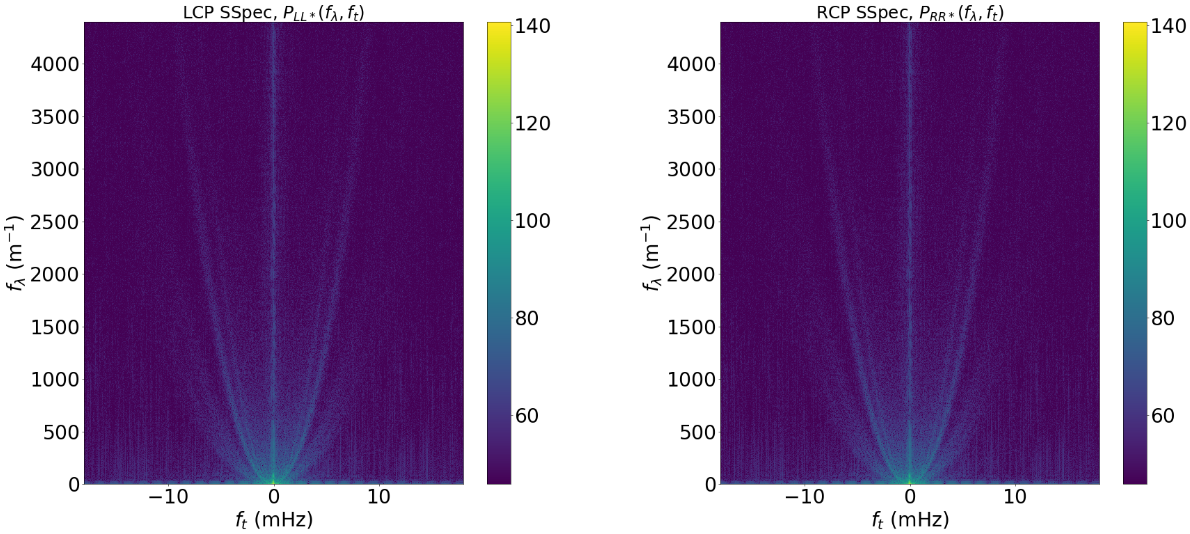


Fig. 3.11: As in Fig. 3.7

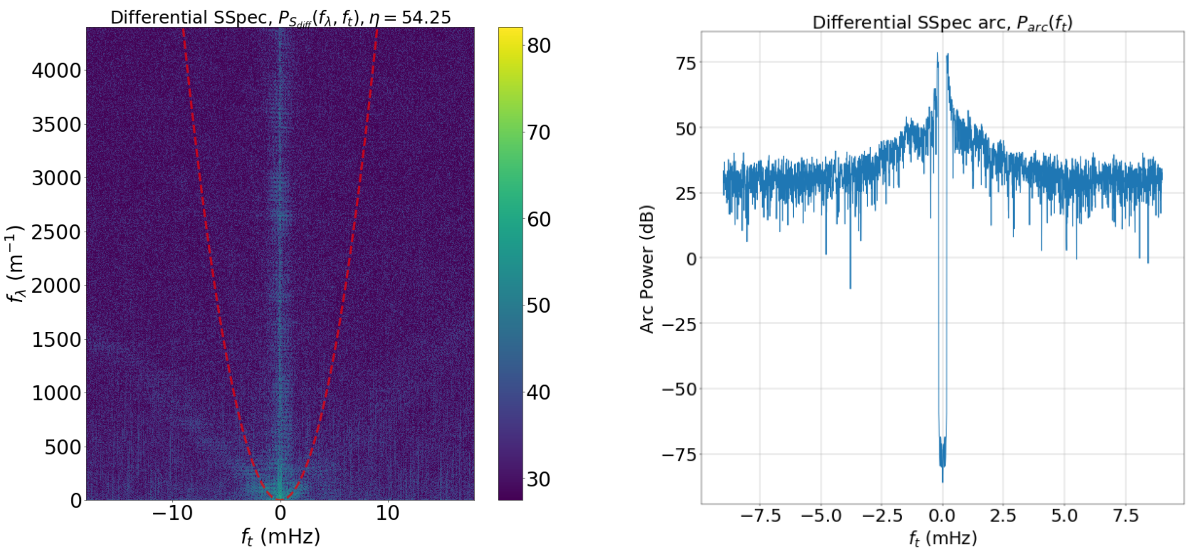


Fig. 3.12: As in Fig. 3.8 with $\eta = 54.25$

### 2019-12-29

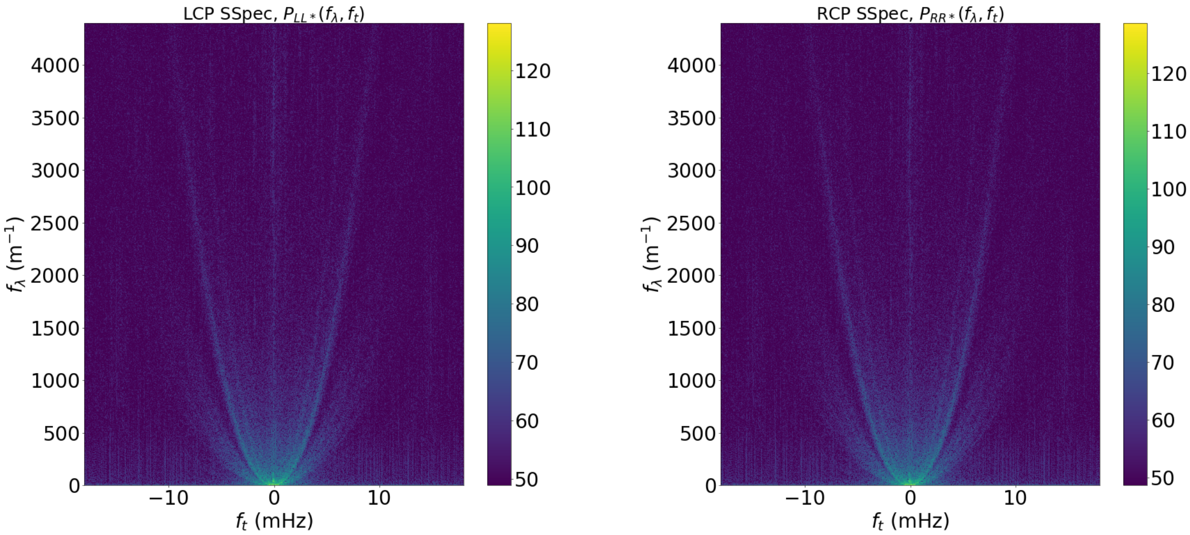


Fig. 3.13: As in Fig. 3.7

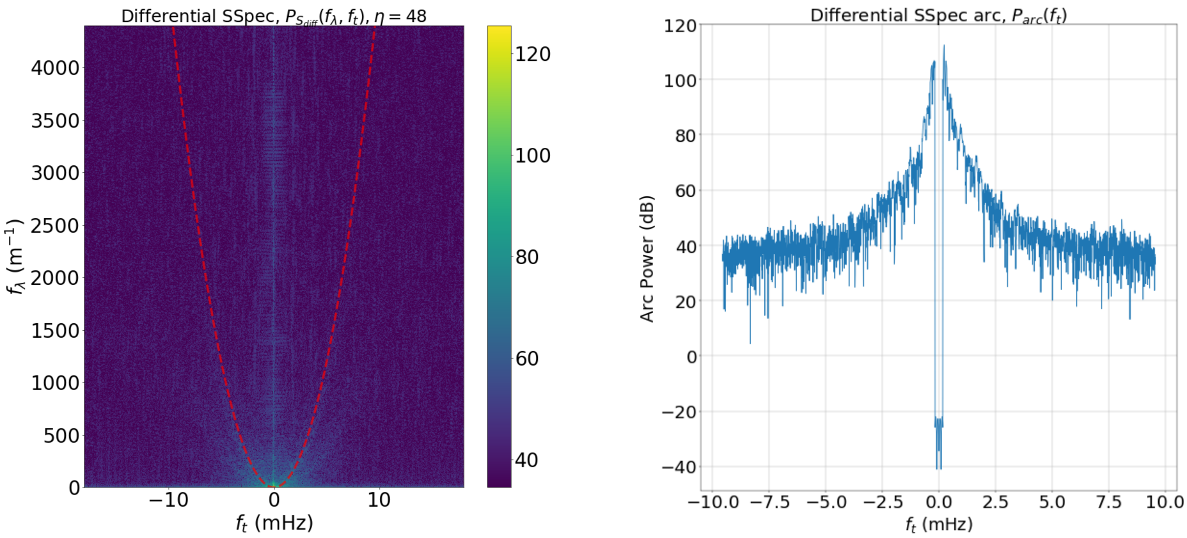


Fig. 3.14: As in Fig. 3.8 with $\eta$ = 48.0

### 2019-12-30

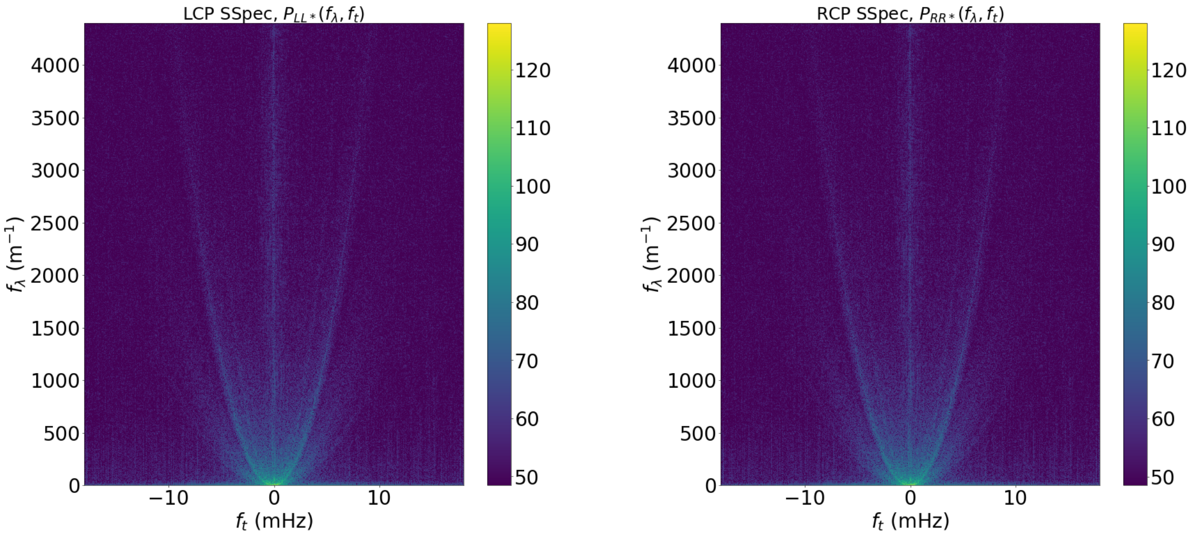


Fig. 3.15: As in Fig. 3.7

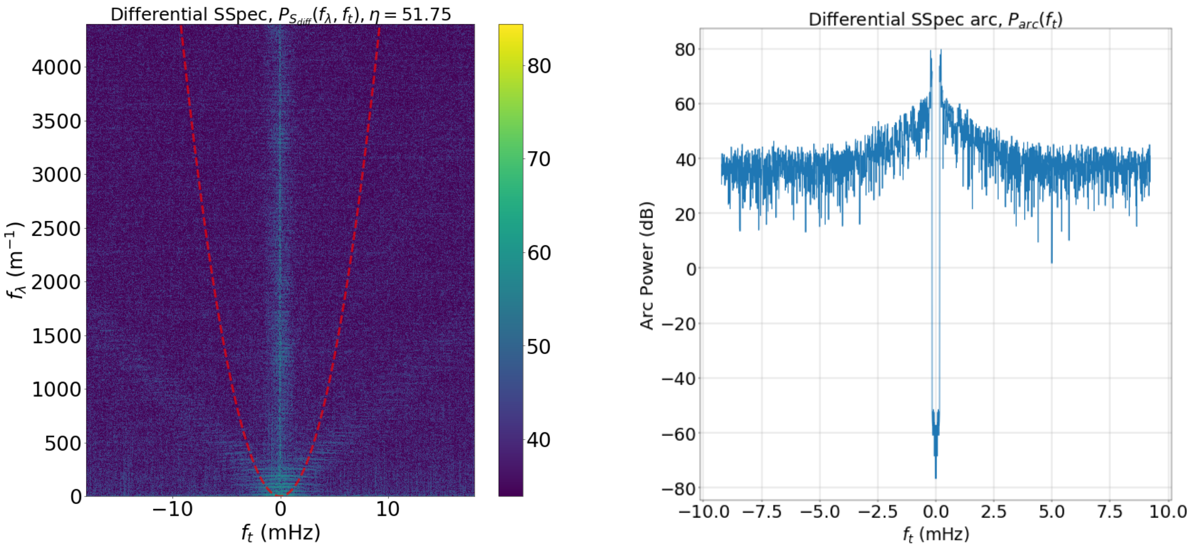


Fig. 3.16: As in Fig. 3.8 with $\eta = 51.75$

### 2019-12-31

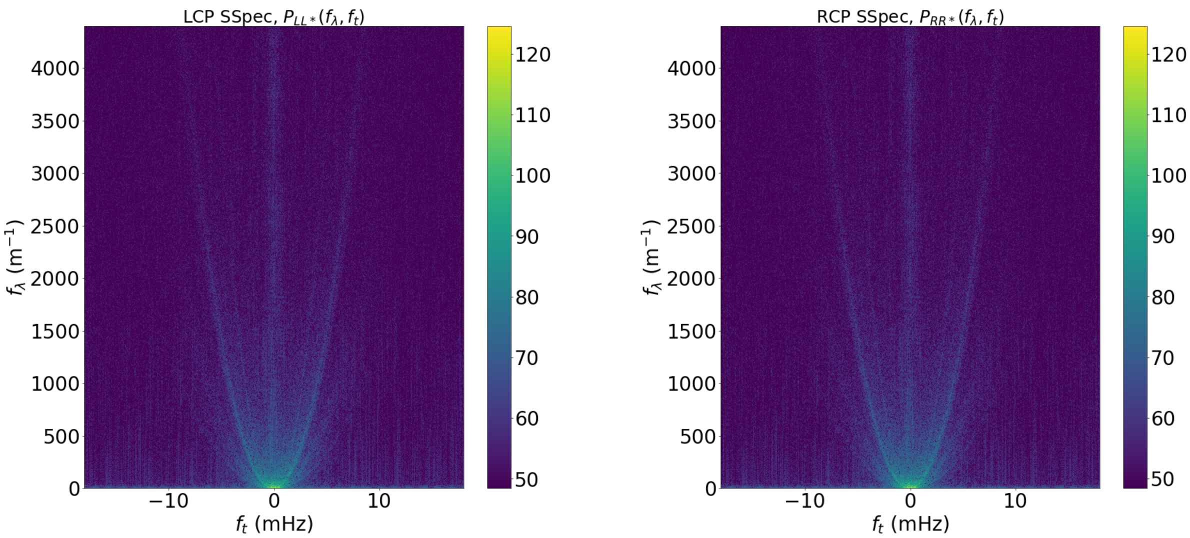


Fig. 3.17: As in Fig. 3.7

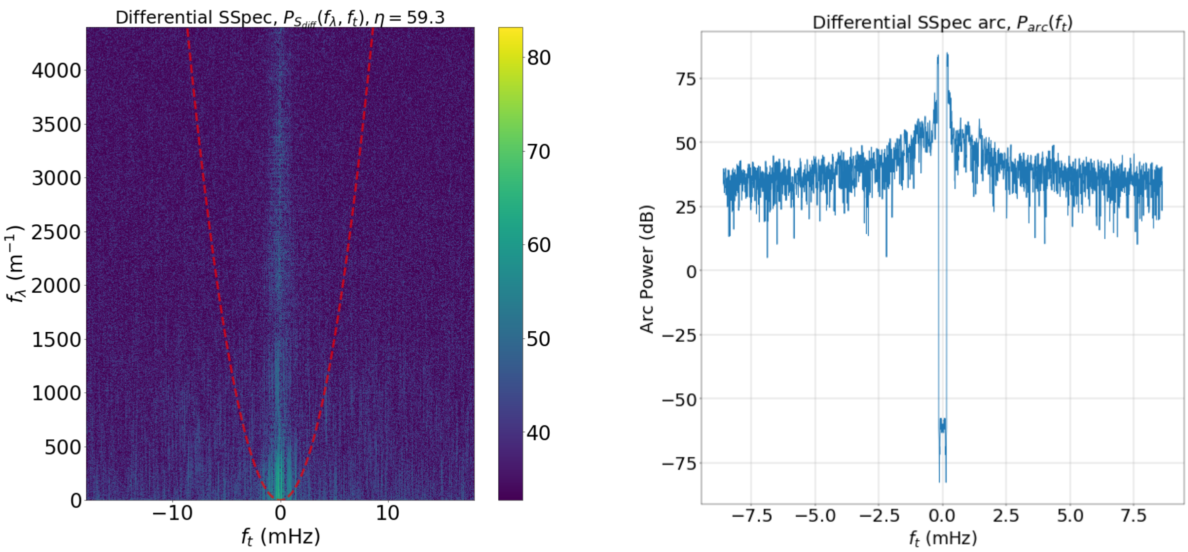


Fig. 3.18: As in Fig. 3.8 with $\eta = 59.3$

## 3.2 Secondary Cross Spectra

### 2019-12-26

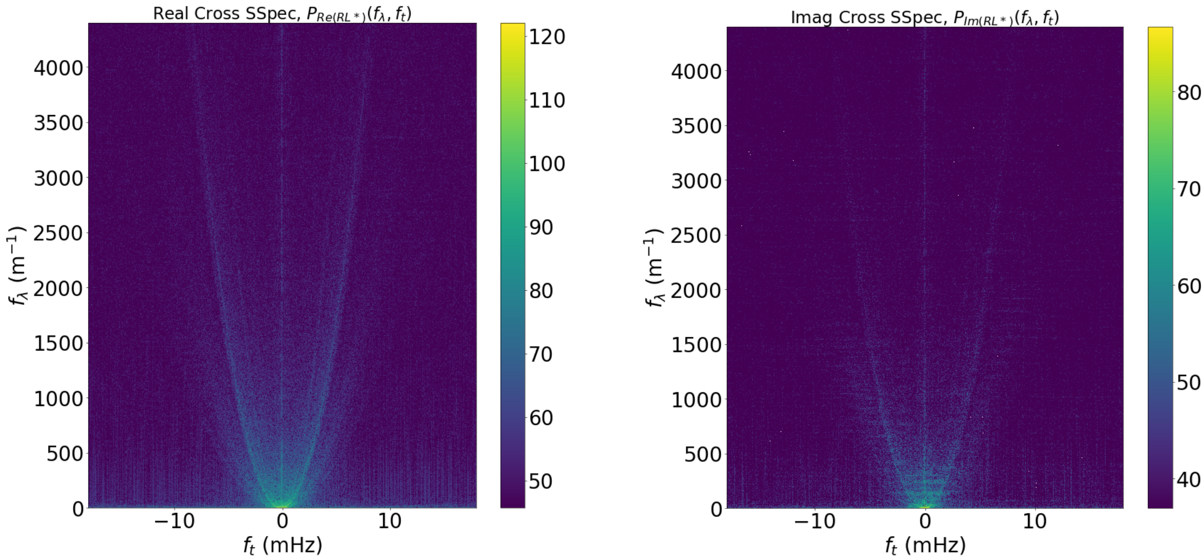


Fig. 3.19: $P_{\mathrm{Re}(RL^*)}(f_\lambda, f_t)$ and $P_{\mathrm{Im}(RL^*)}(f_\lambda, f_t)$

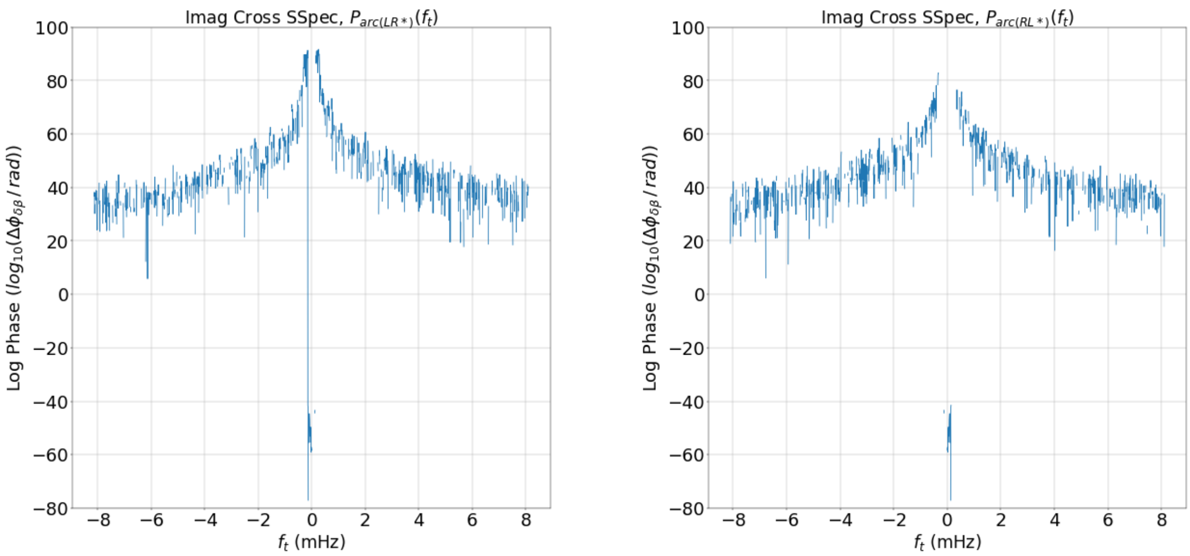


Fig. 3.20: $P_{\mathrm{arc}(LR^*)}(f_t)$ and $P_{\mathrm{arc}(RL^*)}(f_t)$

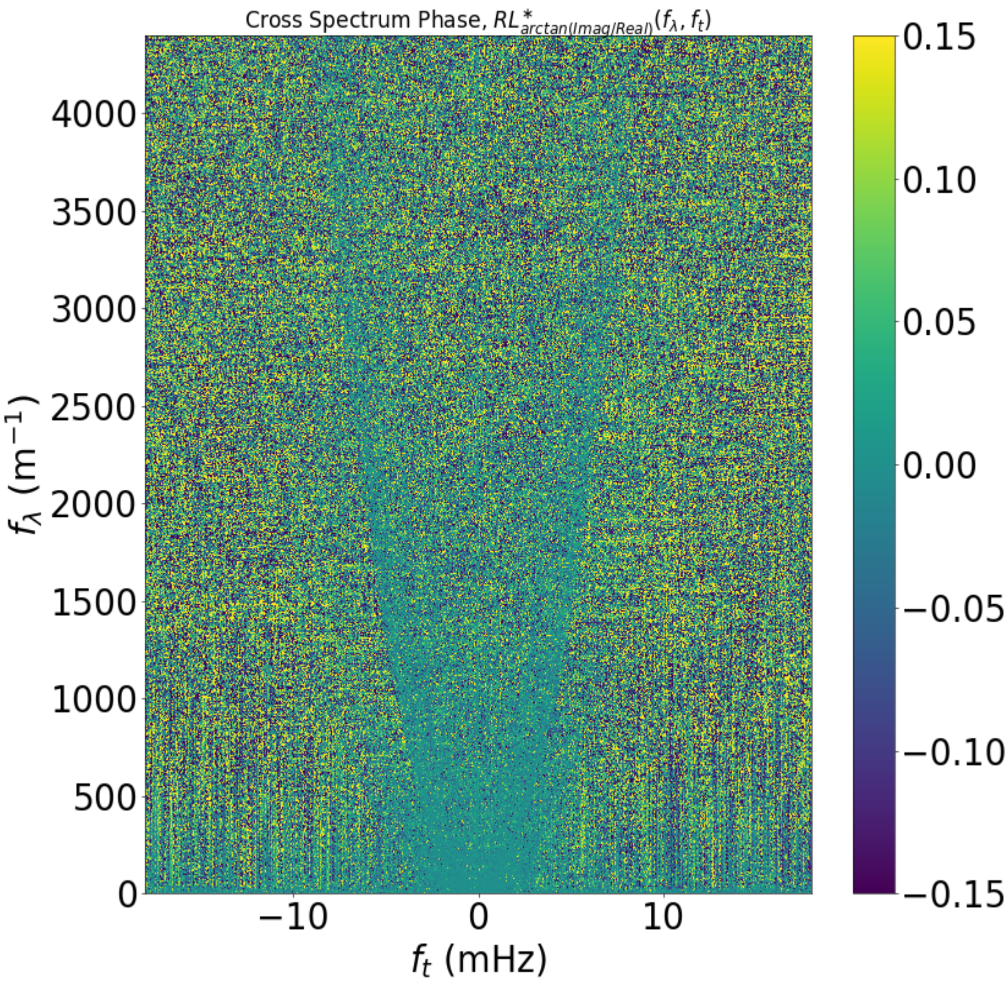


Fig. 3.21: Phase of $RL^*$ Cross Spectra from observations of 2019-12-26. The phase has been restricted between -0.15 and 0.15 to improve dynamic range.

| **Run length** | **Average power** | $f_t$ **span (mHz)** | $f_t$ **center (mHz)** | **Classification** |
|---|---|---|---|---|
| 8 | 34.56 | 0.0534 | -9.3422 | High $f_\lambda$ and $\|f_t\|$, arc within noise field |
| 8 | 35.61 | 0.0534 | -6.7329 | Outer arc negative $f_t$ |
| 8 | 36.51 | 0.0534 | -5.6725 | Outer arc negative $f_t$ |
| 8 | 47.61 | 0.0534 | -2.1935 | Inner arc negative $f_t$ |
| 8 | 34.77 | 0.0534 | -6.8932 | Outer arc negative $f_t$ |
| 9 | 50.61 | 0.0610 | -2.8915 | Inner arc negative $f_t$ |
| 9 | 44.14 | 0.0610 | 2.8915 | Inner arc positive $f_t$ |
| 10 | 31.26 | 0.0687 | -8.8997 | High $f_\lambda$ and $f_t$, arc is in the noise field |
| 11 | 43.62 | 0.0763 | 3.2120 | Inner arc positive $f_t$ |
| 13 | 52.6 | 0.0916 | -1.9455 | Inner arc negative $f_t$ |

Table 3.1: Analysis of 10 longest signal runs from $P_{\text{arc}}(f_t)$ of $P_{\text{Im}(\text{RL}^*)}(f_\lambda, f_t)$ secondary cross spectrum. The run length is the number samples that make up the signal run length along the parabola. The average power is the sum of the amplitudes of the samples divided by the run length. The $f_t$ span is the absolute value of the difference between the first $f_t$ and last $f_t$ of the sample. The $f_t$ center is the midpoint between the first $f_t$ and last $f_t$ of the sample localised on the $f_t$ axis and the classification refers to a segmentation of the parabola as defined by the introduction of Chapter 3.

| **Run length** | **Average power** | $f_t$ **span (mHz)** | $f_t$ **center (mHz)** | **Classification** |
|---|---|---|---|---|
| 8 | 34.85 | 0.0534 | 9.0446 | High $f_\lambda$ and $\|f_t\|$, arc within noise field |
| 8 | 67.94 | 0.0534 | 0.6447 | Inner arc positive $f_t$ |
| 9 | 41.98 | 0.0610 | 3.3646 | Inner arc positive $f_t$ |
| 10 | 51.75 | 0.0687 | -1.8578 | Inner arc negative $f_t$ |
| 10 | 65.82 | 0.0687 | -0.7057 | Inner arc negative $f_t$ |
| 11 | 49.72 | 0.0764 | 2.7847 | Inner arc positive $f_t$ |
| 11 | 73.5 | 0.0764 | 0.4196 | Inner arc positive $f_t$ |
| 15 | 45.07 | 0.1068 | 3.891 | Inner arc positive $f_t$ |
| 20 | 84.16 | 0.145 | 0.2785 | Inner arc positive $f_t$ |
| 27 | 65.39 | 0.1984 | -0.2213 | Inner arc negative $f_t$ |

Table 3.2: Analysis of 10 longest signal runs from $P_{\text{arc}}(f_t)$ of $P_{\text{Im}(\text{LR}^*)}(f_\lambda, f_t)$ secondary cross spectrum. Table column definitions are similar to Table 3.1

### 2019-12-27

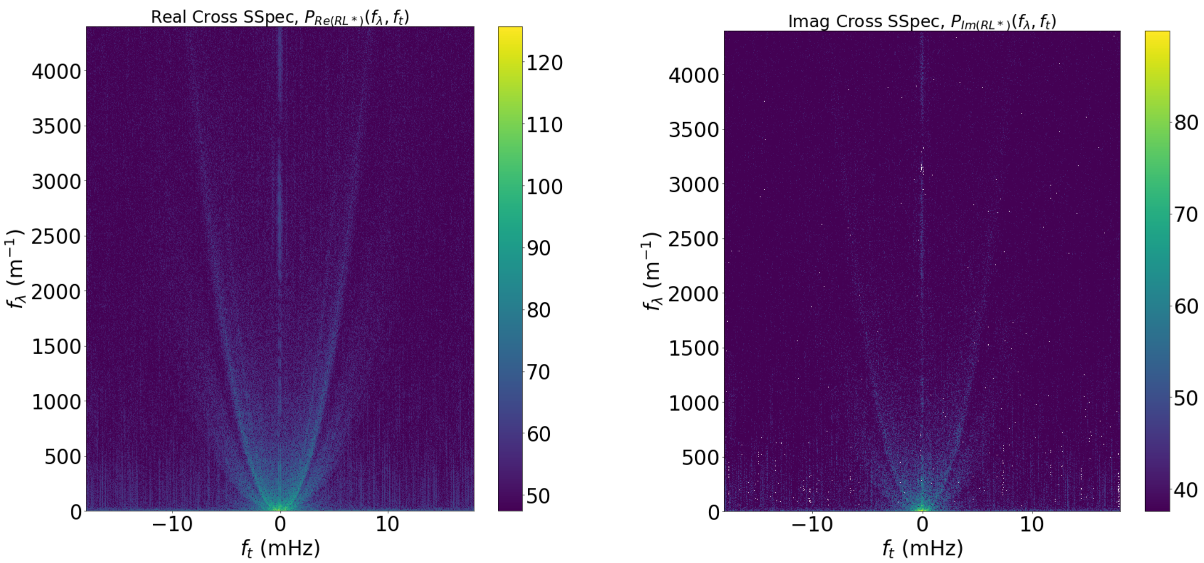


Fig. 3.22: As in Fig. 3.19

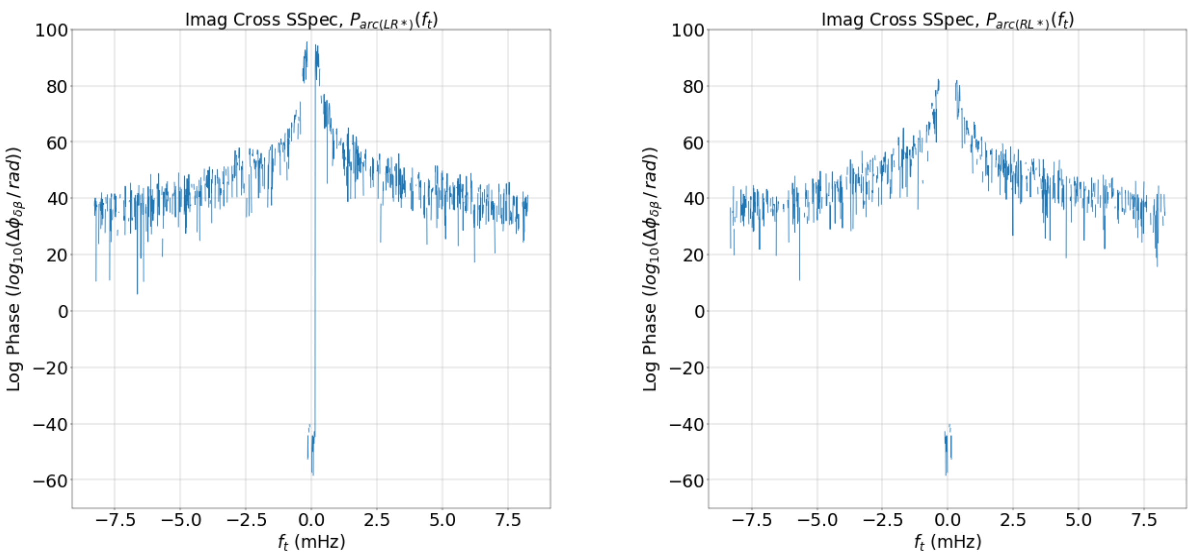


Fig. 3.23: As in Fig. 3.20

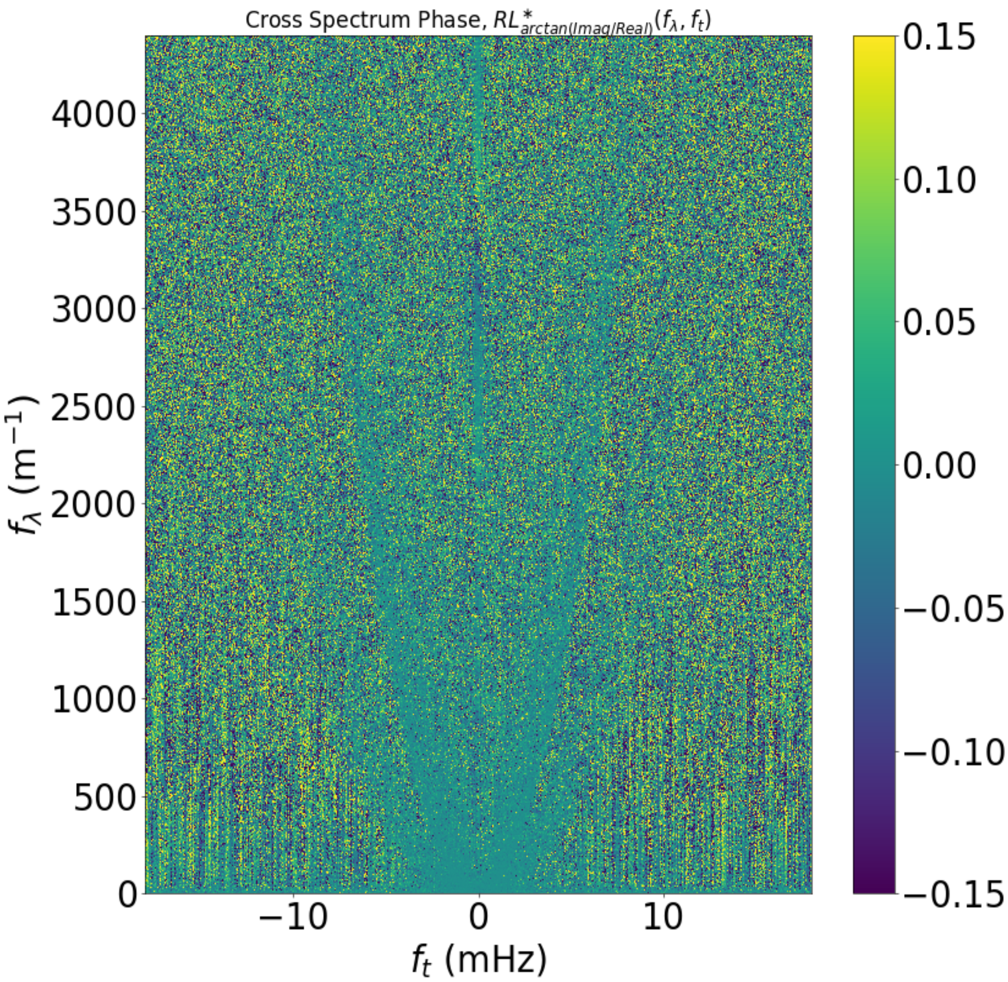


Fig. 3.24: Phase of $RL^*$ Cross Spectra from observations of 2019-12-27. The phase has been restricted between -0.15 and 0.15 to improve dynamic range.

| **Run length** | **Average power** | $f_t$ **span (mHz)** | $f_t$ **center (mHz)** | **Classification** |
|---|---|---|---|---|
| 8 | -52.78 | 0.0534 | -0.0191 | Noise within central blanked region. |
| 8 | 42.99 | 0.0534 | 6.2828 | Outer arc positive $f_t$ |
| 9 | 35.98 | 0.0610 | -5.4245 | Outer arc negative $f_t$ |
| 9 | 45.61 | 0.0610 | 2.8076 | Inner arc positive $f_t$ |
| 10 | 34.99 | 0.0687 | -8.3199 | High $f_\lambda$ and $\|f_t\|$, arc within noise field |
| 10 | 77.05 | 0.0687 | -0.3624 | Inner arc negative $f_t$ |
| 10 | 74.34 | 0.0687 | 0.4311 | Inner arc positive $f_t$ |
| 11 | 58.2 | 0.0763 | 0.9155 | Inner arc positive $f_t$ |
| 11 | 58.85 | 0.0763 | -1.2894 | Inner arc negative $f_t$ |
| 15 | 53.9 | 0.1068 | -1.709 | Inner arc negative $f_t$ |

Table 3.3: Analysis of 10 longest signal runs from $P_{\text{arc}}(f_t)$ of $P_{\text{Im(RL}^*)}(f_\lambda, f_t)$ secondary cross spectrum. Table column definitions are similar to Table 3.1.

| **Run length** | **Average power** | $f_t$ **span (mHz)** | $f_t$ **center (mHz)** | **Classification** |
|---|---|---|---|---|
| 8 | 58.47 | 0.0534 | 1.5907 | Inner arc positive $f_t$ |
| 8 | 46.57 | 0.0534 | -2.636 | Inner arc negative $f_t$ |
| 9 | 36.93 | 0.0610 | -4.7684 | Inner arc negative $f_t$ |
| 9 | 38.58 | 0.0610 | 8.1863 | High $f_\lambda$ and $\|f_t\|$, arc within noise field |
| 9 | 57.71 | 0.0610 | 1.3962 | Inner arc positive $f_t$ |
| 10 | 35.58 | 0.0687 | -7.6561 | High $f_\lambda$ and $\|f_t\|$, arc within noise field |
| 15 | 50.48 | 0.1068 | -1.9836 | Inner arc negative $f_t$ |
| 17 | 54.74 | 0.1221 | 1.7624 | Inner arc positive $f_t$ |
| 20 | 82.49 | 0.145 | 0.2174 | Inner arc positive $f_t$ |
| 23 | 88.22 | 0.1678 | -0.2365 | Inner arc negative $f_t$ |

Table 3.4: Analysis of 10 longest signal runs from $P_{\text{arc}}(f_t)$ of $P_{\text{Im(LR}^*)}(f_\lambda, f_t)$ secondary cross spectrum. Table column definitions are similar to Table 3.1.

### 2019-12-28

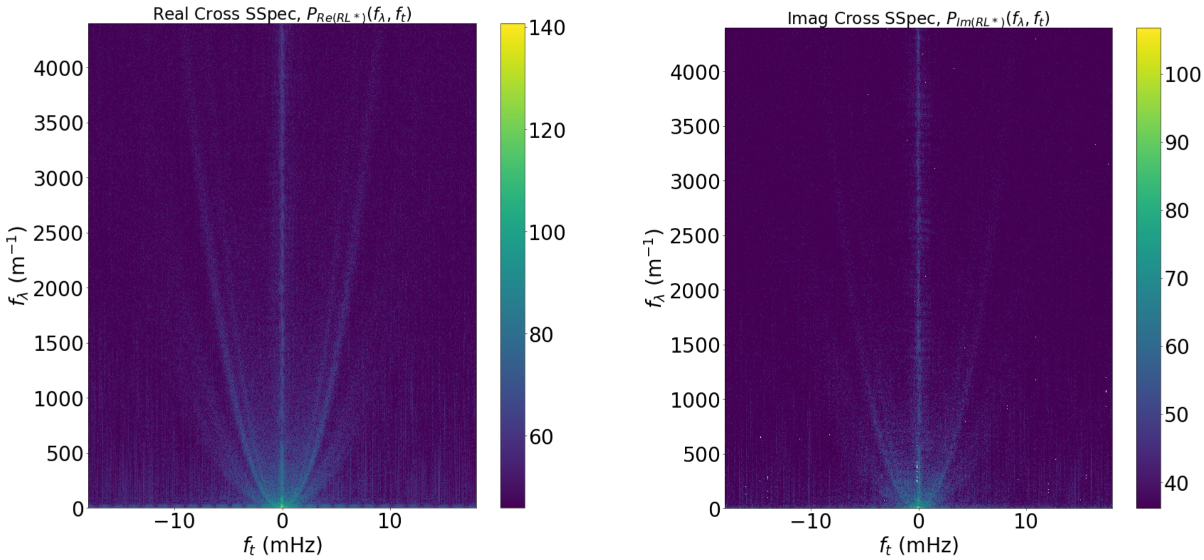


Fig. 3.25: As in Fig. 3.19

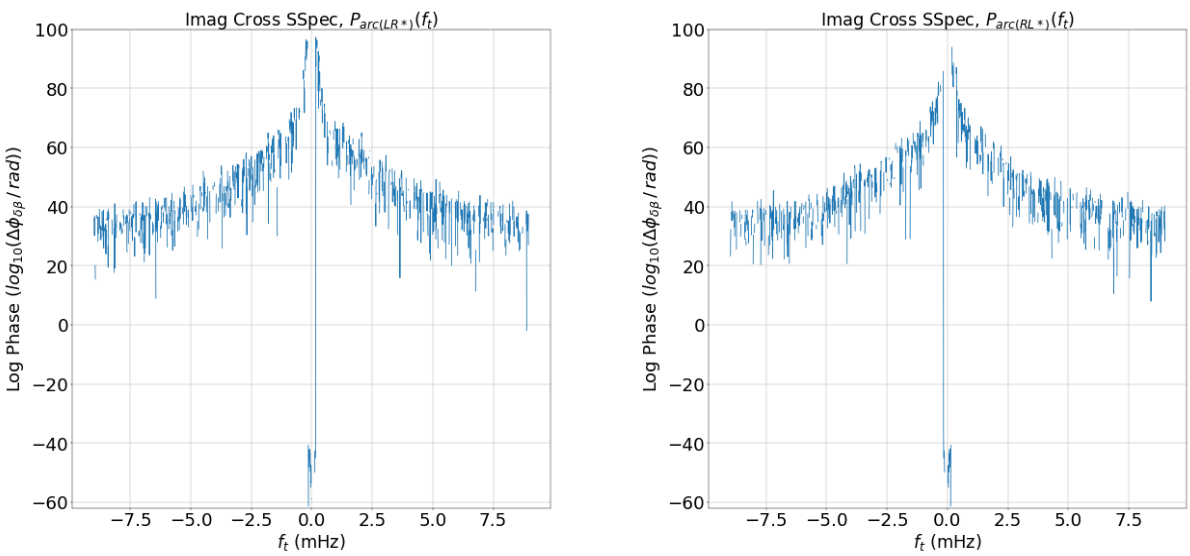


Fig. 3.26: As in Fig. 3.20

| **Run length** | **Average power** | $f_t$ **span (mHz)** | $f_t$ **center (mHz)** | **Classification** |
|---|---|---|---|---|
| 8 | 34.09 | 0.0534 | 8.8387 | High $f_\lambda$ and $f_t$, arc is in the noise field |
| 8 | 47.8 | 0.0534 | -3.2845 | Inner arc negative $f_t$ |
| 8 | 34.68 | 0.0534 | -7.5035 | High $f_\lambda$ and $\lvert f_t\rvert$, arc within noise field |
| 8 | 35.24 | 0.0534 | 9.2964 | High $f_\lambda$ and $\lvert f_t\rvert$, arc within noise field |
| 8 | 33.08 | 0.0534 | 7.5645 | High $f_\lambda$ and $\lvert f_t\rvert$, arc within noise field |
| 8 | 47.67 | 0.0534 | 3.1395 | Inner arc positive $f_t$ |
| 9 | 62.16 | 0.0610 | -1.2054 | Inner arc negative $f_t$ |
| 10 | 30.38 | 0.0687 | -6.9847 | High $f_\lambda$ and $\lvert f_t\rvert$, arc within noise field |
| 10 | 62.02 | 0.0687 | 0.7973 | Inner arc positive $f_t$ |
| 11 | 60.29 | 0.0839 | 1.2169 | Inner arc positive $f_t$ |

Table 3.5: Analysis of 10 longest signal runs from $P_{\mathrm{arc}}(f_t)$ of $P_{\mathrm{Im(RL^*)}}(f_\lambda, f_t)$ secondary cross spectrum. Table column definitions are similar to Table 3.1.

| **Run length** | **Average power** | $f_t$ **span (mHz)** | $f_t$ **center (mHz)** | **Classification** |
|---|---|---|---|---|
| 7 | -45.18 | 0.0458 | -0.0763 | Noise within central blanked region. |
| 7 | 48.94 | 0.0458 | 3.7155 | Inner arc positive $f_t$ |
| 7 | 34.66 | 0.0458 | -10.2158 | High $f_\lambda$ and $\lvert f_t\rvert$, arc within noise field |
| 7 | 86.08 | 0.0458 | 0.2823 | Inner arc positive $f_t$ |
| 8 | 80.84 | 0.0534 | -0.3166 | Inner arc negative $f_t$ |
| 8 | 40.49 | 0.0534 | -4.6043 | Inner arc negative $f_t$ |
| 8 | 32.01 | 0.0534 | -9.3498 | High $f_\lambda$ and $\lvert f_t\rvert$, arc within noise field |
| 9 | 48.32 | 0.061 | -3.1357 | Inner arc negative $f_t$ |
| 10 | 38.99 | 0.0687 | 4.9171 | Inner arc positive $f_t$ |
| 11 | 93.67 | 0.0763 | -0.206 | Inner arc negative $f_t$ |

Table 3.6: Analysis of 10 longest signal runs from $P_{\mathrm{arc}}(f_t)$ of $P_{\mathrm{Im(LR^*)}}(f_\lambda, f_t)$ secondary cross spectrum. Table column definitions are similar to Table 3.1.

**2019-12-29**

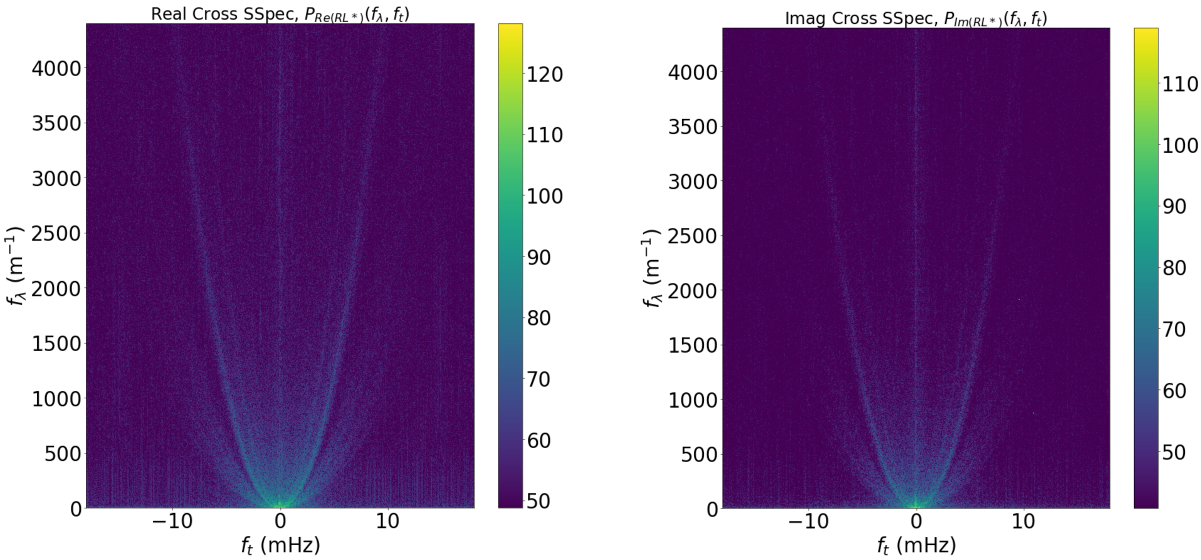


Fig. 3.27: As in Fig. 3.19

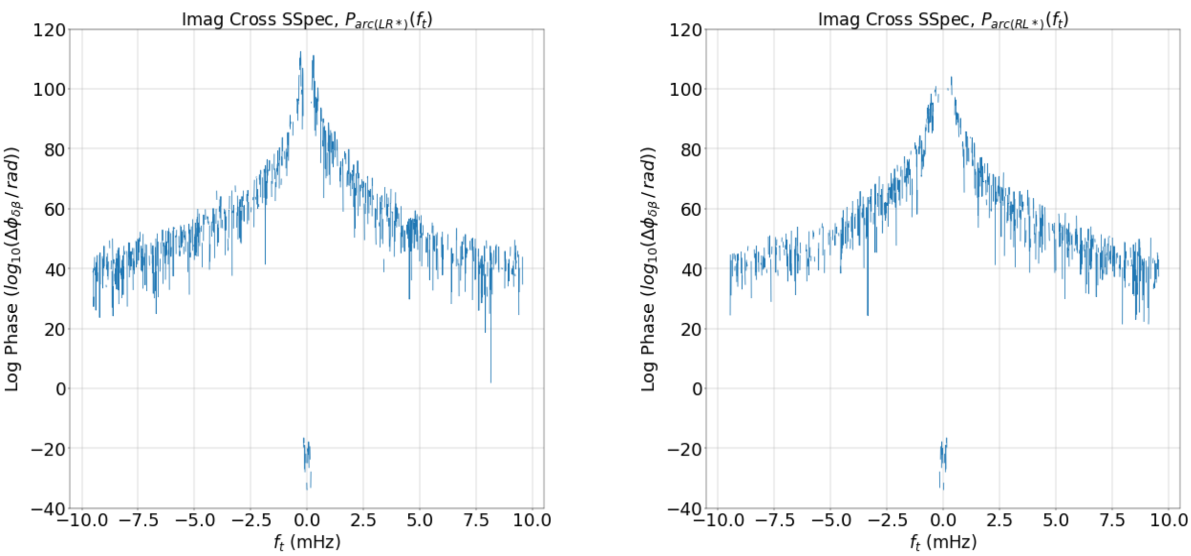


Fig. 3.28: As in Fig. 3.20

| **Run length** | **Average power** | $f_t$ **span (mHz)** | $f_t$ **center (mHz)** | **Classification** |
|---|---|---|---|---|
| 7 | 62.83 | 0.0458 | -1.9455 | Inner arc negative $f_t$ |
| 7 | 73.16 | 0.0458 | -1.6022 | Inner arc negative $f_t$ |
| 8 | 42.94 | 0.0534 | 8.6937 | High $f_\lambda$ and $\|f_t\|$, arc within noise field |
| 9 | 80.59 | 0.061 | -1.0529 | Inner arc negative $f_t$ |
| 10 | 90.45 | 0.0687 | -0.6676 | Inner arc negative $f_t$ |
| 10 | 54.72 | 0.0687 | 3.1548 | Inner arc positive $f_t$ |
| 10 | 33.26 | 0.0687 | 10.3645 | High $f_\lambda$ and $\|f_t\|$, arc within noise field |
| 10 | 59.97 | 0.0687 | -2.5291 | Inner arc negative $f_t$ |
| 13 | 93.32 | 0.0916 | 0.5493 | Inner arc positive $f_t$ |
| 24 | 91.29 | 0.1755 | -0.5302 | Inner arc negative $f_t$ |

Table 3.7: Analysis of 10 longest signal runs from $P_{\mathrm{arc}}(f_t)$ of $P_{\mathrm{Im(RL^*)}}(f_\lambda, f_t)$ secondary cross spectrum. Table column definitions are similar to Table 3.1.

| **Run length** | **Average power** | $f_t$ **span (mHz)** | $f_t$ **center (mHz)** | **Classification** |
|---|---|---|---|---|
| 8 | 57.1 | 0.0534 | -3.994 | Inner arc negative $f_t$ |
| 8 | 42.12 | 0.0534 | -8.2359 | High $f_\lambda$ and $\|f_t\|$, arc within noise field |
| 9 | 53.47 | 0.0610 | -4.1428 | Inner arc negative $f_t$ |
| 9 | 41.72 | 0.0610 | -8.1558 | High $f_\lambda$ and $\|f_t\|$, arc within noise field |
| 9 | 80.3 | 0.0610 | 0.8087 | Inner arc positive $f_t$ |
| 9 | 38.14 | 0.0610 | 7.6294 | High $f_\lambda$ and $\|f_t\|$, arc within noise field |
| 9 | 109.22 | 0.0610 | -0.2899 | Inner arc negative $f_t$ |
| 10 | 92.96 | 0.0687 | 0.4158 | Inner arc positive $f_t$ |
| 10 | 52.4 | 0.0687 | 4.7722 | Inner arc positive $f_t$ |
| 13 | 105.79 | 0.0916 | 0.2594 | Inner arc positive $f_t$ |

Table 3.8: Analysis of 10 longest signal runs from $P_{\mathrm{arc}}(f_t)$ of $P_{\mathrm{Im(LR^*)}}(f_\lambda, f_t)$ secondary cross spectrum. Table column definitions are similar to Table 3.1.

### 2019-12-30

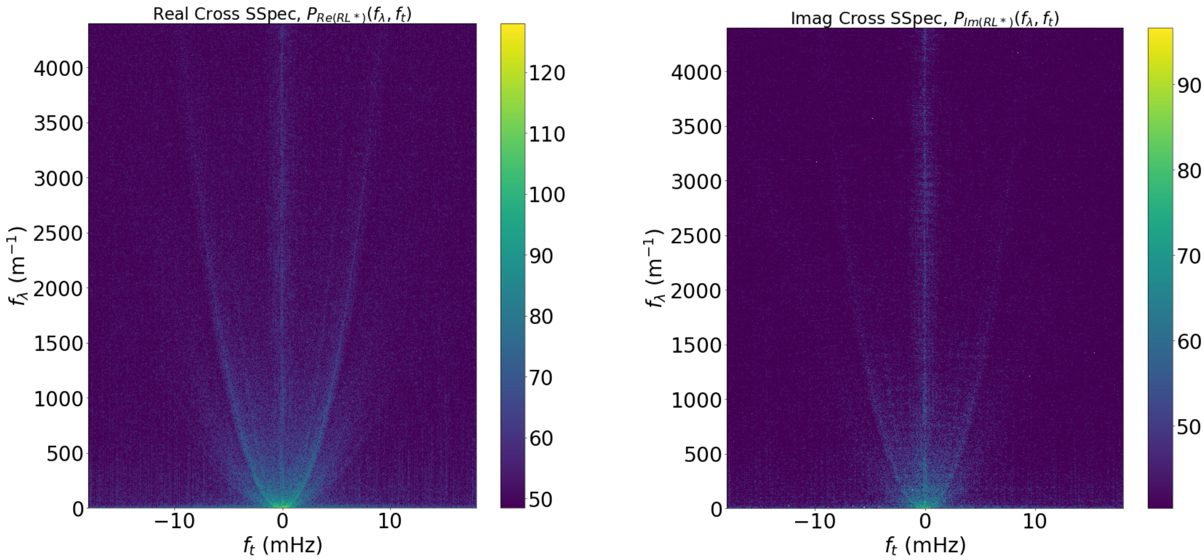


Fig. 3.29: As in Fig. 3.19

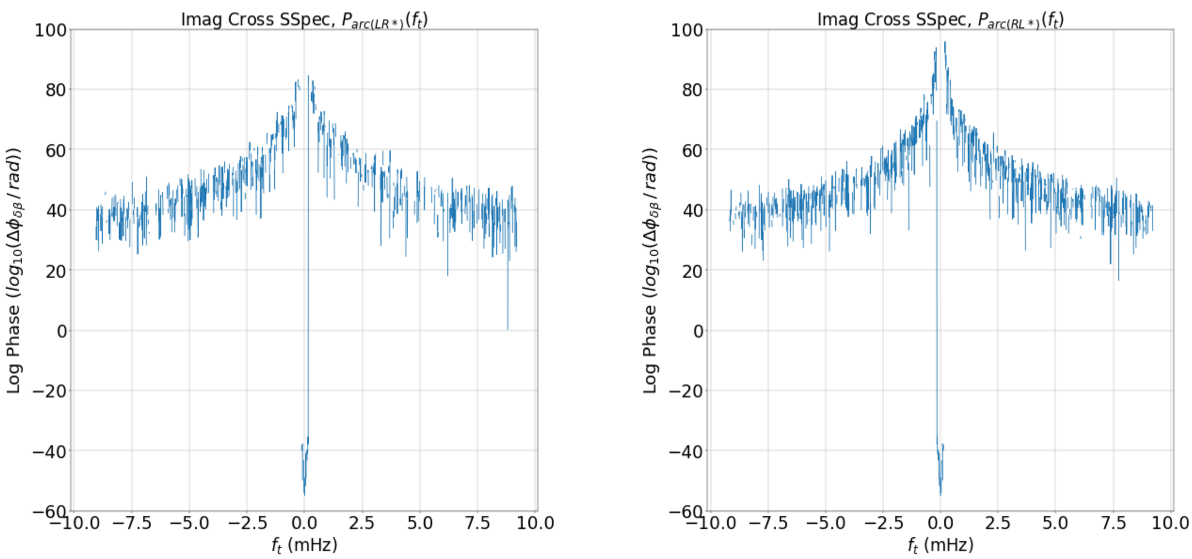


Fig. 3.30: As in Fig. 3.20

| Signal length | Average power | $f_t$ span (mHz) | $f_t$ center (mHz) | Classification |
|---|---|---|---|---|
| 8 | 80.45 | 0.0534 | -0.309 | Inner arc negative $f_t$ |
| 8 | 45.95 | 0.0534 | -2.6512 | Inner arc negative $f_t$ |
| 8 | 55.24 | 0.0534 | 2.0561 | Inner arc positive $f_t$ |
| 8 | 42.70 | 0.0534 | 5.8784 | Outer arc positive $f_t$ |
| 9 | 38.11 | 0.0610 | 7.4081 | High $f_\lambda$ and $\lvert f_t \rvert$, arc within noise field |
| 9 | 52.96 | 0.0610 | 2.7161 | Inner arc positive $f_t$ |
| 9 | 67.98 | 0.0610 | -1.0605 | Inner arc negative $f_t$ |
| 9 | 41.46 | 0.0610 | -6.0425 | Outer arc negative $f_t$ |
| 10 | 58.4 | 0.0687 | -1.7433 | Inner arc negative $f_t$ |
| 13 | 50.49 | 0.0916 | 3.7842 | Inner arc positive $f_t$ |

Table 3.9: Analysis of 10 longest signal runs from $P_{\text{arc}}(f_t)$ of $P_{\text{Im(RL}^*)}(f_\lambda, f_t)$ secondary cross spectrum. Table column definitions are similar to Table 3.1.

| Signal length | Average power | $f_t$ span (mHz) | $f_t$ center (mHz) | Classification |
|---|---|---|---|---|
| 7 | 38.46 | 0.0458 | -8.6441 | High $f_\lambda$ and $\lvert f_t \rvert$, arc within noise field |
| 7 | 32.77 | 0.0458 | 9.3155 | High $f_\lambda$ and $\lvert f_t \rvert$, arc within noise field |
| 7 | 48.07 | 0.0458 | -3.3875 | Inner arc negative $f_t$ |
| 8 | 45.15 | 0.0534 | -3.7117 | Inner arc negative $f_t$ |
| 8 | 42.69 | 0.0534 | -4.7569 | Inner arc negative $f_t$ |
| 8 | 39.44 | 0.0534 | -8.2741 | High $f_\lambda$ and $\lvert f_t \rvert$, arc within noise field |
| 9 | 35.35 | 0.0610 | 10.0174 | High $f_\lambda$ and $\lvert f_t \rvert$, arc within noise field |
| 9 | 66.05 | 0.0610 | 0.6256 | Inner arc positive $f_t$ |
| 9 | 78.73 | 0.0610 | 0.3815 | Inner arc positive $f_t$ |
| 11 | 37.1 | 0.0763 | -8.0872 | High $f_\lambda$ and $\lvert f_t \rvert$, arc within noise field |

Table 3.10: Analysis of 10 longest signal runs from $P_{\text{arc}}(f_t)$ of $P_{\text{Im(LR}^*)}(f_\lambda, f_t)$ secondary cross spectrum. Table column definitions are similar to Table 3.1.

## 2019-12-31

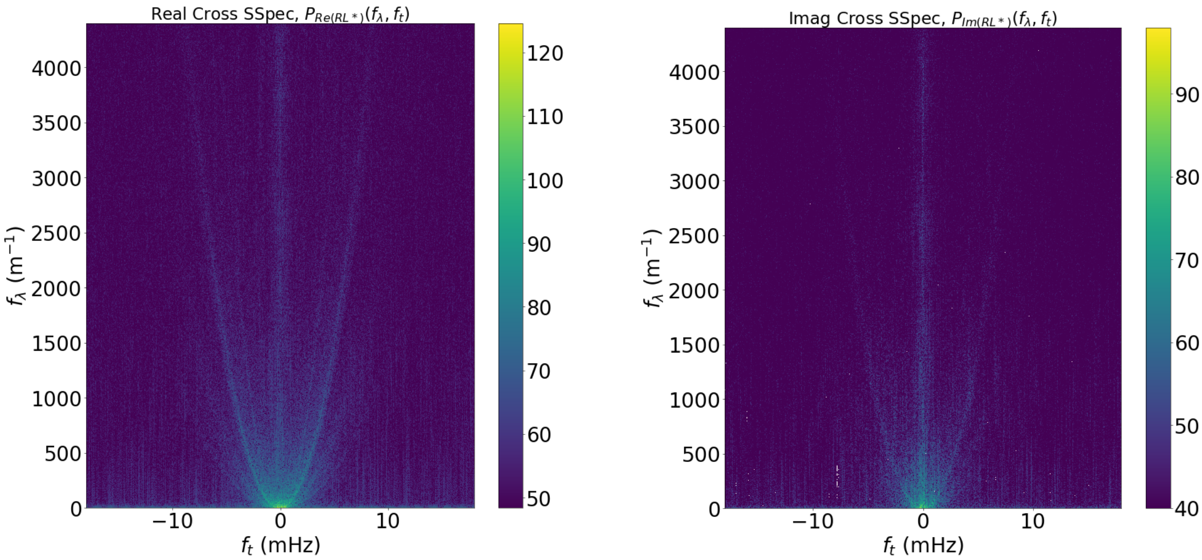


Fig. 3.31: As in Fig. 3.19

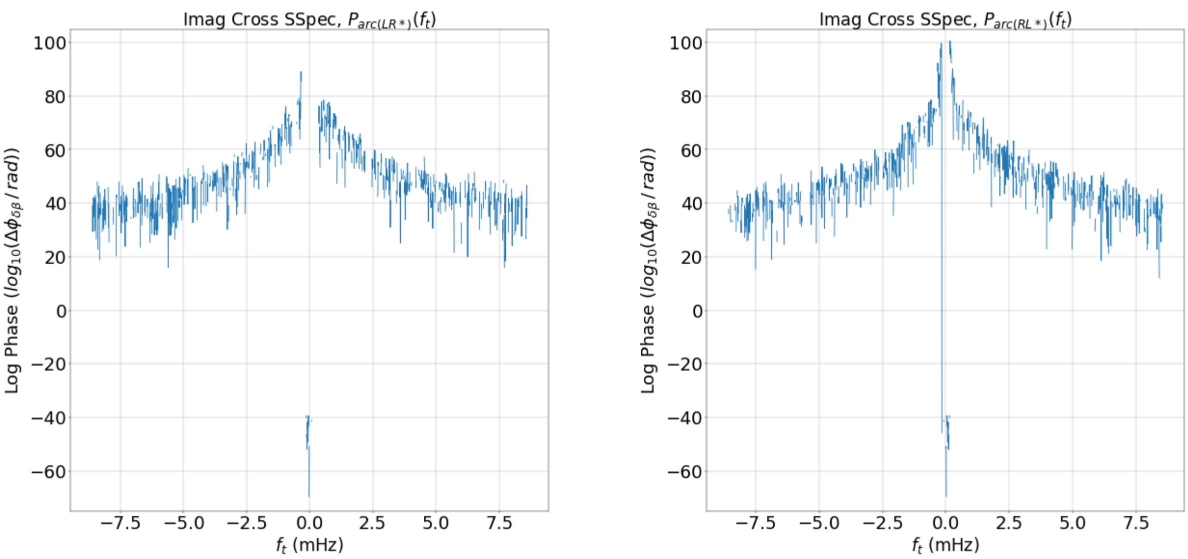


Fig. 3.32: As in Fig. 3.20

| **Run length** | **Average power** | $f_t$ **span (mHz)** | $f_t$ **center (mHz)** | **Classification** |
|---|---|---|---|---|
| 9 | 37.02 | 0.061 | 8.5068 | High $f_\lambda$ and $\|f_t\|$, arc within noise field |
| 10 | 63.84 | 0.0687 | 1.2398 | Inner arc positive $f_t$ |
| 10 | 83.63 | 0.0687 | 0.2632 | Inner arc positive $f_t$ |
| 10 | 69.41 | 0.0687 | -1.0185 | Inner arc negative $f_t$ |
| 11 | 56.64 | 0.0763 | 2.4261 | Inner arc positive $f_t$ |
| 11 | 59.49 | 0.0763 | -1.3275 | Inner arc negative $f_t$ |
| 12 | 54.21 | 0.0839 | 2.3308 | Inner arc positive $f_t$ |
| 12 | 65.14 | 0.0839 | 1.4839 | Inner arc positive $f_t$ |
| 12 | 69.69 | 0.0839 | 0.8736 | Inner arc positive $f_t$ |
| 20 | 71.48 | 0.145 | -0.5913 | Inner arc negative $f_t$ |

Table 3.11: Analysis of 10 longest signal runs from $P_{\text{arc}}(f_t)$ of $P_{\text{Im(RL}^*)}(f_\lambda, f_t)$ secondary cross spectrum. Table column definitions are similar to Table 3.1.

| **RUn length** | **Average power** | $f_t$ **span (mHz)** | $f_t$ **center (mHz)** | **Classification** |
|---|---|---|---|---|
| 8 | 49.19 | 0.0534 | 4.5662 | Inner arc positive $f_t$ |
| 9 | 46.46 | 0.0610 | -5.9662 | Outer arc negative $f_t$ |
| 9 | 62.22 | 0.0610 | -1.5411 | Inner arc negative $f_t$ |
| 9 | 38.07 | 0.0610 | -8.0948 | High $f_\lambda$ and $\|f_t\|$, arc within noise field |
| 10 | 70.42 | 0.0687 | -0.9422 | Inner arc negative $f_t$ |
| 10 | 35.85 | 0.0687 | 9.7313 | High $f_\lambda$ and $\|f_t\|$, arc within noise field |
| 10 | 60.89 | 0.0687 | 1.7357 | Inner arc positive $f_t$ |
| 11 | 54.09 | 0.0763 | -2.1744 | Inner arc negative $f_t$ |
| 12 | 60.03 | 0.0839 | 1.873 | Inner arc positive $f_t$ |
| 13 | 70.91 | 0.0916 | 0.7782 | Inner arc positive $f_t$ |

Table 3.12: Analysis of 10 longest signal runs from $P_{\text{arc}}(f_t)$ of $P_{\text{Im(LR}^*)}(f_\lambda, f_t)$ secondary cross spectrum. Table column definitions are similar to Table 3.1.

# Chapter 4

# Conclusion

In this chapter we interpret and provide commentary on the results and the quality of the data presented in Chapter 3 for each method of analysis aimed at observing the evidence of the effects of birefringent scintillation. We comment on the feasibility of resolving the structure of $\Delta\phi_{LR}$ from the secondary cross spectrum phase. Using a correlation coefficient derived from the normalization of the secondary cross spectrum phase, we set $3\sigma$ upper limits on the strengths of magnetic field fluctuations on small scales. We comment on the physical implications of the magnetic field strength estimates in terms of the configuration of electron densities within the scattering environment. The chapter concludes by considering possible avenues and enhancements that can be considered for future work on the study of birefringent scintillation.

## 4.1 Summary

### 4.1.1 Difference Spectra

#### Dynamic Spectra

A visual inspection of $S_{\text{diff}}(\nu, t)$ reveals very little obvious scintillating structure. The only observable structure are diffuse vertical bands that coincide in time with the bright scintles of the original $S_R(\nu, t)$ and $S_L(\nu, t)$. Some of the diffuse bands appear to dissipate at low frequency possibly indicating modest broadband structure; however, no familiar fringing patterns or drifting maxima and minima across frequency and time are qualitatively visible in $S_{\text{diff}}(\nu, t)$.

We quantify the statistical properties of $S_{\text{diff}}(\nu, t)$ in Table 4.1. From the table we can see that the mean of $S_{\text{diff}}(\nu, t)$ is close to zero. The median verifies this result being even closer to zero. A mean of zero shows little systematic offset between $S_R(\nu, t)$ and $S_L(\nu, t)$ as a result of poor polarimetric calibration. The standard deviation of all $S_{\text{diff}}(\nu, t)$ indicate that the mean of the data is consistent with 0 for all observation days as they are bounded within the error. These characteristics are consistent for all six days except for 2019-12-29 having a higher mean and standard deviation most likely as a result of polarimetric calibration error. We calculate the percentage of difference between $S_R(\nu, t)$ and $S_L(\nu, t)$ with equation 2.14 from which we quantify no detectable signal above the 0.01 $\%$ level in any of the difference spectra, except for 2019-12-29, where the significance rises to 0.2 $\%$, in the last *dynspec* sub-integration.

The fluctuations of intensity seen in the last sub-integration of 2019-12-29 beginning at $t$ = 480 minutes is most likely a result of differential phase calibration error. This conclusion is arrived at due to the sharp transitional nature of the effect. The apparent scintillating effect caused by the instrumental calibration error highlights the importance of accurate polarimetric calibration.

| Obs. Date | Mean | Median | Standard deviation |
|---|---|---|---|
| 2019-12-26 | 0.00027 | 0.00017 | 0.00240 |
| 2019-12-27 | 0.00043 | 0.00023 | 0.00281 |
| 2019-12-28 | 0.00035 | 0.00018 | 0.00252 |
| 2019-12-29 | 0.01209 | 0.00057 | 0.09717 |
| 2019-12-30 | -0.00033 | -0.00008 | 0.00432 |
| 2019-12-31 | -0.00039 | -0.00014 | 0.00367 |

Table 4.1: Noise statistics of differential dynamic spectrum, $S_{\text{diff}}(\nu, t)$.

From the the visualization of $S_{\text{diff}}(\nu, t)$ we can observe variations of gain in the frequency domain marked by sharp spectral transitions between sub-integrations at *t* = 240 minutes and *t* = 480 minutes. 2019-12-28 and 2019-12-29 observations aside (due to instrumental calibration and FITSIO errors), this is most noticeable in the observations made on 2019-12-30 and 2019-12-31. Noting that MeerKAT was phased only once at the start of observations made on 2019-12-26 and 2019-12-27, and that the array was rephased every two hours on 2019-12-30 and 2019-12-31, we conclude that the observed gain variations are most likely caused by the array phasing and beam forming processes. The array phasing process could have also been the source of the errors encountered on the 2019-12-28 and 2019-12-29 observations. We are able to establish a qualitative hierarchy not based on an objective metric of the calibrated data analyzed in this work with calibrated spectra of 2019-12-26 and 2019-12-27 being the most reliable, the data of 2019-12-30 and 2019-12-31 being less reliable, and the data of 2019-12-28 and 2019-12-29 of the least reliable quality for *dynspecs* of integrations of $t \geq 11$ hours. Alternatively, performing analysis on the shorter, 3-hour sub-integrations of 2019-12-30 and 2019-12-31 may surmount the issues of frequency gain variations but limit the resolution of their secondary spectra.

**Differential Secondary Spectra**

Visual inspection of $P_{S_{\text{diff}}}(f_\lambda, f_t)$, reveals an empty field of noise except on 2019-12-29 where a parabolic arc is seen. Diagonally aligned signal artefacts reminiscent of Fig. 3 (c) of Cordes et al. (2006) are present in most of the spectra. The diagonal artefacts are a possible result of $\lambda$-step sampling of the *dynspec*. Sampling $P_{S_{\text{diff}}}(f_\lambda, f_t)$ with the average curvature fit of $P_{LL^*}$ and $P_{RR^*}$ reveals a mostly flat distribution of power of the order of the noise floor except near the origin where residual power from pre-whitening and post-darkening exist. RFI also contributes power at low $f_\lambda$ seen as vertical stripes in the secondary spectrum. Fitting a spline through the sampled $P_{S_{\text{diff}}}(f_t)$ data with the regions near $f_t$ = 0 filtered should reveal a flat horizontal linear relationship across $f_t$ compared to inclined and triangular line fit for $P_{LL^*}(f_t)$ and $P_{RR^*}(f_t)$.

### 4.1.2 Cross Spectra Evaluation

We are able to successfully resolve $\Delta\phi_{\delta\beta}$ where $\Delta\phi_{\delta\beta} = \phi_R - \phi_L$, as a function of $f_\lambda$ and $f_t$ from $P_{\text{Im}(RL^*)}$ as shown in Fig. 3.19 - Fig. 3.29. Qualitatively, $P_{\text{Im}(RL^*)}$ reveals visible parabolic arcs. However, the arcs appear fainter and more diffuse than their $P_{\text{Re}(RL^*)}$, $P_{RR^*}$, and $P_{LL^*}$ counterparts. The strongest arc is seen in 2019-12-29 again due to phase calibration error. Most of the $P_{\text{Im}(RL^*)}$ parabola are upper bounded by $f_\lambda \approx$ 3000 m$^{-1}$ where the parabola dissipate. This corresponds to a delay of $\tau \approx 1.035$ $\mu$s.

For $\Delta\phi_{\delta\beta}$ from birefringence, a smoothly varying continuous signal is expected. Sampling $P_{\text{Im}(RL^*)}$ along its parabola, it is seen that $\Delta\phi_{\delta\beta}$ varies quickly in the outer regions of the sampled arc with phase variations slowing down as $|f_t| \to 0$, as the location of most sampled signal runs fall within the inner arc region of -5 < $|f_t|$ < 5 mHz (seen in Tables 3.1 - 3.12). The location of a signal run is defined as the midpoint between the first and last sample of the signal on the $f_t$ axis. 81 out of 120 of the longest signal runs are bounded within this region. However, we comment a word of caution as the inner arc cutoff of $f_t$ = 5 mHz (corresponding to delays $\tau \approx 0.42\,\mu$s) is arbitrarily chosen. The predominantly stochastic variations of $\Delta\phi_{\delta\beta}$ lead us to conclude that the phase variations originate from the self-noise intrinsic to PSR J0437-4715. In the limit of a strong source, noise in synthesis images of an interferometer can be dominated by noise fluctuations of the source power (Kulkarni, 1989). As the flux desnisty of J0437-4715 approaches and exceeds the low SEFD of MeerKAT, self-noise (dominated by the pulse jitter noise of the pulsar) correlated over the wide bandwidth of the spectra is significant and sets a fundamental limit for observations (Osłowski et al., 2011). Characterization of the distribution of noise in the presence of signal in the high S/N regime for the cross power spectrum of a scintillating source is provided in Gwinn et al. (2012) which provides a template for further study. The measured $\Delta\phi_{\delta\beta}$ signal is dominated by jitter and is difficult to distinguish from the intrinsic jitter noise of the pulsar. In regards to this, the wide bandwidth and the high gain of the L-band of MeerKAT works against us. Longer integration times may surmount this problem. We propose as a follow up to examine the cross spectra of all six days of separately appended $S_L(\nu, t)$ and $S_R(\nu, t)$ with the gaps filled with linear interpolation. From the apparent phase variations, we can conclude that $\Delta\phi_{\delta\beta}$ is very small such that it is smaller than the jitter noise limit intrinsic to the emission of J0437-4715. Because of this we fail to reject the null hypothesis posed in section 2.4 and conclude that $S_R(\nu, t)$ and $S_L(\nu, t)$ are highly correlated for all observations unaffected by calibration error.

Large signal power at $f_t$ < $0.5$ mHz near the origin are visually identified in the arc sampled phase of the secondary cross spectrum. We attribute these lump like features (seen in Fig. 3.20 - 3.30) adjacent to the regions affected by pre-whitening and post-darkening as the effect of ringing from the FFT. Although our original expectation for $\Delta\phi_{\delta\beta}$ to vary smoothly within the range $-5 < f_t < 5$ mHz was somewhat verified, a significant smoothly varying signal at such low $f_t$ could also be interpreted as having originated from scattering by large scale structures.

### 4.1.3 Upper Limits on Turbulent Magnetic Fields

The standard deviation of the spatial fluctuations of the magnetoionic field $\delta\beta_z$, in units of $\mu$G cm$^{-3}$ as a function of the transverse Fresnel scale $r_F$, can be calculated from equation (33) of Simonetti et al. (1984):

$$\langle\delta\beta_z^2(r_F)\rangle^{1/2} \approx 157[1 - \hat{\Gamma}_{RL}]^{1/2}\left(\frac{\nu}{430\,\mathrm{MHz}}\right)^2\left(\frac{D}{1\,\mathrm{kpc}}\right)^{-1/2}\left(\frac{r_F}{10^{11}\,\mathrm{cm}}\right)^{-1/2}\mu\mathrm{G\,cm}^{-3} \quad (4.1)$$

$\delta\beta_z$ is a spatially fluctuating component of the birefringent medium owing to fluctuations in both free electron density and the projection of small scale magnetic fields along the line of sight; $\delta\beta_z = n_e\delta B_z + B_z\delta n_e$. For eq. 4.1, $\nu$ = 1284 MHz for the L-band center frequency of MeerKAT and $D$ = 0.154 kpc for PSR J0437-4715. $r_F$ can be calculated as $r_F = \sqrt{\lambda\left(\frac{D_s}{D}\right)(D - D_s)} = 4.2 \times 10^{10}$ cm for $\lambda$ = 23 cm, $D$ = 154 pc, and $D_s$ = 32 pc. Authors such as Smirnova et al. (2006) have also quoted $r_F$ values of $2 \times 10^{10}$ cm and $1 \times 10^{11}$ cm towards J0437-4715. $\hat{\Gamma}_{RL}$ is a correlation coefficient that decays with the variance of differential phase.

$$\hat{\Gamma}_{RL} = 1 - \langle\Delta\phi_{\delta\beta}^2\rangle \quad (4.2)$$

We can calculate $\langle\Delta\phi_{\delta\beta}^2\rangle$ from the dataset by taking a normalization of the the secondary cross spectrum phase.

$$\langle\Delta\phi_{\delta\beta}^2\rangle = \mathrm{var}\left[\frac{\tilde{S}_{\mathrm{Im}(RL^*)}}{\sqrt{\tilde{S}_{LL^*}\tilde{S}_{RR^*}}}\right] \quad (4.3)$$

where $\langle\Delta\phi_{\delta\beta}^2\rangle$ is measured from the parabola of the normalized secondary cross spectrum phase. $\tilde{S}_{\mathrm{Im}(RL^*)}$ is the imaginary part of the secondary cross spectrum, and $\tilde{S}_{LL^*}$ and $\tilde{S}_{RR^*}$ are LCP and RCP secondary spectra. Sampling along the parabola recovers a positive and negative valued signal with a mean approaching zero as shown in Fig. 4.1.

A smaller $\langle \Delta\phi^2_{\delta\beta} \rangle$ allows us to place more stringent limits on $\langle \delta\beta^2_z(r_F) \rangle^{1/2}$ spatial fluctuations. All preprocessing steps are employed except pre-whitening and post-darkening and computing the logarithm of $\tilde{S}_{\mathrm{Im}(RL^*)}$, $\tilde{S}_{RR^*}$, and $\tilde{S}_{LL^*}$.

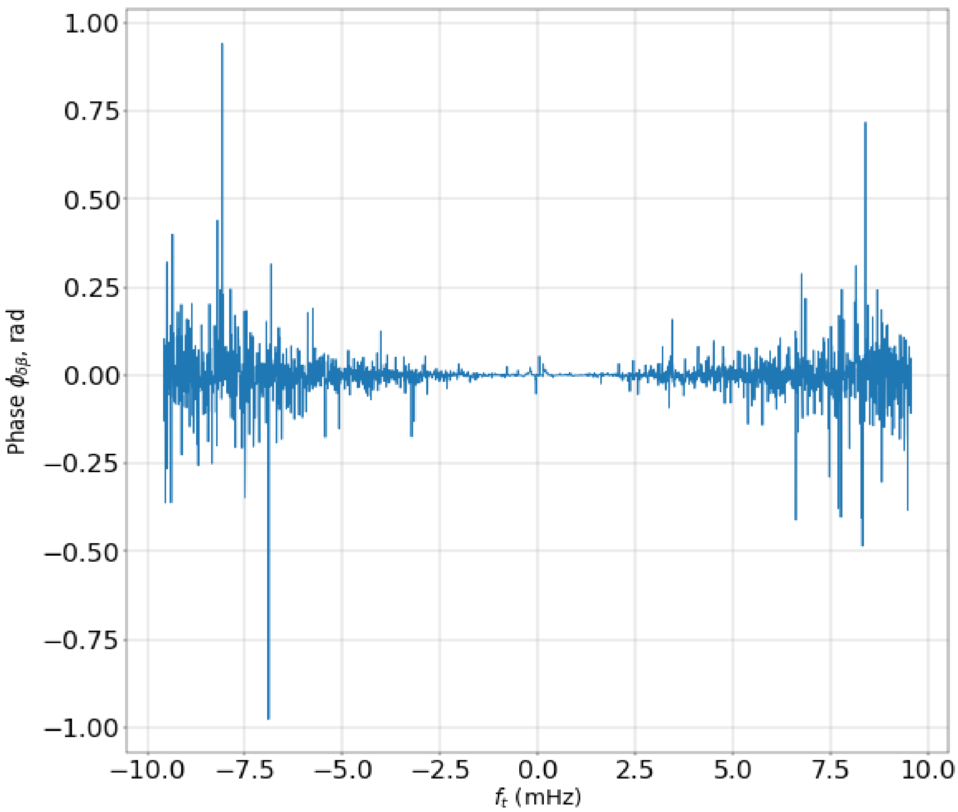


Fig. 4.1: Result of sampling the normalized secondary cross spectrum phase along the parabolic arc. The result varies between -1 and 1 with a mean approaching 0. The variance $\langle \Delta\phi^2_{\delta\beta} \rangle$ is smaller as $|f_t| \to 0$ and larger when moving away from 0. We compute $\langle \Delta\phi^2_{\delta\beta} \rangle$ for different ranges of $f_t$ within the inner arc and and the outer arc with the limit of 5 mHz. The limit of 5 mHz is arbitrary and can affect the final estimate of $\langle \delta\beta^2_z \rangle^{1/2}$. Including more samples in the estimate of $\langle \Delta\phi^2_{\delta\beta} \rangle$ helps to reduce uncertainty. This can be done by averaging the samples and taking $\langle \Delta\phi^2_{\delta\beta} \rangle$ for longer intervals.

Tables C.1, C.2, and C.3 in Appendix C show the upper limits of $\delta\beta_z$ by inserting $\langle \Delta\phi^2_{\delta\beta} \rangle$ from different ranges of $f_t$ where the normalised phase varies quickly (outer arc) and slowly (inner arc) and for $-f_t$ and $f_t$ into eq. 4.2 and applying the resulting $\hat{\Gamma}_{RL}$ to eq. 4.1. Due to subtraction, we are effectively left with standard deviation of $\Delta\phi_{\delta\beta}$ as the second term of eq. 4.1 which is multiplied by 3 for $3\sigma$ confidence.

From the tables of Appendix C the best upper limits of spatial fluctuations of the magnetoionic field within the scattering region probed by the primary forward arc are derived from the data of 2019-12-26, 2019-12-27, and 2019-12-28. There is an order of magnitude of difference between upper limits of $\langle \delta\beta_z^2 \rangle^{1/2}$ for $\langle \Delta\phi_{\delta\beta}^2 \rangle$ taken from the inner arc versus the outer arc. The upper limits derived from 2019-12-26 and 2019-12-27 verifies our original assumption of the quality of the data from those epochs. The limits derived for 2019-12-28 are a surprise because of the missing 4 hour sub-integration in the interim filled in with linear interpolation for the observation. However, this result indicates the viability of further studies to estimate $\langle \delta\beta_z^2 \rangle^{1/2}$ from data of shorter integration lengths. The weakest upper limits of $\langle \delta\beta_z^2 \rangle^{1/2}$ in the scattering region are from 2019-12-29 where $\langle \Delta\phi_{\delta\beta}^2 \rangle$ along the entire arc is large originating from instrumental calibration error. Summing and averaging the samples of normalized phase for all observations unaffected by calibration error produces an upper limit of $\delta\beta_z \leq 305$ $\mu$G cm$^{-3}$ for $\langle \Delta\phi_{\delta\beta} \rangle = 0.01749$ measured from an arc region of $-5 < f_t < 5$ mHz. We set the upper limit of $\delta\beta_z$ fluctuations interpreted in the next section as $\delta\beta_z \leq 302$ $\mu$G cm$^{-3}$.

The estimate for $\delta\beta_z$ made by Simonetti et al. (1984) only accounts for spatial fluctuations in either $n_e$ or $B_z$ to avoid separating $\delta\beta_z$ into contributions from $\delta n_e$ and $\delta B_z$ because such separations requires additional information about their correlations. For a spatially uniform medium with unchanging electron density in the scattering screen, $\langle n_e \rangle = \frac{\mathrm{DM}}{D} = \frac{2.64\,\mathrm{pc\,cm^{-3}}}{154\,\mathrm{pc}} = 0.017$ cm$^{-3}$ and the upper limit of small scale magnetic field fluctuations along the LoS is $\langle \delta B_z^2 (1 \times 10^{11}\,\mathrm{cm}) \rangle^{1/2} \leq 17.7$ mG. If the same $\delta\beta_z$ occur in a spatially uniform medium with $\langle n_e \rangle = 0.2$ and filling factor $f \sim 0.1$ - $0.2$ (McKee and Ostriker, 1977), the upper limit is $\langle \delta B_z^2 (1 \times 10^{11}\,\mathrm{cm}) \rangle^{1/2} \leq 1.6$ mG. Likewise, with knowledge of $\delta\beta_z$ and a probable value for uniform $B_z$ on small scales as $B_z \approx 4\,\mu$G (Han, 2017), we can place upper limits on the fluctuations of $n_e$ as $\langle \delta n_e^2 (1 \times 10^{11}\,\mathrm{cm}) \rangle^{1/2}$ $\leq 75.5$ cm$^{-3}$ which is less than two orders of magnitude of an observed over-density ($n_e \geq 100$ cm$^{-3}$) within the IISM (Hill et al., 2005).

Based on present literature of interstellar magnetic fields such as Beck (2007), Beck and Wielebinski (2013), and the original work of Simonetti et al. (1984), our computed upper limits of magnetic field variations are uninformative as the expected constraints on the amplitude of interstellar magnetic fields on turbulent scales should be on the order of a few $\mu$G not tens of mG! However, if we use the same $\hat{\Gamma}_{RL}$ from calculating the upper limit of 302 $\mu$G cm$^{-3}$ and assume the same observing conditions of Simonetti et al. (1984) with the constants ($\nu$ = 430 MHz, $D$ = 1.8 kpc, and $r_F = 6 \times 10^{11}$ cm), we acquire an upper limit of spatial fluctuations of $\langle \delta\beta_z^2(6 \times 10^{11}\,\text{cm})\rangle^{1/2} \leq 2.42$ $\mu$G cm$^{-3}$ which is lower than the original work's base constraint of $\delta\beta_z \leq 3.6$ $\mu$G cm$^{-3}$ at $3\sigma$. Making the same assumptions as the previous paragraph but for a spatially uniform medium of $\langle n_e\rangle = 0.03$ cm$^{-3}$ , $\langle n_e\rangle = 0.2$ cm$^{-3}$, and a uniform magnetic field of $B_z \approx 4\mu$G we would observe $\delta B_z \leq 70.6$ and 10.5 $\mu$G, and $\delta n_e \leq 0.6$ cm$^{-3}$ within the scattering region towards PSR 1737+13. These values are more reasonable. Distance to the pulsar and observing frequency therefore play an important role in determining the upper limit and should be considered in future studies. The distance to the scattering screen also impacts the upper limit by the way of the Fresnel scale with a scattering screen closer to the pulsar putting more stringent limits on $\delta\beta_z$. Observations of more pulsars along a multitude of LoS will allow us to improve measurements of fine scale turbulence as we would gain further information regarding the spatial correlations between $\delta n_e$ and $\delta B_z$ thus allowing for the refinement of $\delta\beta_z$ upper limits. Such studies could follow in the practice of Ohno and Shibata (1993) by observing pulsars pairs with small angular separation with similar DMs and different RMs.

## 4.2 Future Works

We now discuss what areas could have been improved upon in this work. From the perspective of current instrumentation, the RFI mitigation scheme could be improved upon. Solutions like MeerGuard (Reardon, 2019) may yield better quality dynamic spectra and secondary spectra. Fine tuning the $q$ parameter of CLFD to find a threshold that optimally mitigates RFI bursts without zapping the low frequency bins of the dynamic spectrum can also be considered.

The currently employed arc sampling method to view power distribution along the parabola was developed ad hoc from scratch. We presently sample the raw values of $P(f_\lambda, f_t)$ along a parabola of a known $\eta$. This is neither the only way nor may it be the best way of studying the power distribution of the secondary spectrum. The normalized secondary spectrum $P(f_\lambda, \frac{f_t}{f_{\text{arc}}})$, as derived in Reardon et al. (2020) is created by re-sampling the secondary spectrum in $f_t$ with the sampling of each row adjusted with linear interpolation provides an alternative approach to study the arc power distribution. Each arc is transformed into vertical lines of power with the primary arc located at $\frac{f_t}{f_{\text{arc}}} = f_{tn} = \pm 1$. The $f_{tn}$ axis is the fractional distance from the $f_t = 0$ axis to the arc at $f_{\text{arc}}$ for a given $f_\lambda$. Averaging the normalised spectrum in $f_\lambda$ with appropriate weighting produces the Doppler profile $D_t(f_{tn})$, that is useful for analyzing anisotropy and characterising how power falls off from the primary arc. Averaging the normalised spectrum in Doppler obtains the delay profile $D_\lambda(f_\lambda)$, that follows the phase spectrum in weak scintillation where the secondary spectrum can be written in terms of the spatial spectrum of phase shifts the waves experience when traversing the scattering region. We have computed an example of these 3 products with the absolute value of the phase of the secondary cross spectrum, $P_{|\text{Im}(RL^*)|}(f_\lambda, f_t)$, for the data of 2019-12-27 and are displayed in Fig. 4.2, however, we leave for future work their interpretation and application on the remaining data.

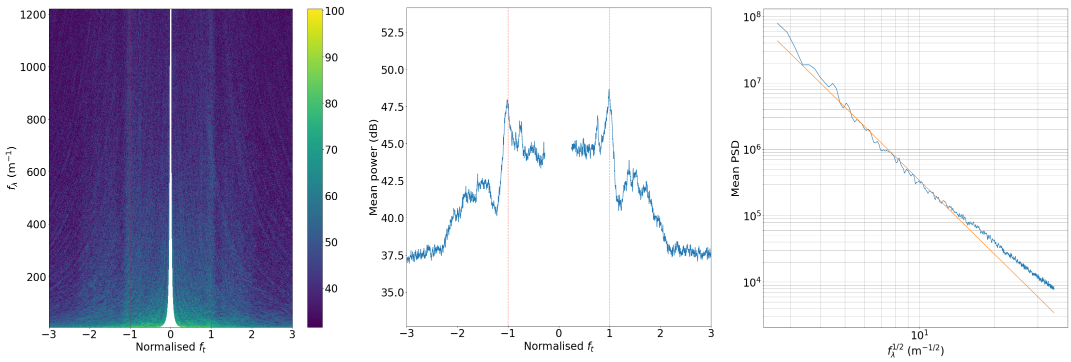

Fig. 4.2: The normalized secondary cross spectrum $P_{|\text{Im}(RL^*)|}(f_\lambda, f_{tn})$ (left). The Doppler profile $D_t(f_{tn})$ (center) gives the strength of scintillation and visualizes anisotropy. The Delay profile $D_\lambda(f_\lambda)$ (right) follows a power law scaling with the exponent $\frac{\alpha}{2} - 1$ where $\alpha$ is the spectral exponent of turbulence. The Delay profile is scaled by $f_\lambda^{1/2}$ and plotted versus $f_\lambda^{1/2}$. These approaches can provide further insight into the power distribution of the secondary cross spectrum and the nature of $\Delta\phi_{\delta\beta}$ variations, however, more work needs to be done in adjusting their compatibility with a non-logarithmic and non-absolute form of the secondary cross spectrum.

The phase of the secondary cross spectrum from Brisken et al. (2010) is not visualized on a logarithmic scale which works best when noise is log-normally distributed (Reardon, 2018). For display purposes, the phase is smoothed over with a 3 pixel in $f_t$ and 5 pixel in $\tau$ averaging of the complex product prior to taking the real or imaginary part. The phase spectrum is therefore $\Delta\phi_{\delta\beta}(\tau, f_t) = \arg(\langle C_{RL^*}(\tau, f_t)\rangle)$, where the angle brackets denote a $3 \times 5$ averaging that weights the complex product before taking the argument. The size of the averaging window needs to be adjusted for the spatial frequency domain if we persist in analyzing the secondary spectrum in $f_\lambda$.

The data we have acquired represent signal runs of when the phase of either $RL^*$ or $LR^*$ is positive valued along the parabola. A runs test of independence (Croarkin, 2013) can be used to verify whether the sequence of signal runs along the parabola is random or whether there is organised structure. The runs test statistic is $Z = \frac{R-\mu_R}{\sigma_R}$ where $R$ is the observed number of signal runs, $\mu_R = \frac{n_1 n_2}{n_1+n_2} + 1$ is the mean, $\sigma_R^2 = \frac{(\mu_R-1)(\mu_R-2)}{(n_1+n_2)-1}$ is the variance of runs, and $n_1$ and $n_2$ are the number of instances where the phase of $LR^*$ or $RL^*$ is positive. For a large sample size and a significance of $5\%$, a critical value of

$|Z| > 1.96$ indicates non-randomness and structure within the signal runs. We propose carrying out the runs test separately for the inner and outer regions of the arc.

Reaching out for more novel instrumentation, cyclic spectroscopy can be used to form the cyclic dynamic cross spectrum and secondary cross spectrum (Walker et al., 2013). The cyclic spectrum is the complex product of the lower sideband of the pulsar baseband signal with the complex conjugate of the upper sideband:

$$S_E(\nu, a_k) = \langle E(\nu + \frac{a_k}{2}) E^*(\nu - \frac{a_k}{2}) \rangle \tag{4.4}$$

where $\nu$ is radio frequency and $a_k$ is modulation frequency. The cyclic spectrum encapsulates phase information from IISM scattering as part of a filtered response $H(\nu)$ where we can expect to study $\delta\phi_{\delta\beta}$:

$$S_E(\nu, a_k) = \langle H(\nu + \frac{a_k}{2}) H^*(\nu - \frac{a_k}{2}) \rangle S_x(\nu, a_k) \tag{4.5}$$

$S_x(\nu, a_k)$ is the FFT of the intrinsic pulse unaffected by propagation effects. The cyclic spectrum is calculated across narrow bandwidths where there is little assumed change of the pulse profiles of $S_x(\nu, a_k)$ with frequency. Eq. 4.5 shows that $H(\nu)$ can in principle be separated from $S_x$, however, the separation is non-trivial because of degeneracies within the cyclic spectrum model. Generating the cyclic spectrum can be done with software such as DSPSR (van Straten and Bailes, 2011).

As mentioned by Simonetti et al. (1984), better limits can be measured with lower frequencies and more distant pulsars. Lower frequencies are accessible with the UHF-band of MeerKAT ($\nu_{\rm BW} = 544$, MHz and $\nu_{\rm obs} = 816$ MHz) (Bailes et al., 2020) or other radio telescopes, such as the MWA ($\nu_{\rm BW} = 30$ MHz, and $\nu_{\rm obs} = 192$ MHz) (Bhat et al., 2016; Tingay et al., 2013), and LOFAR (Stappers et al., 2007). Other pulsars can be considered for observation however, the distance should be kept within 1 - 2 kpc to maintain the Local Bubble as the scattering screen.

# References

B. P. Abbott et al. GW151226: Observation of Gravitational Waves from a 22-Solar-Mass Binary Black Hole Coalescence. *Physical Review Letters*, 116(24):241103, June 2016. doi:10.1103/PhysRevLett.116.241103.

B. P. Abbott et al. Observation of gravitational waves from a binary black hole merger. *Phys. Rev. Lett.*, 116:061102, Feb 2016. doi:10.1103/PhysRevLett.116.061102.

B. P. Abbott et al. Gwtc-1: A gravitational-wave transient catalog of compact binary mergers observed by ligo and virgo during the first and second observing runs. *Physical Review X*, 9(3), Sep 2019. doi:10.1103/physrevx.9.031040.

J. W. Armstrong, B. J. Rickett, and S. R. Spangler. Electron Density Power Spectrum in the Local Interstellar Medium. *Astrophysical Journal Letters*, 443:209, April 1995. doi:10.1086/175515.

W. Baade and F. Zwicky. Cosmic rays from super-novae. *Proceedings of the National Academy of Science*, pages 259–263, May 1934. doi:10.1073/pnas.20.5.259.

M. Bailes et al. MeerTime - the MeerKAT Key Science Program on Pulsar Timing. In *MeerKAT Science: On the Pathway to the SKA*, page 11, January 2016.

M. Bailes et al. The meerkat telescope as a pulsar facility: System verification and early science results from meertime. *Publications of the Astronomical Society of Australia*, 37, 2020. doi:10.1017/pasa.2020.19.

R. Beck. Galactic magnetic fields. *Scholarpedia*, 2(8):2411, 2007. doi:10.4249/scholarpedia.2411. revision 193987.

R. Beck, A. Shukurov, D. Sokoloff, and R. Wielebinski. Systematic bias in interstellar magnetic field estimates. *Astronomy & Astrophysics*, 411(2):99–107, Nov 2003. doi:10.1051/0004-6361:20031101.

Rainer Beck and Richard Wielebinski. Magnetic fields in galaxies. *Planets, Stars and Stellar Systems*, page 641–723, 2013. doi:10.1007/978-94-007-5612-0_13.

Werner Becker, Michael Kramer, and Alberto Sesana. Pulsar timing and its application for navigation and gravitational wave detection. *Space Science Reviews*, 214, 01 2018. doi:10.1007/s11214-017-0459-0.

N. D. R. Bhat, S. M. Ord, S. E. Tremblay, S. J. McSweeney, and S. J. Tingay. Scintillation arcs in low-frequency observations of the timing-array millisecond pulsar psr j0437–4715. *The Astrophysical Journal*, 818(1):86, Feb 2016. doi:10.3847/0004-637x/818/1/86.

N. D. Ramesh Bhat, Yashwant Gupta, and A. Pramesh Rao. Pulsar Scintillation and the Local Bubble. *ApJ*, 500(1):262–279, June 1998. doi:10.1086/305715.

N. D. Ramesh Bhat, Yashwant Gupta, A. Pramesh Rao, and P. B. Preethi. Pulsar scintillation studies and structure of the local interstellar medium. *International Astronomical Union Colloquium*, 177:545–548, 2000. doi:10.1017/S0252921100060565.

D. Bhattacharya. The Interstellar Medium. Lecture notes, Inter University Centre for Astronomy and Astrophysics, Pune 411007, India, 2003. URL: http://www.iucaa.in/ dipankar/ph217/ism.pdf.

D. Bhattacharya and E. P. J. van den Heuvel. Formation and evolution of binary and millisecond radio pulsars. *Physics Reports*, 203(1-2):1–124, January 1991. doi:10.1016/0370-1573(91)90064-S.

G. S. Bisnovatyi-Kogan and B. V. Komberg. Pulsars and close binary systems. *Soviet Astronomy*, 18:217, October 1974.

P. Bolli et al. An international survey of front-end receivers and observing performance of telescopes for radio astronomy. *Publications of the Astronomical Society of the*

*Pacific*, 131(1002):085002, jul 2019. doi:10.1088/1538-3873/ab1f7e.

W. F. Brisken, J.-P. Macquart, J. J. Gao, B. J. Rickett, W. A. Coles, A. T. Deller, S. J. Tingay, and C. J. West. 100 uas resolution vlbi imaging of anisotropic interstellar scattering toward pulsar b0834+06. *The Astrophysical Journal*, 708(1):232–243, Dec 2010. doi:10.1088/0004-637x/708/1/232.

M. Burgay et al. An increased estimate of the merger rate of double neutron stars from observations of a highly relativistic system. *Nature*, 426(6966):531–533, Dec 2003. doi:10.1038/nature02124.

Adam Burrows. Neutron stars: How pulsars get their spins. *Nature*, 393(6681):121–122, May 1998. doi:10.1038/30108.

S. Chandrasekhar. The Maximum Mass of Ideal White Dwarfs. *ApJ*, 74:81, July 1931. doi:10.1086/143324.

A. Chepurnov and A. Lazarian. Extending the Big Power Law in the Sky with Turbulence Spectra from Wisconsin H$\alpha$ Mapper Data. *Astrophysical Journal Letters*, 710 (1):853–858, February 2010. doi:10.1088/0004-637X/710/1/853.

Ismaël Cognard and J. Lestrade. Dispersion measure variations observed in the direction of the millisecond pulsar psr b1821-24. *Astronomy and Astrophysics*, 323:211–216, 06 1997.

W. Coles, G. Hobbs, D. J. Champion, R. N. Manchester, and J. P. W. Verbiest. Pulsar timing analysis in the presence of correlated noise. *Monthly Notices of the Royal Astronomical Society*, 418(1):561–570, 11 2011. doi:10.1111/j.1365-2966.2011.19505.x.

James J. Condon and Scott M. Ransom. *Essential Radio Astronomy*. Princeton University Press, 2016.

J. M. Cordes. NE2001: A New Model for the Galactic Electron Density and its Fluctuations. In Dan Clemens, Ronak Shah, and Teresa Brainerd, editors, *Milky Way Surveys: The Structure and Evolution of our Galaxy*, volume 317 of *Astronomical Society of the Pacific Conference Series*, page 211, December 2004.

J. M. Cordes and B. J. Rickett. Diffractive interstellar scintillation timescales and velocities. *The Astrophysical Journal*, 507(2):846–860, nov 1998. doi:10.1086/306358.

J. M. Cordes and A. Wolszczan. Multiple Imaging of Pulsars by Refraction in the Interstellar Medium. *The Astrophysical Journal Letters*, 307:L27, August 1986. doi:10.1086/184722.

James M. Cordes. Pulsar Observations I. – Propagation Effects, Searching Distance Estimates, Scintillations and VLBI. In Snezana Stanimirovic, Daniel Altschuler, Paul Goldsmith, and Chris Salter, editors, *Single-Dish Radio Astronomy: Techniques and Applications*, volume 278 of *Astronomical Society of the Pacific Conference Series*, pages 227–250, December 2002.

James M. Cordes, T. Joseph W. Lazio, and Carl Sagan. Scintillation-induced intermittency in SETI. *The Astrophysical Journal*, 487(2):782–808, oct 1997. doi:10.1086/304620.

James M. Cordes, Barney J. Rickett, Daniel R. Stinebring, and William A. Coles. Theory of parabolic arcs in interstellar scintillation spectra. *The Astrophysical Journal*, 637 (1):346–365, jan 2006. doi:10.1086/498332.

Donald P. Cox and Ronald J. Reynolds. The local interstellar medium. *Annual Reviews in Astronomy and Astrophysics*, 25:303–344, January 1987. doi:10.1146/annurev.aa.25.090187.001511.

Carroll Croarkin. Runs test for detecting non-randomness. `https://www.itl.nist.gov/div898/handbook/eda/section3/eda35d.htm`, 2013.

X. P. Deng, G. Hobbs, X. P. You, M. T. Li, M. J. Keith, R. M. Shannon, W. Coles, R. N. Manchester, J. H. Zheng, X. Z. Yu, D. Gao, X. Wu, and D. Chen. Interplanetary spacecraft navigation using pulsars. *Advances in Space Research*, 52(9):1602–1621, November 2013. doi:10.1016/j.asr.2013.07.025.

Timothy Dolch, Dan R. Stinebring, Glenn Jones, Hengrui Zhu, Ryan S. Lynch, Tyler Cohen, Paul B. Demorest, Michael T. Lam, Lina Levin, Maura A. McLaughlin, and Nipuni T. Palliyaguru. Deconvolving Pulsar Signals with Cyclic Spectroscopy: A Systematic Evaluation. *The Astrophysical Journal*, 913(2):98, June 2021. doi:10.3847/1538-4357/abf48b.

R. T. Edwards, G. B. Hobbs, and R. N. Manchester. TEMPO2, a new pulsar timing package - II. The timing model and precision estimates. *Monthly Notices of the Royal Astronomical Society*, 372(4):1549–1574, November 2006. doi:10.1111/j.1365-2966.2006.10870.x.

Albert Einstein. Approximative Integration of the Field Equations of Gravitation. *Sitzungsber. Preuss. Akad. Wiss. Berlin (Math. Phys. )*, 1916:688–696, 1916.

D. Emmanoulopoulos, I. M. McHardy, and P. Uttley. On the use of structure functions to study blazar variability: caveats and problems. *Monthly Notices of the Royal Astronomical Society*, 404(2):931–946, 05 2010. doi:10.1111/j.1365-2966.2010.16328.x.

R. A. Fallows et al. Broadband meter-wavelength observations of ionospheric scintillation. *Journal of Geophysical Research: Space Physics*, 119(12):10,544–10,560, 2014. doi:https://doi.org/10.1002/2014JA020406.

R. D. Ferdman et al. Asymmetric mass ratios for bright double neutron-star mergers. *Nature*, 583(7815):211–214, Jul 2020. doi:10.1038/s41586-020-2439-x.

Elizabeth Ferrara. Galactic millisecond pulsars. `http://astro.phys.wvu.edu/GalacticMSPs/`, 2021.

R. L. Fiedler, B. Dennison, K. J. Johnston, and A. Hewish. Extreme scattering events caused by compact structures in the interstellar medium. *Nature*, 326(6114):675–678, April 1987. doi:10.1038/326675a0.

G. D. Fleishman, Q. J. Fu, M. Wang, G.-L. Huang, and V. F. Melnikov. Birefringence effect as a tool for astrophysical plasma study. *Phys. Rev. Lett.*, 88:251101, Jun 2002. doi:10.1103/PhysRevLett.88.251101.

R. S. Foster and D. C. Backer. Constructing a Pulsar Timing Array. *ApJ*, 361:300, September 1990. doi:10.1086/169195.

A Fruchter. The bow shock of the nearest millisecond pulsar, 1995.

M. Geyer, A. Karastergiou, V. I. Kondratiev, K. Zagkouris, M. Kramer, B. W. Stappers, J.-M. Grießmeier, J. W. T. Hessels, D. Michilli, M. Pilia, and C. Sobey. Scattering analysis of LOFAR pulsar observations. *Monthly Notices of the Royal Astronomical Society*, 470(3):2659–2679, 05 2017. doi:10.1093/mnras/stx1151.

Marisa Geyer. *Pulsar scattering and the ionized interstellar medium*. PhD thesis, University of Oxford, 2017.

T. Gold. Rotating Neutron Stars as the Origin of the Pulsating Radio Sources. *Nature*, 218(5143):731–732, May 1968. doi:10.1038/218731a0.

Peter Goldreich and William H. Julian. Pulsar Electrodynamics. *ApJ*, 157:869, August 1969. doi:10.1086/150119.

D. M. Gould and A. G. Lyne. Multifrequency polarimetry of 300 radio pulsars. *Monthly Notices of the Royal Astronomical Society*, 301(1):235–260, November 1998. doi:10.1046/j.1365-8711.1998.02018.x.

Yashwant Gupta. *Pulsar Scintillation: Overview and Some Recent Results*, pages 25–30. Springer Netherlands, Dordrecht, 2001. ISBN 978-94-010-1001-6. doi:10.1007/978-94-010-1001-6_4.

C. R. Gwinn, M. C. Britton, J. E. Reynolds, D. L. Jauncey, E. A. King, P. M. McCulloch, J. E. J. Lovell, and R. A. Preston. Interstellar Optics. *Astrophysical Journal letters*, 505(2):928–940, October 1998. doi:10.1086/306178.

C. R. Gwinn, C. Hirano, and S. Boldyrev. Interstellar scintillation of psr j0437-4715 on two scales. *Astronomy and Astrophysics*, 453(2):595–599, Jun 2006. doi:10.1051/0004-6361:20054280.

C. R. Gwinn, M. D. Johnson, J. E. Reynolds, D. L. Jauncey, A. K. Tzioumis, S. Dougherty, B. Carlson, D. Del Rizzo, H. Hirabayashi, H. Kobayashi, and et al. Noise in the cross-power spectrum of the vela pulsar. *The Astrophysical Journal*, 758 (1):6, Sep 2012. doi:10.1088/0004-637x/758/1/6.

Carl R Gwinn. Noodle model for scintillation arcs. *Monthly Notices of the Royal Astronomical Society*, 486(2):2809–2826, Mar 2019. doi:10.1093/mnras/stz894.

J. P. Hamaker and J. D. Bregman. Understanding radio polarimetry. III. Interpreting the IAU/IEEE definitions of the Stokes parameters. *Astronomy and Astrophysics Supplement*, 117:161–165, May 1996.

J. L. Han. Observing Interstellar and Intergalactic Magnetic Fields. *Annual Review of Astronomy and Astrophysics*, 55(1):111–157, August 2017. doi:10.1146/annurev-astro-091916-055221.

J. L. Han, R. N. Manchester, G. J. Qiao, and A. G. Lyne. The Large-scale Galactic Magnetic Field Structure and Pulsar Rotation Measures. In Matthew Bailes, David J. Nice, and Stephen E. Thorsett, editors, *Radio Pulsars*, volume 302 of *Astronomical Society of the Pacific Conference Series*, page 253, January 2003.

J. L. Han, K. Ferriere, and R. N. Manchester. The Spatial Energy Spectrum of Magnetic Fields in Our Galaxy. *ApJ*, 610(2):820–826, August 2004. doi:10.1086/421760.

J. L. Han, R. N. Manchester, A. G. Lyne, G. J. Qiao, and W. van Straten. Pulsar rotation measures and the large-scale structure of the galactic magnetic field. *The Astrophysical Journal*, 642(2):868–881, May 2006. doi:10.1086/501444.

J. L. Han, R. N. Manchester, W. van Straten, and P. Demorest. Pulsar rotation measures and large-scale magnetic field reversals in the galactic disk. *The Astrophysical Journal Supplement Series*, 234(1):11, jan 2018. doi:10.3847/1538-4365/aa9c45.

M. Haverkorn, J. C. Brown, B. M. Gaensler, and N. M. McClure-Griffiths. The outer scale of turbulence in the magnetoionized galactic interstellar medium. *The Astrophysical Journal*, 680(1):362–370, Jun 2008. doi:10.1086/587165.

D. J. Helfand, R. N. Manchester, and J. H. Taylor. Observations of pulsar radio emission. III. Stability of integrated profiles. *ApJ*, 198:661–670, June 1975. doi:10.1086/153644.

R. W. Hellings and G. S. Downs. Upper limits on the isotropic gravitational radiation background from pulsar timing analysis. *Astrophysical Journal Letters*, 265:L39–L42, February 1983. doi:10.1086/183954.

Daniel A Hemberger and Daniel R Stinebring. Scintillation & pulsar timing: Low-level timing noise from the kolmogorov halo. *Chinese Journal of Astronomy and Astrophysics*, 6(S2):185–188, oct 2006. doi:10.1088/1009-9271/6/s2/34.

Daniel A. Hemberger and Daniel R. Stinebring. Time Variability of Interstellar Scattering and Improvements to Pulsar Timing. *Apstrophysical Journal Letters*, 674(1):L37, February 2008. doi:10.1086/528985.

A. Hewish, S. J. Bell, J. D. H. Pilkington, and R. A. Collins P. F. Scott. Observation of a rapidly pulsaring radio source. *Nature*, 217(5130):709–713, Feb 1968. doi:10.1038/217709a0.

Alex S. Hill, Daniel R. Stinebring, Henry A. Barnor, Daniel E. Berwick, and Aaron B. Webber. Pulsar scintillation arcs. i. frequency dependence. *The Astrophysical Journal*, 599(1):457–464, dec 2003. doi:10.1086/379191.

Alex S. Hill, Daniel R. Stinebring, Curtis T. Asplund, Daniel E. Berwick, Wendeline B. Everett, and Natalie R. Hinkel. Deflection of pulsar signal reveals compact structures in the galaxy. *The Astrophysical Journal*, 619(2):L171–L174, Jan 2005. doi:10.1086/428347.

G. H. Hilmarsson, D. Michilli, L. G. Spitler, R. S. Wharton, P. Demorest, G. Desvignes, K. Gourdji, S. Hackstein, J. W. T. Hessels, K. Nimmo, and et al. Rotation measure evolution of the repeating fast radio burst source frb 121102. *The Astrophysical Journal*, 908(1):L10, Feb 2021. doi:10.3847/2041-8213/abdec0.

G Hobbs, A Archibald, Z Arzoumanian, D Backer, M Bailes, N D R Bhat, M Burgay, S Burke-Spolaor, D Champion, I Cognard, and et al. The international pulsar timing array project: using pulsars as a gravitational wave detector. *Classical and Quantum Gravity*, 27(8):084013, Apr 2010. doi:10.1088/0264-9381/27/8/084013.

G. Hobbs, W. Coles, R. N. Manchester, M. J. Keith, R. M. Shannon, D. Chen, M. Bailes,

N. D. R. Bhat, S. Burke-Spolaor, D. Champion, A. Chaudhary, A. Hotan, J. Khoo, J. Kocz, Y. Levin, S. Oslowski, B. Preisig, V. Ravi, J. E. Reynolds, J. Sarkissian, W. van Straten, J. P. W. Verbiest, D. Yardley, and X. P. You. Development of a pulsar-based time-scale. *Monthly Notices of the Royal Astronomical Society*, 427(4): 2780–2787, 12 2012. doi:10.1111/j.1365-2966.2012.21946.x.

George Hobbs et al. An ultra-wide bandwidth (704 to 4 032 MHz) receiver for the Parkes radio telescope. *Publications of the Astronomical Society of Australia*, 37: e012, April 2020. doi:10.1017/pasa.2020.2.

R. Hoogerwerf, J. H. J. de Bruijne, and P. T. de Zeeuw. On the origin of the O and B-type stars with high velocities. II. Runaway stars and pulsars ejected from the nearby young stellar groups. *Astronomy and Astrophysics*, 365:49–77, January 2001. doi:10.1051/0004-6361:20000014.

A. W. Hotan, W. van Straten, and R. N. Manchester. psrchive and psrfits: An open approach to radio pulsar data storage and analysis. *Publications of the Astronomical Society of Australia*, 21(3):302–309, 2004. doi:10.1071/as04022.

R. A. Hulse and J. H. Taylor. Discovery of a pulsar in a binary system. *The Astrophysical Journal Letters*, 195:L51–L53, January 1975. doi:10.1086/181708.

Jarrod Hurley. Centre for astrophsyics and supercomputing. `https://astronomy.swin.edu.au/supercomputing/`, 2020.

F. A. Jenet, S. B. Anderson, V. M. Kaspi, T. A. Prince, and S. C. Unwin. Radio pulse properties of the millisecond pulsar PSR j0437-4715. i. observations at 20 centimeters. *The Astrophysical Journal*, 498(1):365–372, may 1998. doi:10.1086/305529.

Fredrick A. Jenet and Joseph D. Romano. Understanding the gravitational-wave hellings and downs curve for pulsar timing arrays in terms of sound and electromagnetic waves, 2015.

Simon Johnston, D. R. Lorimer, P. A. Harrison, M. Bailes, A. G. Lynet, J. F. Bell, V. M. Kaspi, R. N. Manchester, N. D'Amico, L. Nleastrol, and Jin Shengzhen. Discovery of a very bright, nearby binary millisecond pulsar. *Nature*, 361(6413):613–615, February 1993. doi:10.1038/361613a0.

J. Jonas et al. The MeerKAT Radio Telescope. In *MeerKAT Science: On the Pathway to the SKA*, page 1, January 2016.

A. Karastergiou. The complex polarization angles of radio pulsars: orthogonal jumps and interstellar scattering. *Monthly Notices of the Royal Astronomical Society: Letters*, 392(1):L60–L64, Jan 2009. doi:10.1111/j.1745-3933.2008.00585.x.

A. Karastergiou and S. Johnston. Absolute polarization position angle profiles of southern pulsars at 1.4 and 3.1 GHz. *Monthly Notices of the Royal Astronomical Society*, 365(2):353–366, 01 2006. doi:10.1111/j.1365-2966.2005.09692.x.

M. Kerr, W. A. Coles, C. A. Ward, S. Johnston, A. V. Tuntsov, and R. M. Shannon. Extreme Scattering Events Towards Two Young Pulsars. *Mon. Not. Roy. Astron. Soc.*, 474(4):4637–4647, 2018. doi:10.1093/mnras/stx3101.

F. Kirsten, N. D. R. Bhat, B. W. Meyers, J.-P. Macquart, S. E. Tremblay, and S. M. Ord. Probing pulsar scattering between 120 and 280 mhz with the mwa. *The Astrophysical Journal*, 874(2):179, Apr 2019. doi:10.3847/1538-4357/ab0c05.

M. Kramer, D.C. Backer, J.M. Cordes, T.J.W. Lazio, B.W. Stappers, and S. Johnston. Strong-field tests of gravity using pulsars and black holes. *New Astronomy Reviews*, 48(11-12):993–1002, Dec 2004. doi:10.1016/j.newar.2004.09.020.

Michael Kramer, Christoph Lange, Duncan R. Lorimer, Donald C. Backer, Kiriaki M. Xilouris, Axel Jessner, and Richard Wielebinski. The Characteristics of Millisecond Pulsar Emission. III. From Low to High Frequencies. *Astrophysical Journal Letters*, 526(2):957–975, December 1999. doi:10.1086/308042.

Shrinivas R. Kulkarni. Self-noise in interferometers - Radio and infrared. *Astronomical Journal*, 98:1112–1130, September 1989. doi:10.1086/115202.

A. D. Kuzmin and B. Ya. Losovsky. No low-frequency turn-over in the spectra of millisecond pulsars. *Astronomy and Astrophysics*, 368:230–238, March 2001.

doi:10.1051/0004-6361:20000507.

Dong Lai. *Neutron Star Kicks and Asymmetric Supernovae*, volume 578, page 424. Lecture Notes in Physics, 2001.

P. Lazarus, R. Karuppusamy, E. Graikou, R. N. Caballero, D. J. Champion, K. J. Lee, J. P. W. Verbiest, and M. Kramer. Prospects for high-precision pulsar timing with the new Effelsberg PSRIX backend. *Monthly Notices of the Royal Astronomical Society*, 458(1):868–880, 03 2016. doi:10.1093/mnras/stw189.

L. C. Lee. Wave propagation in a random medium: A complete set of the moment equations with different wavenumbers. *Journal of Mathematical Physics*, 15:1431, August 1974. doi:10.1063/1.1666828.

L. C. Lee and J. R. Jokipii. Strong scintillations in astrophysics. II. A theory of temporal broadening of pulses. *Astrophysical Journal Letters*, 201:532–543, October 1975a. doi:10.1086/153916.

L. C. Lee and J.R. Jokipii. Strong scintillations in astrophysics. I. The Markov approximation, its validity and application to angular broadening. *Astrophysical Journal Letters*, 196:695–707, March 1975b. doi:10.1086/153458.

Wojciech Lewandowski, Marta Dembska, Jaroslaw Kijak, and Magdalena Kowalińska. Pulse broadening analysis for several new pulsars and anomalous scattering. *Monthly Notices of the Royal Astronomical Society*, 434(1):69–83, 07 2013. doi:10.1093/mnras/stt989.

Dongzi Li. Scintillation arcs using the large european array for pulsars. `https://www.atnf.csiro.au/research/conferences/2020/ipta/contributed/RMain_IPTA_2020Sept.pdf`, 2020.

Dongzi Li, Fang Xi Lin, Robert Main, Ue-Li Pen, Marten H van Kerkwijk, and I-Sheng Yang. Constraining magnetic fields through plasma lensing: application to the black widow pulsar. *Monthly Notices of the Royal Astronomical Society*, 484(4):5723–5733, Jan 2019. doi:10.1093/mnras/stz374.

D. R. Lorimer and M. Kramer. *Handbook of Pulsar Astronomy*, volume 4. Cambridge University Press, 2004.

D. R. Lorimer, M. Bailes, M. A. McLaughlin, D. J. Narkevic, and F. Crawford. A Bright Millisecond Radio Burst of Extragalactic Origin. *Science*, 318(5851):777, November 2007. doi:10.1126/science.1147532.

Duncan R. Lorimer. Binary and millisecond pulsars. *Living Reviews in Relativity*, 11 (1), Nov 2008. doi:10.12942/lrr-2008-8.

A. G Lyne. A review of the double pulsar - PSR j0737-3039. *Chinese Journal of Astronomy and Astrophysics*, 6(S2):162–168, oct 2006. doi:10.1088/1009-9271/6/s2/30.

J. P. Macquart and D. B. Melrose. Circular polarization induced by scintillation in a magnetized medium. *Physical Review Letters*, 62(3):4177–4188, September 2000a. doi:10.1103/PhysRevE.62.4177.

J. P. Macquart and D. B. Melrose. Scintillation-induced Circular Polarization in Pulsars and Quasars. *Astrophysical Journal Letters*, 545(2):798–806, December 2000b. doi:10.1086/317852.

Jean-Pierre Macquart. Probing the Universe's baryons with fast radio bursts. *Nature Astronomy*, 2:836–838, October 2018. doi:10.1038/s41550-018-0625-7.

R. Main et al. Measuring interstellar delays of PSR J06130200 over 7 yr, using the Large European Array for Pulsars. *Monthly Notices of the Royal Astronomical Society*, 499 (1):1468–1479, 09 2020. doi:10.1093/mnras/staa2955.

Robert Main and Marten H. van Kerkwijk. Mapping the emission location of the crab pulsar's giant pulses. *The Astrophysical Journal*, 13(S337):83–83, 2021. doi:10.1017/S1743921317009176.

R N Manchester. Pulsar timing and its applications. *Journal of Physics: Conference Series*, 932:012002, dec 2017. doi:10.1088/1742-6596/932/1/012002.

Olaf Maron, J Kijak, and R Wielebinski. Observations of millisecond pulsars at 8.35 ghz. *Astronomy and Astrophysics*, 413:19–22, 01 2004. doi:10.1051/0004-6361:20031707.

C. F. McKee and J. P. Ostriker. A theory of the interstellar medium: three components regulated by supernova explosions in an inhomogeneous substrate. *ApJ*, 218:148–169, November 1977. doi:10.1086/155667.

M. M. McKinnon. Birefringence as a mechanism for the broadening and depolarization of pulsar average profiles. *The Astrophysical Journal*, 475(2):763–769, feb 1997. doi:10.1086/303542.

Anthony H. Minter and Steven R. Spangler. Observation of Turbulent Fluctuations in the Interstellar Plasma Density and Magnetic Field on Spatial Scales of 0.01 to 100 Parsecs. *ApJ*, 458:194, February 1996. doi:10.1086/176803.

V Morello et al. The high time resolution universe survey – xiv. discovery of 23 pulsars through gpu-accelerated reprocessing. *Monthly Notices of the Royal Astronomical Society*, 483(3):3673–3685, Dec 2018. doi:10.1093/mnras/sty3328.

Maria Moutzouri. Flux density and spectral variability of pulsars. Master's thesis, The University of Manchester, UK, 2018.

Ramesh Narayan. The physics of pulsar scintillation. *Philosophical Transactions: Physical Sciences and Engineering*, 341(1660):151–165, 1992.

Hiroshi Ohno and Shinpei Shibata. The random magnetic field in the Galaxy. *Monthly Notices of the Royal Astronomical Society*, 262(4):953–962, June 1993. doi:10.1093/mnras/262.4.953.

J. R. Oppenheimer and G. M. Volkoff. On Massive Neutron Cores. *Physical Review*, 55(4):374–381, February 1939. doi:10.1103/PhysRev.55.374.

S. Osłowski, W. van Straten, G. B. Hobbs, M. Bailes, and P. Demorest. High signal-to-noise ratio observations and the ultimate limits of precision pulsar timing. *Monthly Notices of the Royal Astronomical Society*, 418(2):1258–1271, December 2011. doi:10.1111/j.1365-2966.2011.19578.x.

Aditya Parthasarathy. *Timing properties across the pulsar population*. PhD thesis, Monash Centre for Astrophysics (MoCA), School of Physics and Astronomy, Monash

University, Victoria 3800, Australia, January 2020.

Ue-Li Pen and Yuri Levin. Pulsar scintillations from corrugated reconnection sheets in the interstellar medium. *Monthly Notices of the Royal Astronomical Society*, 442(4): 3338–3346, Jun 2014. doi:10.1093/mnras/stu1020.

M. Angeles Perez-Garcia, Joseph Silk, and Ue-Li Pen. Pulsar scintillation patterns and strangelets. *Physics Letters B*, 727(4-5):357–360, Dec 2013. doi:10.1016/j.physletb.2013.11.007.

Nataliya Konstantinovna Porayko. *Probing the Interstellar Medium and Dark Matter with Pulsars*. PhD thesis, Rheinische Friedrich-Wilhelms-Universität Bonn, March 2020.

Markus Pössel. The Shapiro time delay and the equivalence principle. *arXiv e-prints*, art. arXiv:2001.00229, December 2019.

V. Radhakrishnan and D. J. Cooke. Magnetic Poles and the Polarization Structure of Pulsar Radiation. *Astrophysical Letters*, 3:225, January 1969.

Blagoy Rangelov, George G. Pavlov, Oleg Kargaltsev, Martin Durant, Andrei M. Bykov, and Alexandre Krassilchtchikov. First detection of a pulsar bow shock nebula in far-uv: Psr j0437–4715. *The Astrophysical Journal*, 831(2):129, Nov 2016. doi:10.3847/0004-637x/831/2/129.

S. Ransom. Sensitivity and Noise. Lecture notes, Theoretical Institute for Advanced Research in Astrophysics, Academia Sinica, Taipei, 2017. URL: https://events.asiaa.sinica.edu.tw/school/20160815/talk/sransom0818.pdf.

D. J. Reardon, G. Hobbs, W. Coles, Y. Levin, M. J. Keith, M. Bailes, N. D. R. Bhat, S. Burke-Spolaor, S. Dai, M. Kerr, P. D. Lasky, R. N. Manchester, S. Osłowski, V. Ravi, R. M. Shannon, W. van Straten, L. Toomey, J. Wang, L. Wen, X. P. You, and X.-J. Zhu. Timing analysis for 20 millisecond pulsars in the Parkes Pulsar Timing Array. *Monthly Notices of the Royal Astronomical Society*, 455(2):1751–1769, 11 2015. doi:10.1093/mnras/stv2395.

Daniel J. Reardon. Meerguard a meertime copy of coastguard. `https://github.com/danielreardon/MeerGuard`, commit = 3c39141ef6efde039d707ab98672541b1fb5a34 , 2019.

Daniel J. Reardon. Scintools: Pulsar scintillation data tools, November 2020.

Daniel J. Reardon, William A. Coles, Matthew Bailes, et al. Precision orbital dynamics from interstellar scintillation arcs for psr j0437–4715. *The Astrophysical Journal*, 904(2):104, Nov 2020. doi:10.3847/1538-4357/abbd40.

Daniel John Reardon. *Precision Radio-Frequency Pulsar Timing & Interstellar Scintillometry*. PhD thesis, Monash Centre for Astrophysics (MoCA), School of Physics and Astronomy, Monash University, Victoria 3800, Australia, September 2018.

B. J. Rickett. Interstellar scattering and scintillation of radio waves. *Annual review of astronomy and astrophysics*, 15:479–504, January 1977. doi:10.1146/annurev.aa.15.090177.002403.

B. J. Rickett. Radio propagation through the turbulent interstellar plasma. *Annual Reviews in Astronomy and Astrophysics*, 28:561–605, January 1990. doi:10.1146/annurev.aa.28.090190.003021.

B. J. Rickett, W. A. Coles, C. F. Nava, M. A. McLaughlin, S. M. Ransom, F. Camilo, R. D. Ferdman, P. C. C. Freire, M. Kramer, A. G. Lyne, and I. H. Stairs. Interstellar Scintillation of the Double Pulsar J0737-3039. *The Astrophysical Journal*, 787(2): 161, June 2014. doi:10.1088/0004-637X/787/2/161.

Barney J. Rickett, Andrew G. Lyne, and Yashwant Gupta. Interstellar Fringes from Pulsar B0834+06. *Monthly Notices of the Royal Astronomical Society*, 287(4): 739–752, June 1997. doi:10.1093/mnras/287.4.739.

Timothy Robishaw and Carl Heiles. The measurement of polarization in radio astronomy. *The WSPC Handbook of Astronomical Instrumentation*, 2018. doi:10.1142/9789811203770_0006.

E. R. Safutdinov, M. V. Popov, Ya. Gupta, D. Mitra, and U. Kumar. Secondary dynamical spectra of pulsars as indicators of inhomogeneities in the interstellar plasma. *Astronomy Reports*, 61(5):406–416, May 2017. doi:10.1134/S1063772917050055.

P. A. G. Scheuer. Amplitude Variations in Pulsed Radio Sources. *Nature*, 218(5145): 920–922, June 1968. doi:10.1038/218920a0.

M Serylak, S Johnston, M Kramer, S Buchner, A Karastergiou, M J Keith, A Parthasarathy, P Weltevrede, M Bailes, E D Barr, F Camilo, M Geyer, B V Hugo, A Jameson, D J Reardon, R M Shannon, R Spiewak, W van Straten, and V Venkatraman Krishnan. The thousand-pulsar-array programme on MeerKAT IV: Polarization properties of young, energetic pulsars. *Monthly Notices of the Royal Astronomical Society*, 505(3): 4483–4495, 05 2021. doi:10.1093/mnras/staa2811.

Andrew P. V. Siemion et al. Searching for extraterrestrial intelligence with the square kilometre array, 2014.

J. H. Simonetti, J. M. Cordes, and S. R. Spangler. Small-scale variations in the galactic magnetic field : the rotation measure structure function and birefringence in interstellar scintillations. *Astrophysical Journal Leters*, 284:126–134, September 1984. doi:10.1086/162391.

T. V. Smirnova, C. R. Gwinn, and V. I. Shishov. Interstellar scintillation of PSR J0437-4715. *Astronomy and Astrophysics*, 453(2):601–607, July 2006. doi:10.1051/0004-6361:20054281.

F. Snik. *Astronomical Polarimetry : new concepts, new instruments, new measurements and observations*. PhD thesis, Utrecht University, October 2009.

Charlotte Sobey. Investigating astrophysical plasmas using LOFAR observations of pulsars. In *American Astronomical Society Meeting Abstracts #223*, volume 223 of *American Astronomical Society Meeting Abstracts*, page 212.02, January 2014.

H. Spruit and E. S. Phinney. Birth kicks as the origin of pulsar rotation. *Nature*, 393 (6681):139–141, May 1998. doi:10.1038/30168.

D. H. Staelin and E. C. Reifenstein. Pulsating radio sources near the crab nebula. *Science*, 162(3861):1481–1483, December 1968. doi:10.1126/science.162.3861.1481.

Steven W. Stahler and Francesco Palla. *The Formation of Stars*. Wiley, 2004.

B. W. Stappers, A. G. J. van Leeuwen, M. Kramer, D. Stinebring, and J. Hessels. LOFAR: A powerful tool for pulsar studies. In W. Becker and H. H. Huang, editors, *WE-Heraeus Seminar on Neutron Stars and Pulsars 40 years after the Discovery*, page 100, January 2007.

D. R. Stinebring, M. A. McLaughlin, J. M. Cordes, K. M. Becker, J. E. Espinoza Goodman, M. A. Kramer, J. L. Sheckard, and C. T. Smith. Faint Scattering Around Pulsars: Probing the Interstellar Medium on Solar System Size Scales. *ApJ*, 549(1): L97–L100, March 2001. doi:10.1086/319133.

G. G. Stokes. On the Composition and Resolution of Streams of Polarized Light from different Sources. *Transactions of the Cambridge Philosophical Society*, 9:399, January 1851.

P. A. Sturrock. A Model of Pulsars. *ApJ*, 164:529, March 1971. doi:10.1086/150865.

Kandaswamy Subramanian. Magnetic fields in the universe, 2018.

Kandaswamy Subramanian. From primordial seed magnetic fields to the galactic dynamo. *Galaxies*, 7(2):47, Apr 2019. doi:10.3390/galaxies7020047.

A. Suresh and J. M. Cordes. Induced polarization from birefringent pulse splitting in magneto-ionic media. *The Astrophysical Journal*, 870(1):29, Jan 2019. doi:10.3847/1538-4357/aaf004.

Mayuresh Surnis. *Radio Pulsar Search and Timing*. PhD thesis, Tata Institute of Fundamental Research, 01 2017.

Caterina Tiburzi. Pulsars probe the low-frequency gravitational sky: Pulsar timing arrays basics and recent results. *Publications of the Astronomical Society of Australia*, 35, 2018. doi:10.1017/pasa.2018.7.

S. J. Tingay, R. Goeke, J. D. Bowman, D. Emrich, S. M. Ord, D. A. Mitchell, M. F.

Morales, T. Booler, B. Crosse, R. B. Wayth, and et al. The murchison widefield array: The square kilometre array precursor at low radio frequencies. *Publications of the Astronomical Society of Australia*, 30:e007, 2013. doi:10.1017/pasa.2012.007.

J.W. Tukey. *Exploratory Data Analysis*. Number v. 2 in Addison-Wesley series in behavioral science. Addison-Wesley Publishing Company, 1977. ISBN 9780201076165.

A. V. Tuntsov, H. E. Bignall, and M. A. Walker. Power-law models of totally anisotropic scattering. *Monthly Notices of the Royal Astronomical Society*, 429(3):2562–2568, Jan 2013. doi:10.1093/mnras/sts527.

W. van Straten and M. Bailes. Dspsr: Digital signal processing software for pulsar astronomy. *Publications of the Astronomical Society of Australia*, 28(1):1–14, 2011. doi:10.1071/AS10021.

W. van Straten, M. Bailes, M. Britton, S. R Kulkarni, S. B. Anderson, R. N. Manchester, and J. Sarkissian. A test of general relativity from the three-dimensional orbital geometry of a binary pulsar. *Nature*, 412(6843):158–160, Jul 2001. doi:10.1038/35084015.

W. van Straten, R. N. Manchester, S. Johnston, and J. E. Reynolds. psrchive and psrfits: Definition of the stokes parameters and instrumental basis conventions. *Publications of the Astronomical Society of Australia*, 27(1):104–109, 2010. doi:10.1071/as09084.

Willem van Straten, Paul Demorest, and Stefan Oslowski. Pulsar Data Analysis with PSRCHIVE. *Astronomical Research and Technology*, 9(3):237–256, July 2012.

M. A. Walker. Extreme Scattering Events: Insights into the Interstellar Medium on AU-Scales. In M. Haverkorn and W. M. Goss, editors, *SINS - Small Ionized and Neutral Structures in the Diffuse Interstellar Medium*, volume 365 of *Astronomical Society of the Pacific Conference Series*, page 299, July 2007.

M. A. Walker, D. B. Melrose, D. R. Stinebring, and C. M. Zhang. Interpretation of parabolic arcs in pulsar secondary spectra. *Monthly Notices of the Royal Astronomical Society*, 354(1):43–54, Oct 2004. doi:10.1111/j.1365-2966.2004.08159.x.

Mark A. Walker, Paul B. Demorest, and Willem van Straten. CYCLIC SPECTROSCOPY OF THE MILLISECOND PULSAR, b1937+21. *The Astrophysical Journal*, 779(2):99, nov 2013. doi:10.1088/0004-637x/779/2/99.

Mark A. Walker, Artem V. Tuntsov, Hayley Bignall, Cormac Reynolds, Keith W. Bannister, Simon Johnston, Jamie Stevens, and Vikram Ravi. Extreme radio-wave scattering associated with hot stars. *The Astrophysical Journal*, 843(1):15, Jun 2017. doi:10.3847/1538-4357/aa705c.

N. Wang, R. N. Manchester, S. Johnston, B. Rickett, J. Zhang, A. Yusup, and M. Chen. Long-term scintillation observations of five pulsars at 1540 MHz. *Monthly Notices of the Royal Astronomical Society*, 358(1):270–282, 03 2005. doi:10.1111/j.1365-2966.2005.08798.x.

J. M. Wrobel and R. C. Walker. Sensitivity. In G. B. Taylor, C. L. Carilli, and R. A. Perley, editors, *Synthesis Imaging in Radio Astronomy II*, volume 180 of *Astronomical Society of the Pacific Conference Series*, page 171, January 1999.

Siyao Xu and Bing Zhang. SCATTER BROADENING OF PULSARS AND IMPLICATIONS ON THE INTERSTELLAR MEDIUM TURBULENCE. *The Astrophysical Journal*, 835(1):2, jan 2017. doi:10.3847/1538-4357/835/1/2.

J. M. Yao, R. N. Manchester, and N. Wang. A new electron-density model for estimation of pulsar and frb distances. *The Astrophysical Journal*, 835(1):29, Jan 2017. doi:10.3847/1538-4357/835/1/29.

X. P. You et al. Dispersion measure variations and their effect on precision pulsar timing. *Monthly Notices of the Royal Astronomical Society*, 378(2):493–506, 05 2007. doi:10.1111/j.1365-2966.2007.11617.x.

Bing Zhang. Radio Pulsar Death. *Acta Astronomica Sinica*, 44:215–222, February 2003.

Xia Zhou, Hao Tong, Cui Zhu, and Na Wang. Dependence of pulsar death line on the equation of state. *Monthly Notices of the Royal Astronomical Society*, 472(2):

2403–2409, 08 2017. doi:10.1093/mnras/stx2114.

# Appendix A

# Glossary

**ACF** Autocovariance Function

**CP** Circular Polarization

**DM** Dispersion Measure

**Dynspec** Dynamic Spectra

**EoS** Equation of State

**FFT** Fast Fourier Transform

**GMF** Galactic Magnetic Field

**GR** General Relativity

**GW** Gravitational Wave

**IISM** Ionised Interstellar Medium

**ISM** Interstellar Medium

**L/LCP** Left Circularly Polarized

**LoS** Laser Interferometer Gravitational Wave Observatory

**MSP** Millisecond Pulsar

**MWA** Murchison Widefield Array

**NS** Neutron Star

**O** Ordinary

**PK** Post-Keplerian

**NS** Neutron Star

**PSR** Pulsar

**PA** Position Angle

**R/RCP** Right Circularly Polarized

**RM** Rotation Measure

**RFI** Radio Frequency Interfernece

**SKA** Square Kilometer Array

**SNR** Supernova Remnant

**S/N** Signal to Noise Ratio

**SSpec** Secondary Spectra

**TOA** Time of Arrival

**X** Extraordinary

# Appendix B

# Arc Curvatures

## B.1 Uncalibrated Data

### B.1.1 Combined Integrations

| Epoch | Integration Length | LCP | RCP |
|---|---|---|---|
| 26-12-2019 | 11 | 66.2 | 66.1 |
| 27-12-2019 | 11 | 65.6 | 65.6 |
| 28-12-2019 | 12 | 54.5 | 54.5 |
| 29-12-2019 | 11 | 48.1 | 48.1 |
| 30-12-2019 | 11 | 51.2 | 51.5 |
| 31-12-2019 | 11 | 59 | 59 |

Table B.1: Arc curvatures for day length integrations across the full L band of MeerKAT.

| Epoch | Integration Length | LCP | RCP |
|---|---|---|---|
| 26-12-2019 | 11 | 65.8 | 65.8 |
| 27-12-2019 | 11 | 64.9 | 64.8 |
| 28-12-2019 | 12 | 53.9 | 53.9 |
| 29-12-2019 | 11 | 48.2 | 48.2 |
| 30-12-2019 | 11 | 51.0 | 51.1 |
| 31-12-2019 | 11 | 60.9 | 60.9 |

Table B.2: Arc curvatures for day length integrations across the low frequency portion of the L band of MeerKAT ($856 < f < 1100$) MHz.

### B.1.2 Sub-integrations

| Epoch | Duration | LCP FB | RCP FB | LCP LF | RCP LF |
|---|---|---|---|---|---|
| 26-12-2019 | 16:00:00-17:00:00 | 65.5 | 65.5 | 65.0 | 65.0 |
| | 17:00:00-18:00:00 | 64.9 | 65 | 64.7 | 64.7 |
| | 18:00:00-19:00:00 | 66.0 | 66.0 | 65.6 | 65.6 |
| | 19:00:00-20:00:00 | 67.1 | 67.2 | 66.5 | 66.5 |
| | 20:00:00-21:00:00 | 66.8 | 66.7 | 65.4 | 65.5 |
| | 21:00:00-22:00:00 | 65.2 | 65.2 | 65.2 | 65.2 |
| | 22:00:00-23:00:00 | 66.6 | 66.6 | 66.3 | 66.3 |
| | 23:00:00-00:00:00 | 66.4 | 66.4 | 65.6 | 65.5 |
| | 00:00:00-01:00:00 | 66.7 | 66.7 | 66.0 | 66.0 |
| | 01:00:00-02:00:00 | 67.2 | 67.2 | 65.8 | 65.8 |
| | 02:00:00-03:00:00 | 76.3 | 75.2 | 70.2 | 71.9 |
| 27-12-2019 | 15:00:00-16:00:00 | 66.1 | 66.1 | 65.4 | 65.3 |
| | 16:00:00-17:00:00 | 66.9 | 66.9 | 65.9 | 65.9 |
| | 17:00:00-18:00:00 | 66.1 | 66.1 | 65.0 | 65.0 |
| | 18:00:00-19:00:00 | 65.7 | 65.8 | 64.1 | 64.1 |
| | 19:00:00-20:00:00 | 65.2 | 65.2 | 64.7 | 64.6 |
| | 20:00:00-21:00:00 | 64.3 | 64.4 | 64.0 | 63.9 |
| | 21:00:00-22:00:00 | 63.9 | 63.9 | 63.5 | 63.5 |
| | 22:00:00-23:00:00 | 63.6 | 63.6 | 63.1 | 63.1 |
| | 23:00:00-00:00:00 | 63.8 | 63.7 | 63.0 | 63.0 |
| | 00:00:00-01:00:00 | 63.0 | 63.0 | 62.8 | 62.8 |
| | 01:00:00-02:00:00 | 62.8 | 62.7 | 62.3 | 62.4 |
| 28-12-2019 | 14:00:00-15:00:00 | 56.9 | 56.9 | 56.8 | 57.0 |
| | 15:00:00-16:00:00 | 56.0 | 56.0 | 56.0 | 56.0 |
| | 16:00:00-17:00:00 | 55.4 | 55.4 | 55.4 | 55.4 |
| | 17:00:00-18:00:00 | 54.9 | 54.9 | 54.8 | 54.8 |
| | 18:00:00-19:00:00 | 54.6 | 54.8 | 54.5 | 54.5 |
| | 19:00:00-20:00:00 | 53.9 | 53.9 | 54.1 | 54.1 |
| | 20:00:00-21:00:00 | 53.3 | 53.2 | 53.5 | 53.5 |
| | 21:00:00-22:00:00 | 53.2 | 53.2 | 53.2 | 53.2 |
| | 22:00:00-23:00:00 | 52.8 | 52.8 | 52.8 | 52.8 |
| | 23:00:00-00:00:00 | 52.9 | 52.9 | 53.0 | 53.0 |
| | 00:00:00-01:00:00 | 52.2 | 52.2 | 52.2 | 52.2 |
| | 01:00:00-02:00:00 | 51.7 | 51.7 | 51.6 | 51.6 |

Table B.3: Arc curvatures for 26-12-2019 to 28-12-2019. FB indicates the full L-band. LF indicates a low frequency portion of the L- band ($856 < f < 1100$ MHz)

| Epoch | Duration | LCP FB | RCP FB | LCP LF | RCP LF |
|---|---|---|---|---|---|
| 29-12-2019 | 15:00:00-16:00:00 | 48.7 | 48.7 | 48.5 | 48.5 |
| | 16:00:00-17:00:00 | 48.7 | 48.6 | 48.8 | 48.7 |
| | 17:00:00-18:00:00 | 48.7 | 48.8 | 48.5 | 48.6 |
| | 18:00:00-19:00:00 | 48.0 | 48.0 | 48.1 | 48.1 |
| | 19:00:00-20:00:00 | 48.5 | 48.5 | 48.5 | 48.5 |
| | 20:00:00-21:00:00 | 48.1 | 48.1 | 48.3 | 48.3 |
| | 21:00:00-22:00:00 | 47.8 | 47.8 | 47.8 | 47.8 |
| | 22:00:00-23:00:00 | 47.9 | 47.9 | 48.1 | 48.1 |
| | 23:00:00-00:00:00 | 47.8 | 47.9 | 47.9 | 47.9 |
| | 00:00:00-01:00:00 | 48.0 | 47.9 | 48.1 | 48.0 |
| | 01:00:00-02:00:00 | 48.3 | 48.3 | 48.1 | 48.1 |
| 30-12-2019 | 15:00:00-16:00:00 | 50.9 | 50.9 | 49.9 | 49.8 |
| | 16:00:00-17:00:00 | 50.6 | 50.5 | 50.2 | 50.2 |
| | 17:00:00-18:00:00 | 50.6 | 50.6 | 50.0 | 50.0 |
| | 18:00:00-19:00:00 | 50.1 | 50.1 | 49.6 | 49.7 |
| | 19:00:00-20:00:00 | 50.7 | 50.7 | 50.5 | 50.4 |
| | 20:00:00-21:00:00 | 51.2 | 51.2 | 50.4 | 50.4 |
| | 21:00:00-22:00:00 | 51.8 | 51.5 | 51.4 | 51.3 |
| | 22:00:00-23:00:00 | 51.6 | 51.6 | 51.6 | 51.6 |
| | 23:00:00-00:00:00 | 51.5 | 51.5 | 51.8 | 51.8 |
| | 00:00:00-01:00:00 | 52.0 | 51.9 | 51.5 | 51.5 |
| | 01:00:00-02:00:00 | 52.1 | 52.1 | 52.7 | 52.7 |
| 31-12-2019 | 15:00:00-16:00:00 | 57.5 | 57.5 | 57.8 | 57.8 |
| | 16:00:00-17:00:00 | 57.5 | 57.4 | 57.7 | 57.7 |
| | 17:00:00-18:00:00 | 57.8 | 57.9 | 50.0 | 50.0 |
| | 18:00:00-19:00:00 | 57.9 | 58.0 | 49.6 | 49.7 |
| | 19:00:00-20:00:00 | 58.6 | 58.6 | 50.5 | 50.4 |
| | 20:00:00-21:00:00 | 59.1 | 59.2 | 50.4 | 50.4 |
| | 21:00:00-22:00:00 | 59.5 | 59.5 | 51.4 | 51.3 |
| | 22:00:00-23:00:00 | 59.5 | 59.5 | 51.6 | 51.6 |
| | 23:00:00-00:00:00 | 60.2 | 60.2 | 51.8 | 51.8 |
| | 00:00:00-01:00:00 | 60.4 | 60.2 | 52.5 | 52.5 |
| | 01:00:00-02:00:00 | 60.6 | 60.6 | 52.7 | 52.7 |

Table B.4: Arc curvatures for 2019-12-29 to 2019-12-31.FB indicates the full L-band. LF indicates a low frequency portion of the L- band (856 < f < 1100 MHz)

## B.2 Calibrated Data

### B.2.1 Combined Integrations

| Epoch | Integration Length | LCP | RCP |
|---|---|---|---|
| 26-12-2019 | 11 | 66.6 | 66.6 |
| 27-12-2019 | 11 | 63.7 | 63.7 |
| 28-12-2019 | 8 | 54.2 | 54.3 |
| 29-12-2019 | 11 | 48.0 | 48.0 |
| 30-12-2019 | 11 | 51.7 | 51.8 |
| 31-12-2019 | 11 | 59.3 | 59.3 |

Table B.5: Arc curvatures for 11 hour integrations across the full L-band.

| Epoch | Integration Length | LCP | RCP |
|---|---|---|---|
| 26-12-2019 | 11 | 65.5 | 66.1 |
| 27-12-2019 | 11 | 64.1 | 64.2 |
| 28-12-2019 | 8 | 54.1 | 54.6 |
| 29-12-2019 | 11 | 48.1 | 48.1 |
| 30-12-2019 | 11 | 51.2 | 51.2 |
| 31-12-2019 | 11 | 61.1 | 60.8 |

Table B.6: Arc curvatures for 11 hour integrations across the low frequency portion of the L-band (856 $< f <$ 1100 MHz).

### B.2.2 Sub-integrations

| Epoch | Duration | LCP FB | RCP FB | LCP LF | RCP LF |
|---|---|---|---|---|---|
| 26-12-2019 | 16:00:00-20:00:00 | 66.4 | 66.4 | 66.0 | 66.0 |
| | 20:00:00—:00:00 | 66.1 | 66.1 | 65.4 | 65.5 |
| | 00:00:00-03:00:00 | 67.8 | 68.0 | 67.1 | 67.1 |
| 27-12-2019 | 15:00:00-19:00:00 | 64.4 | 64.4 | 64.4 | 64.4 |
| | 19:00:00-23:00:00 | 63.6 | 63.6 | 64.0 | 64.0 |
| | 23:00:00-02:00:00 | 62.4 | 62.4 | 62.0 | 62.0 |
| 28-12-2019 | 14:00:00-18:00:00 | 58.4 | 58.4 | 55.6 | 55.6 |
| | 18:00:00-22:00:00 | NA | NA | NA | NA |
| | 22:00:00-02:00:00 | 53.1 | 53.1 | 52.3 | 52.4 |
| 29-12-2019 | 15:00:00-19:00:00 | 48.3 | 48.3 | 48.3 | 48.3 |
| | 19:00:00-23:00:00 | 48.6 | 48.6 | 48.2 | 48.2 |
| | 23:00:00-02:00:00 | 48.3 | 48.3 | 49.2 | 49.2 |
| 30-12-2019 | 15:00:00-19:00:00 | 51.1 | 51.1 | 50.7.0 | 50.7 |
| | 19:00:00-23:00:00 | 51.3 | 51.3 | 51.5 | 51.6 |
| | 23:00:00-02:00:00 | 51.6 | 51.5 | 53.2 | 53.3 |
| 31-12-2019 | 15:00:00-19:00:00 | 57.6 | 57.6 | 59.8 | 58.7 |
| | 19:00:00-23:00:00 | 60.3 | 60.3 | 54.6 | 54.6 |
| | 23:00:00-02:00:00 | 60.3 | 60.3 | 62.6 | 65.1 |

Table B.7: Arc curvatures for 26-12-2019 to 31-12-2019.FB indicates the full L-band. LF indicates a low frequency portion of the L- band ($856 < f < 1100$ MHz).

# Appendix C

# Magnetoionic Field Estimates

## C.1 Upper Limits of Magnetoionic Field Fluctuations

| Obs. Epoch | -5 < $f_t$ < 0 | | 0 < $f_t$ < 5 | |
|---|---|---|---|---|
| | $\langle \Delta\phi^2_{\delta\beta} \rangle^{1/2}$ | $\langle \delta\beta^2_z \rangle^{1/2}$ | $\langle \Delta\phi^2_{\delta\beta} \rangle^{1/2}$ | $\langle \delta\beta^2_z \rangle^{1/2}$ |
| 2019-12-26 | 0.021 | 345 | 0.031 | 509 |
| 2019-12-27 | 0.016 | 262 | 0.017 | 279 |
| 2019-12-28 | 0.037 | 607 | 0.019 | 312 |
| 2019-12-29 | 0.106 | 1864 | 0.117 | 1922 |
| 2019-12-30 | 0.068 | 1117 | 0.029 | 476 |
| 2019-12-31 | 0.033 | 542 | 0.046 | 755 |

Table C.1: Upper limits of small scale magnetoionic spatial fluctuations, $\langle \delta\beta^2_z \rangle^{1/2}$ (inner arc small $f_t$ sample), estimated from $\hat{\Gamma}_{\mathrm{RL}}$ and $\nu$, $D$, and $r_F$ for all observations.

| Obs. Epoch | $f_t$ < -5 | | $f_t$ > 5 | |
|---|---|---|---|---|
| | $\langle \Delta\phi^2_{\delta\beta} \rangle^{1/2}$ | $\langle \delta\beta^2_z \rangle^{1/2}$ | $\langle \Delta\phi^2_{\delta\beta} \rangle^{1/2}$ | $\langle \delta\beta^2_z \rangle^{1/2}$ |
| 2019-12-26 | 0.115 | 1889 | 0.120 | 1971 |
| 2019-12-27 | 0.095 | 1561 | 0.080 | 1314 |
| 2019-12-28 | 0.100 | 1643 | 0.104 | 1708 |
| 2019-12-29 | 0.148 | 2431 | 0.139 | 2284 |
| 2019-12-30 | 0.162 | 2661 | 0.133 | 2185 |
| 2019-12-31 | 0.138 | 2267 | 0.118 | 1938 |

Table C.2: Upper limits of small scale magnetoionic spatial fluctuations, $\langle \delta\beta^2_z \rangle^{1/2}$ (outer arc small $f_t$ sample), estimated from $\hat{\Gamma}_{\mathrm{RL}}$ and $\nu$, $D$, and $r_F$ for all observations.

| Obs. Epoch | -5 < $f_t$ < 5 | | $\|f_t\|$ > 5 | |
|---|---|---|---|---|
| | $\langle \Delta\phi^2_{\delta\beta} \rangle^{1/2}$ | $\langle \delta\beta^2_z \rangle^{1/2}$ | $\langle \Delta\phi^2_{\delta\beta} \rangle^{1/2}$ | $\langle \delta\beta^2_z \rangle^{1/2}$ |
| 2019-12-26 | 0.029 | 476 | 0.117 | 1922 |
| 2019-12-27 | 0.017 | 279 | 0.087 | 1429 |
| 2019-12-28 | 0.031 | 509 | 0.102 | 1676 |
| 2019-12-29 | 0.122 | 2004 | 0.143 | 2439 |
| 2019-12-30 | 0.054 | 887 | 0.149 | 2448 |
| 2019-12-31 | 0.047 | 772 | 0.126 | 2070 |

Table C.3: Upper limits of small scale magnetoionic spatial fluctuations, $\langle \delta\beta^2_z \rangle^{1/2}$ (inner and outer arc large $f_t$ sample), estimated from $\hat{\Gamma}_{\rm RL}$ and $\nu$, $D$, and $r_F$ for all observations.

# Appendix D

# RFI Blanking

## D.1 Manual RFI Blanking

| $N_{chan}$ | Frequency (MHz) | Region |
|---|---|---|
| 1119 | 1089.85 | C |
| 1120 | 1090.06 | C |
| 1121 | 1090.27 | C |
| 1122 | 1090.48 | C |
| 1520 | 1090.69 | C |
| 1123 | 1173.65 | C |
| 1524 | 1174.49 | C |
| 1526 | 1174.91 | C |
| 1528 | 1175.33 | C |
| 1530 | 1175.75 | C |
| 1532 | 1176.16 | C |
| 1534 | 1176.58 | C |
| 1536 | 1177.00 | C |
| 1538 | 1177.42 | C |

Table D.1: Manually blanked channels at 1.0 - 1.1 GHz

| $N_{chan}$ | Frequency (MHz) | Region |
|---|---|---|
| 1671 | 1205.63 | C |
| 1673 | 1206.88 | C |
| 1675 | 1227.37 | C |
| 1679 | 1246.17 | C |
| 1777 | 1246.17 | C |
| 1867 | 1246.17 | C |
| 1970 | 1267.70 | C |
| 1972 | 1268.11 | C |
| 1974 | 1268.54 | C |
| 1978 | 1269.37 | C |
| 1980 | 1269.79 | C |
| 2021 | 1278.36 | C |

Table D.2: Manually blanked channels at 1.2 GHz

| $N_{chan}$ | Frequency (MHz) | Region |
|---|---|---|
| 3244 | 1533.95 | B |
| 3245 | 1534.15 | B |
| 3249 | 1534.99 | B |
| 3368 | 1559.86 | B |
| 3369 | 1560.07 | B |
| 3510 | 1589.53 | B |
| 3567 | 1601.45 | B |
| 3568 | 1601.66 | B |
| 3569 | 1601.86 | B |
| 3949 | 1681.28 | B |
| 3952 | 1681.91 | B |
| 3954 | 1682.23 | B |
| 3955 | 1682.53 | B |
| 3956 | 1682.74 | B |
| 3957 | 1682.95 | B |
| 3958 | 1683.16 | B |
| 3960 | 1683.58 | B |
| 3976 | 1686.92 | B |
| 3977 | 1687.12 | B |

Table D.3: Manually blanked channels at 1.5 - 1.6 GHz

| $N_{chan}$ | Frequency (MHz) | Region |
|---|---|---|
| 383 | 936.04 | A |
| 384 | 936.25 | A |
| 385 | 936.46 | A |
| 386 | 936.67 | A |
| 387 | 936.88 | A |
| 388 | 937.09 | A |
| 390 | 937.50 | A |
| 392 | 937.92 | A |
| 394 | 938.34 | A |
| 396 | 938.76 | A |
| 398 | 939.18 | A |
| 399 | 939.38 | A |
| 400 | 939.59 | A |
| 401 | 939.80 | A |
| 402 | 940.01 | A |
| 403 | 940.22 | A |
| 404 | 940.43 | A |
| 405 | 940.64 | A |
| 408 | 941.27 | A |
| 410 | 941.68 | A |
| 412 | 942.10 | A |
| 414 | 942.52 | A |
| 416 | 942.94 | A |

Table D.4: Manually blanked channels at 940 MHz